Development of III-V Semiconductor Materials for Thermophotovoltaic Cells

Pamela Agata Jurczak

Thesis submitted for the degree of Doctor of Philosophy.

Department of Electronic and Electrical Engineering

University College London

July 2017

I, Pamela Agata Jurczak confirm that the work presented in this thesis is my own. Where information has been derived from other sources, I confirm that this has been indicated in the thesis.

…………………………………

Acknowledgements

Firstly, I would like to express my sincere gratitude to Professor Huiyun Liu for the continuous support of my PhD study, for his patience, motivation and guidance. Thank you for letting me explore my research interests and make my own mistakes, and all the advice on how to fix things when they would inevitably go wrong.

A very special thanks to my fellow group members: Dr Jiang Wu, Kevin Lee, Dr Mingchu Tang, Dr Yunyan Zhang, Arthur Onno, Dongyoung Kim, Dr Siming Chen, Dr Sabina Hatch, Dr Qi Jiang, Dr Phu Lam, Dr Joao Valente, Hao Xu and Mengya Liao for all the discussions and help along the way, and of course for your friendship. I could not have done this without you!

With a special mention to Dr Marina Gutiérrez from University of Cadiz and Dr Ana Sanchez from University of Warwick for excellent TEM images. To Suguo Huo from LCN and Steve Hudziak from UCL for their patience and all the help with SEM and AFM imaging.

And finally, last but by no means least, I am grateful to all my friends and family for your moral and emotional support throughout the ups and downs of this PhD and my life in general.

Abstract

Thermophotovoltaic energy conversion (TPV) is concerned with generation of power from heat sources. Multiple types of TPV systems have been developed so far; unfortunately, they all suffer from high losses and low overall efficiencies, usually only around 1%. Their performances could be greatly enhanced by high-efficiency converter cells, development of which is the main concern of the work presented in this thesis.

The first part focuses on research into materials suitable for fabrication of TPV cells. Low bandgap III-V and group IV semiconductors such as GaInAs, InAsP or GeSn were investigated. Then the thesis describes the model used to simulate behaviour of TPV cells under different illumination conditions. The results show that best performances are achieved for cells bandgap-matched to the emission of the radiator. Maximum theoretical efficiency of 27% has been predicted for cells with 0.43 eV bandgaps and a light-trapping architecture operating with a source at 1800 K delivering 500 $kW.m^{-2}$ of power.

The chapter on modelling is followed by detailed description of growth, fabrication and characterisation of GaInAs TPV devices. Quality of the grown material, its morphology and composition have been evaluated and then the processing steps for contacts deposition have been briefly explained. They are followed by a discussion of optical and electrical measurements for the fabricated devices.

The last chapter describes details of growth and characterisation of InAs

nanowires. Using nanostructures such as nanowires rather than bulk materials has significant advantages. Nanowires can be grown on virtually any substrate, which allows for integration with Si for CMOS-compatible devices. The improvement of optical properties of InAs nanowires has been the chief objective of this part of the thesis. Through a series of photoluminescence measurements, it has been demonstrated that capping the core-InAs nanowires with an InP passivation layer increases the photoluminescence emission up to ten times.

Impact Statement

Research on the low bandgap semiconductor materials for mid-wave infrared applications presented in this thesis has led to establishment of optimal material parameters for high-efficiency thermophotovoltaic (TPV) devices. This development will greatly help in designing new materials and structures not only for TPVs, but also for other mid-IR devices like photodetectors. Development of high-efficiency TPV energy converters can have a large impact on economic and environmental aspects of industries like steel and glass manufacturing as well as other industries where high temperature processing is required. Using the TPV cells to convert part of the large amount of waste heat produced by these industries into electricity can significantly reduce the energy usage resulting in a reduction of production cost. It will also have a positive impact on the environment as less electricity needs to be produced resulting in a lower carbon footprint.

Development of InAs nanowires (NWs) with good optical properties will have an impact on further research into this material system which can lead to fabrication of mid-wave infrared (mid-IR) detectors, TPVs or emitters based on these nanowires. Currently, good quality mid-IR devices are scarce and expensive. The ability of growing the InAs NWs on cheap, Si substrates can significantly reduce the cost of fabrication of such devices and make them more widely available. This is an important development for spectroscopic and sensing applications i.e. identifying and studying chemicals. Within the infrared spectral region of 2 to 20μm are contained strong

vibrational transitions of many important molecules, which makes the spectroscopic analysis within the IR range highly significant for materials processing, chemical, biochemical and food industries. Availability of low-cost, high-performance mid-IR lasers and detectors would have high positive impact on developments in the aforementioned industries. They could also be widely implemented in environmental sensing helping to monitor pollution levels or to detect i.e. gas leaks.

Contents

ACKNOWLEDGEMENTS 3

ABSTRACT 4

IMPACT STATEMENT 6

CONTENTS 8

LIST OF FIGURES 13

LIST OF JOURNAL PAPERS AND CONFERENCE PRESENTATIONS 22

CHAPTER 1: 25

INTRODUCTION 25

1.1 History of thermophotovoltaics 26

1.2 Aims and Objectives 28

1.3 Materials and Structures 29

1.3.1 Typical structures *29*

1.3.2 III-V Semiconductors *30*

1.3.3 Group IV Semiconductors *33*

1.3.4 Nanowire TPVs *34*

1.4 Advantages and Disadvantages of Thermophotovoltaic Systems 35

1.5 Applications of Thermophotovoltaic Systems 37

1.6 Thesis Structure 39

1.7 References 41

CHAPTER 2: **49**

OPERATIONAL PRINCIPLES OF TPVS **49**

2.1 PHYSICS OF THE CELLS 50

2.1.1 Thermal Emitters *50*

2.1.2 Basics of Semiconductors *52*

2.1.3 P-N Junction *55*

2.2 CELL OPERATION 57

2.2.1 Ideal Cell Operation *57*

2.2.2 Loss Mechanisms *60*

2.2.3 Performance Parameters *63*

2.3 REFERENCES 69

CHAPTER 3: **71**

EXPERIMENTAL METHODS **71**

3.1. EPITAXIAL GROWTH 72

3.1.1 Molecular Beam Epitaxy *72*

3.1.2 MBE Growth Mechanisms *79*

3.1.3 Atomic Force Microscopy *82*

3.1.4 Scanning Electron Microscopy *83*

3.1.5 Transmission Electron Microscopy *85*

3.1.6 X-ray Diffraction *87*

3.2. DEVICE PROCESSING 88

3.2.1 Cleaning *89*

3.2.2 Photolithography *90*

3.2.3 Wet Etching *92*

3.2.4 Metallisation *93*

3.2.5 Thermal Annealing *94*

3.3. CHARACTERISATION 95

3.3.1 Photoluminescence *95*

3.3.2 Electrical Characterisation *97*

3.4. REFERENCES 99

CHAPTER 4: **101**

THEORETICAL PERFORMANCES OF GAINAS THERMOPHOTOVOLTAIC CELLS **101**

4.1 THE BASIS OF THE MODEL 102

4.1.1 Architecture of the Cells *102*

4.1.2 Absorptivity Models *104*

4.1.3 Blackbody Theory and Flow Equilibrium *105*

4.1.4 Bulk Non-Radiative Recombination *108*

4.2 RESULTS AND DISCUSSION 111

4.2.1 Effects of Cell Temperature *111*

4.2.2 Impact of the Cell Thickness and Light Trapping *115*

4.2.3 Threading Dislocations *119*

4.2.4 Impact of the Thermal Emitter Temperature and Incident Power Density *122*

4.3 CONCLUSIONS 130

4.4 REFERENCES 134

CHAPTER 5: 136

GAINAS THERMOPHOTOVOLTAIC CELLS GROWN BY MBE ON GAAS SUBSTRATES 136

5.1 DESIGN OF THE CELLS AND MBE GROWTH 137

5.1.1 Structure of the Cells 137

5.1.2 MBE Growth 138

5.2 MATERIAL QUALITY ANALYSIS 139

5.2.1 Surface Morphology 139

5.2.2 Crystal Quality 141

5.2.3 Composition 147

5.3 FABRICATION PROCESS 150

5.4 ELECTRICAL AND OPTICAL CHARACTERISATION 151

5.4.1 Dark JV Measurements 151

5.4.2 Illuminated JV and QE 155

5.4.3 PL of Annealed Samples 160

5.5 CONCLUSIONS 163

5.6 REFERENCES 165

CHAPTER 6: 167

INAS NANOWIRES FOR THERMOPHOTOVOLTAIC APPLICATIONS 167

6.1. MOTIVATION AND INITIAL GROWTHS 168

6.2. INAS NANOWIRES CAPPED WITH INP 172

6.2.1. Growth Conditions and Initial Quality Assessment *172*

6.2.2. Crystal Quality, Structure and Composition *174*

6.3. PHOTOLUMINESCENCE STUDY OF THE INAS AND INAS/INP NANOWIRES 177

6.3.1. Peaks Analysis *178*

6.3.2. Temperature Dependent Measurements *181*

6.3.3. Integrated Photoluminescence Analysis *183*

6.4. CONCLUSIONS 186

6.5. REFERENCES 188

CHAPTER 7: 190

CONCLUSIONS AND FUTURE WORK 190

7.1 CONCLUSIONS 190

7.2 FUTURE PLANS 194

7.3 REFERENCES 196

List of Figures

FIGURE 1.1. STRUCTURE OF THE INGAAS TPV CELL DISCUSSED IN CHAPTER 5 INCLUDING THICKNESSES, COMPOSITIONS, DOPING LEVELS AND FUNCTIONS OF THE LAYERS. 30

FIGURE 1.2. DIAGRAM OF THE BANDGAPS OF VARIOUS SEMICONDUCTOR COMPOUNDS AND ALLOYS. 32

FIGURE 2.1. INTENSITY OF BLACKBODY RADIATION AT A RANGE OF TEMPERATURES FROM 1000 TO 1800 K AS A FUNCTION OF THE WAVELENGTHS OF EMITTED PHOTONS. 51

FIGURE 2.2. SPECTRA OF BLACK BODIES AT TEMPERATURES RANGING FROM 100 TO 10000 K INCLUDING ROOM TEMPERATURE (RED LINE) AND SOLAR SPECTRUM (YELLOW LINE) AS A FUNCTION OF THE WAVELENGTHS OF EMITTED PHOTONS. 51

FIGURE 2.3. THE ABSORPTION COEFFICIENT IN A VARIETY OF SEMICONDUCTOR MATERIALS AT 300 K AS A FUNCTION OF THE VACUUM WAVELENGTH OF LIGHT. 54

FIGURE 2.4. THE ABSORPTION COEFFICIENT OF VARIOUS COMPOSITIONS OF GAINAS AT 300 K AS A FUNCTION OF THE ENERGY OF THE PHOTONS. 55

FIGURE 2.5. ILLUSTRATION OF THE FORMATION OF A P-N JUNCTION. 56

FIGURE 2.6. THE BAND DIAGRAMS OF P-N JUNCTION AT THERMAL EQUILIBRIUM (A) AND UNDER REVERSE AND FORWARD BIAS (B). 57

FIGURE 2.7. CROSS-SECTION OF A TPV CELL. 58

FIGURE 2.8. AN EQUIVALENT CIRCUIT OF AN IDEAL SINGLE JUNCTION PHOTOVOLTAIC CELL. 60

FIGURE 2.9. AN EQUIVALENT CIRCUIT OF A NON-IDEAL SINGLE JUNCTION PHOTOVOLTAIC CELL. 63

FIGURE 2.10. AN EXAMPLE OF QUANTUM EFFICIENCY PLOT (SINGLE JUNCTION SILICON SOLAR CELL)

VS. IDEAL QUANTUM EFFICIENCY AS A FUNCTION OF THE WAVELENGTH OF INCOMING PHOTONS. 64
FIGURE 2.11. AN I-V CURVE OF A TYPICAL SOLAR CELL PLOTTED IN CONVENTIONAL WAY SHOWING THE OPEN-CIRCUIT VOLTAGE, THE SHORT-CIRCUIT CURRENT AND THE MAXIMUM POWER POINT. 66
FIGURE 2.12. OUTPUT POWER (BLUE) AND CURRENT (RED) AS A FUNCTION OF VOLTAGE IN A TYPICAL SOLAR CELL........ 67

FIGURE 3.1. VEECO GEN930 SOLID-SOURCE MBE. 73
FIGURE 3.2. SCHEMATIC DIAGRAM OF THE MBE GROWTH CHAMBER 75
FIGURE 3.3. SCHEMATIC DIAGRAM OF A STANDARD THERMAL EFFUSION CELL. 77
FIGURE 3.4. RHEED INTENSITY OSCILLATION AT DIFFERENT GROWTH STAGES. 79
FIGURE 3.5. SIMPLIFIED MBE GROWTH MECHANISM. 80
FIGURE 3.6. ATOMS BEHAVIOUR DURING SURFACE DEPOSITION. 81
FIGURE 3.7. ILLUSTRATION OF THE THREE MAIN GROWTH MODES: FRANK-VAN DER MERWE, STRANSKI-KRASTANOV AND VOLMER-WEBER. 82
FIGURE 3.8. AFM IMAGE OF AN (A) $IN_{0.85}GA_{0.15}AS$ TPV CELL GROWN ON GAAS SUBSTRATE WITH AN INALAS STEP-GRADED BUFFER GROWN BY MBE AND (B) INAS/GAAS QUANTUM DOTS, BOTH 1MM × 1MM. 83
FIGURE 3.9. SCHEMATIC DIAGRAM OF A SCANNING ELECTRON MICROSCOPE. 84
FIGURE 3.10. LOW-MAGNIFICATION SIDE-VIEW AND TOP-VIEW AND HIGH-MAGNIFICATION TOP-VIEW SEM IMAGES OF VERTICALLY ORIENTATED GAASP P–N HOMOJUNCTION NANOWIRES GROWN ONTO A P^{+}-SI (111) SUBSTRATE. 85

FIGURE 3.11. TEM IMAGES OF (A) CROSS SECTION OF AN INGAAS TPV CELL, (B) THE TOP LAYERS AND (C) CROSS SECTION OF THE BUFFER LAYERS (INDICATED WITH BLUE CIRCLE IN A) WITH VISIBLE THREADING DISLOCATIONS. THE RED CIRCLE MARKS ONE OF THE THREADING DISLOCATIONS FOR CLARITY........ 87

FIGURE 3.12. ILLUSTRATION OF AN XRD SYSTEM (A) AND THE MEASUREMENT MECHANISM (B). 88

FIGURE 3.13. FLOW CHART OF STANDARD DEVICE FABRICATION PROCESS FOR TPV TEST CELLS... 89

FIGURE 3.14. MAIN STEPS OF A STANDARD LIFT-OFF PROCEDURE. 92

FIGURE 3.15. SIMPLIFIED PL EQUIPMENT SETUP. 97

FIGURE 4.1. THE DETAILS OF THE CELL ARCHITECTURES WITH (A) AND WITHOUT (B) LIGHT TRAPPING MECHANISM INVESTIGATED IN THIS CHAPTER........ 103

FIGURE 4.2. THE DETAILS OF THE ABSORPTIVITY MODELS USED IN THE SIMULATIONS: (A) FLAT TOP SURFACE WITH FRONT SURFACE (RED ARROWS) AND BACK SURFACE (GREEN ARROWS) ABSORPTION AND (B) IDEALLY TEXTURED SURFACE WITH A BACK MIRROR CREATING LIGHT TRAPPING (ORANGE ARROWS)........ 104

FIGURE 4.3. MAXIMAL THEORETICAL EFFICIENCY *H* OF A $GA_XIN_{1-X}AS$ CELL WITH PERFECT LIGHT TRAPPING AS A FUNCTION OF THE TEMPERATURE OF THE CELL *T* AND THE GA COMPOSITION. 112

FIGURE 4.4. MAXIMAL THEORETICAL EFFICIENCY *H* (BLACK, LEFT SCALE) AND OPTIMAL GA COMPOSITION FOR BEST-MATCHED BANDGAP (RED, RIGHT SCALE) OF A $GA_XIN_{1-X}AS$ CELL WITH PERFECT LIGHT TRAPPING AS A FUNCTION OF THE TEMPERATURE OF THE CELL *T*........ 114

FIGURE 4.5. THE BANDGAP E_G OF A $GA_XIN_{1-X}AS$ CELL WITH PERFECT LIGHT TRAPPING AS A FUNCTION OF THE TEMPERATURE OF THE CELL *T* AND THE GA COMPOSITION........ 115

FIGURE 4.6. MAXIMAL THEORETICAL EFFICIENCY *H* OF A $GA_XIN_{1-X}AS$ CELL WITH (A) AND WITHOUT (B)

PERFECT LIGHT TRAPPING AS A FUNCTION OF THE THICKNESS OF THE CELL L AND THE BANDGAP OF THE CELL E_G. 117

FIGURE 4.7. MAXIMAL THEORETICAL EFFICIENCY H (BLACK, LEFT SCALE) AND THE BANDGAP OF THE CELL E_G (RED, RIGHT SCALE) OF A $GA_XIN_{1-X}AS$ CELL WITH (DASHED LINES) AND WITHOUT (SOLID LINES) PERFECT LIGHT TRAPPING AS A FUNCTION OF THE THICKNESS OF THE CELL L. 118

FIGURE 4.8. MAXIMAL THEORETICAL EFFICIENCY H OF A $GA_XIN_{1-X}AS$ CELL WITH PERFECT LIGHT TRAPPING (A) AND WITHOUT IT (B) AS A FUNCTION OF THE THREADING DISLOCATION DENSITY N_{TD} AND THE BANDGAP OF THE CELL E_G. 120

FIGURE 4.9. MAXIMAL THEORETICAL EFFICIENCY H (BLACK, LEFT SCALE) AND THE BANDGAP OF THE CELL E_G (RED, RIGHT SCALE) OF A $GA_XIN_{1-X}AS$ CELL WITH (DASHED LINES) AND WITHOUT (SOLID LINES) PERFECT LIGHT TRAPPING AS A FUNCTION OF THE THREADING DISLOCATION DENSITY N_{TD}. 121

FIGURE 4.10. MAXIMAL THEORETICAL EFFICIENCY H OF A $GA_XIN_{1-X}AS$ CELL WITH PERFECT LIGHT TRAPPING (A) AND WITHOUT IT (B) AS A FUNCTION OF THE TEMPERATURE OF THE THERMAL EMITTER T_{SOURCE} AND THE BANDGAP OF THE CELL E_G. 123

FIGURE 4.11. MAXIMAL THEORETICAL EFFICIENCY H (BLACK, LEFT SCALE) AND THE BANDGAP OF THE CELL E_G (RED, RIGHT SCALE) OF A $GA_XIN_{1-X}AS$ CELL WITH (DASHED LINES) AND WITHOUT (SOLID LINES) PERFECT LIGHT TRAPPING AS A FUNCTION OF THE TEMPERATURE OF THE THERMAL EMITTER T_{SOURCE}. 125

FIGURE 4.12. MAXIMAL THEORETICAL EFFICIENCY H OF A $GA_XIN_{1-X}AS$ CELL WITH PERFECT LIGHT TRAPPING (A) AND WITHOUT IT (B) AS A FUNCTION OF THE INCIDENT POWER DENSITY P_{IN} AND THE BANDGAP OF THE CELL E_G. 127

Figure 4.13. Maximal theoretical efficiency *η* (black, left scale) and the bandgap of the cell E_G (red, right scale) of a $Ga_xIn_{1-x}As$ cell with (dashed lines) and without (solid lines) perfect light trapping as a function of the incident power density P_{IN}........ 128

Figure 4.14. Maximal theoretical efficiency *η* of an InAs cell with perfect light trapping as a function of the incident power density P_{IN} and temperature of the thermal emitter T_{SOURCE}. 129

Figure 5.1. Structure of the GaInAs TPV cells grown by MBE detailing the layers and their compositions. 137

Figure 5.2. AFM images of the as-grown GaInAs TPV cells from the centre (a,b), middle (c,d) and the edge (e,f) of the wafer, (a,c,e) are 5um × 5um and (b,d,f) are 1um × 1um. The scale on the right indicates the roughness of the samples. Optical microscope image of the centre part of the sample (g). 140

Figure 5.3. TEM images of the GaInAs cells showing the layers within the structure (a), a cross-section including the threading dislocations (b), micrograph of the top layers (c) and the network of misfit dislocations from which threading dislocations originate (d). 142

Figure 5.4. Schematic representation of MD formation and distribution on the GaSb:Be/GaAs heterostructure. (a) Step 1: initial islands following the Volmer-Weber growth model. (b) Step 2: Strain relaxation by IMF network (>) and 60° MDs at the leading edges (h). (c) Step 3: Distribution of the 60° MDs originated in the coalescence areas for both samples. (d) Step 4: Final distribution of 90° and 60° MDs in the GaSb(:Be)/GaAs system. 146

FIGURE 5.5. CROSS-SECTIONAL TEM MICROGRAPHS AT THE INTERFACE OF (A) GASB/GAAS (SAMPLE A) AND (B) GASB:BE/GAAS (SAMPLE B). BOTH MICROGRAPHS HAVE BEEN TAKEN WITH THE SAME SAMPLE THICKNESS, MAGNIFICATION AND ANGLE. THE <001> PLANE AT THE GASB/GAAS INTERFACE IS SCHEMATICALLY SHOWN IN BETWEEN THE TWO MICROGRAPHS TO HELP VISUALISE THE MD CONFIGURATION. THE WHITE ARROWS INDICATE THE ORIGIN POINTS OF THE TDS. 147

FIGURE 5.6. XRD COMPOSITION MEASUREMENT RESULTS FOR THE GAINAS TPV CELL GROWN ON GAAS SUBSTRATE WITH GASB, INAS AND METAMORPHIC BUFFER LAYERS. 148

FIGURE 5.7. THE RESULTS OF THE LOW-TEMPERATURE PHOTOLUMINESCENCE MEASUREMENTS OF THE GAINAS TPV CELL. 149

FIGURE 5.8. THE FABRICATED DEVICES AFTER CONTACTS DEPOSITION USING (A) TOP-TOP APPROACH WITH PHOTOLITHOGRAPHY MASKING AND (B) TOP-BOTTOM APPROACH WITH A SHADOW MASK FOR TOP CONTACTS. SCHEMATICS OF THE METAL CONTACTS AND THEIR DIMENSIONS FOR (C) THE SHADOW MASK AND (D) THE PHOTOLITHOGRAPHY MASK. 151

FIGURE 5.9. THE PRE-ANNEALING DARK JV MEASUREMENTS RESULTS OF FIFTEEN $IN_{0.85}GA_{0.15}AS$ TPV CELLS. 152

FIGURE 5.10. THE PRE- (DASHED LINES) AND POST-ANNEALING (CONTINUOUS LINES) DARK JV MEASUREMENTS OF SOME OF THE TOP-TOP CONTACTED $IN_{0.85}GA_{0.15}AS$ TPV CELLS. THE TABLE DETAILS THE TIMES AND TEMPERATURES OF THE ANNEALING PROCESS AS WELL AS WHICH DEVICES HAVE BEEN SUBJECTED TO IT. 153

FIGURE 5.11. THE DARK IV MEASUREMENTS OF THE $IN_{0.85}GA_{0.15}AS$ TPV CELLS PROCESSED USING TOP-TOP CONTACTS (BLUE LINES) AND USING TOP-BOTTOM CONTACTS (GREEN LINES)

COMPARED TO THEIR RESPECTIVE REFERENCES WITH NOT ANNEALED CONTACTS (GREY AND BLACK LINES). 154

FIGURE 5.12. THE DARK CURRENT MEASUREMENTS FOR A RANGE OF BIAS VOLTAGES FOR THE $In_{0.85}Ga_{0.15}As$ CELLS AT ROOM TEMPERATURE (BLACK LINE) AND AT 78 K (RED LINE). 156

FIGURE 5.13. THE CURRENT MEASUREMENTS FOR A RANGE OF BIAS VOLTAGES FOR THE $In_{0.85}Ga_{0.15}As$ CELLS AT ROOM TEMPERATURE UNDER A 1000°C BLACKBODY SOURCE (RED LINE) AND IN THE DARK (BLACK LINE). 157

FIGURE 5.14. THE CURRENT MEASUREMENTS FOR A RANGE OF BIAS VOLTAGES FOR THE $In_{0.85}Ga_{0.15}As$ CELLS AT ROOM TEMPERATURE UNDER A 1000°C BLACKBODY SOURCE (RED DASHED LINE) AND IN THE DARK (BLACK DASHED LINE), LOW TEMPERATURE DARK CURRENT MEASUREMENT (SOLID BLACK LINE) AND CALCULATED VALUES FOR LOW TEMPERATURE CURRENT UNDER 1000°C BLACKBODY SOURCE (RED SOLID LINE). 158

FIGURE 5.15. THE QUANTUM EFFICIENCY (ELECTRONS/PHOTON, BLACK LINE) AND RESPONSIVITY (A/W, RED LINE) MEASUREMENTS FOR A RANGE OF WAVELENGTHS FOR THE $In_{0.85}Ga_{0.15}As$ CELLS AT 78 K UNDER A 1000°C BLACKBODY SOURCE. 160

FIGURE 5.16. (A) THE PHOTOLUMINESCENCE MEASUREMENTS FOR THE $In_{0.85}Ga_{0.15}As$ SAMPLES ANNEALED AT DIFFERENT CONDITIONS (DETAILED IN THE TABLE) COMPARED TO THE UNANNEALED REFERENCE SAMPLE. THE TWO SMALL PLOTS SHOW TRENDS FOR THE TWO DIFFERENT ANNEALING DURATIONS: (B) 150S (SAMPLES 2,4,6) AND (C) 300S (SAMPLES 3,5,7). 162

FIGURE 6.1. THE SEM IMAGES OF SEVERAL INAS NWS SAMPLES. 170

FIGURE 6.2. THE PL SPECTRA OF SEVERAL INAS NWS SAMPLES TAKEN AT 10K. 171

FIGURE 6.3. THE SEM IMAGES (TILT ANGLE 25°) OF (A) INAS CORE-ONLY NWS AND (B) INAS/INP CORE/SHELL NWS GROWN ON SI(111) SUBSTRATES VIA A SELF-CATALYZED MBE GROWTH METHOD. THE INSET IN (B) SHOWS A HIGH MAGNIFICATION IMAGE OF SINGLE INAS/INP NANOWIRES. 173

FIGURE 6.4. (A) <112> ADF-STEM IMAGE OF A MIDDLE SECTION OF ONE OF THE INAS/INP NWS CLEARLY SHOWING THE CORE AND SHELL PARTS OF THE STRUCTURE. (B) <110> ADF-STEM IMAGE OF A MIDDLE SECTION OF ONE OF THE INAS/INP NWS SHOWING POLYTYPIC STRUCTURE OF THE NANOWIRES WITH HIGHLIGHTED EXAMPLES OF WURTZITE (BLUE) AND ZINC-BLENDE (GREEN) CRYSTAL PHASES. THE INSET SHOWS THE SELECTIVE AREA ELECTRON DIFFRACTION PATTERN TAKEN FOR ONE OF THE NANOWIRES CONFIRMING THAT BOTH WURTZITE (WZ) AND ZINC-BLENDE (ZB) PHASES ARE PRESENT. 175

FIGURE 6.5. COMPOSITION ANALYSIS OF THE INAS/INP NWS WITH EDX. (A) MIDDLE SECTION OF A NW WITH HIGHLIGHTED (B) IN, (C) AS AND (D) P ELEMENTAL DISTRIBUTION. EDX LINE PROFILE TAKEN ALONG THE WHITE LINE INDICATED IN (A) CORRECPONDING TO THE IN, AS AND P HAVE ALSO BEEN PLOTTED IN (B), (C) AND (D), RESPECTIVELY. 176

FIGURE 6.6. PL SPECTRA TAKEN AT 10K FOR (A) THE INAS CORE-ONLY AND (B) THE INAS/INP CORE/SHELL NANOWIRES WITH INAS WAFER EMISSION AS REFERENCE. MEASURED SIGNAL (RED), FITTED GAUSSIAN PEAKS (GREEN), SUM OF THE FITTED PEAKS (BLUE) AND NORMALIZED INAS WAFER REFERENCE (BLACK) HAVE BEEN PLOTTED. 179

FIGURE 6.7. PL SPECTRA TAKEN AT TEMPERATURES BETWEEN 10 AND 300 K FOR (A) THE INAS CORE-ONLY AND (B) THE INAS/INP CORE/SHELL NANOWIRES. 181

FIGURE 6.8. EMISSION IMPROVEMENT OF THE INAS/INP NWS OVER INAS NWS, THE INSETS SHOW

PL emission for the two samples at 10 and 300 K. 182

Figure 6.9. Integrated PL as a function of (a) excitation power for a range of temperatures between 10 and 300 K and (b) sample temperature for InAs/InP nanowires (blue), InAs core-only nanowires (green) and InAs wafer (black). 185

List of Journal Papers and Conference Presentations

Papers:

1. **Jurczak P.**, Onno A., Sablon K., Liu H., “Efficiency of GaInAs thermophotovoltaic cells: the effects of incident radiation, light trapping and recombinations”, Optics Express 23(19), 2015.

2. **Jurczak P.**, Sablon K., Gutiérrez M., Liu H. and Wu J., “2.5-μm InGaAs photodiodes grown on GaAs substrates by interfacial misfit array technique”, Infrared Physics & Technology, Volume 81, Pages 320-324, 2017.

3. **Jurczak P.**, Zhang Y., Wu J., Sanchez A.M., Aagesen M., and Liu H., “Ten-fold Enhancement of InAs Nanowire Photoluminescence Emission with an InP Passivation Layer”, Nano Letters 17(6), 2017.

4. Zhang Y., Sanchez A.M., Sun Y., Wu J., Aagesen M., Huo S., Kim D., **Jurczak P.**, Xu X., Liu H., “Influence of droplet size on the growth of self-catalyzed ternary GaAsP nanowires”, Nano Letters 16(2), 2016.

5. Tang M., Chen S., Wu J., Jiang Q., **Jurczak P.**, Liao M., Kennedy K., Beanland R., Seeds A. and Liu H., “Optimizations of Defect Filter Layers for 1.3-μm InAs/GaAs Quantum-Dot Lasers Monolithically Grown on Si substrates”, IEEE

Photonics Society (IPS) Journal of Selected Topics in Quantum Electronics, vol. 22, no. 6, pp. 50-56, 2016.

6. Zhang Y., Aagesen M., Sanchez A.M., Wu J., Beanland R., Ward T., Kim D., **Jurczak P.**, Huo S. and Liu H., “Growth of high-quality self-catalyzed core-shell GaAsP nanowires on Si substrates”, Proc. SPIE 9758, Quantum Dots and Nanostructures: Growth, Characterization, and Modelling XIII, 97580E, 2016.

7. Zhang Y., Sanchez A.M., Aagesen M., Sun Y., Wu J., Kim D., **Jurczak P.**, Huo S., Xu X. and Liu H., “Influence of droplet size on the growth of high-quality self-catalyzed GaAsP nanowires”, Proc. SPIE 10114, Quantum Dots and Nanostructures: Growth, Characterization, and Modelling XIV, 101140K, 2017.

8. Gutiérrez M., Araujo D., **Jurczak P.**, Wu J. and Liu H., “Solid solution strengthening in GaSb/GaAs: A mode to reduce the TD density through Be-doping”, Applied Physics Letters, 110, 092103, 2017.

Conference Presentations:

1. "Impact of the incident spectrum and power on the performances of bandgap-dependent GaInAs thermophotovoltaic cells", 2015, Semiconductor and Integrated OptoElectronics (SIOE), Cardiff (UK Wales).

2. "Impact of the threading dislocation densities on the performances of $Ga_xIn_{1-x}As$ thermophotovoltaic cells", 2015, UK Semiconductors, Sheffield (UK).

3. "The Impact of Incident Spectrum and Power on the Performances of GaInAs Thermophotovoltaic Cells", 2015, European Photovoltaic Solar Energy Conference and Exhibition (EU PVSEC), Hamburg (Germany).

4. "III-V semiconductor nanowires for highly efficient solar and thermophotovoltaic cells", 2016, ISSON16, Thessaloniki (Greece).

5. "Up to ten-fold enhancement of emission from InP-passivated InAs nanowires", 2017, Nanowires Week, Lund (Sweden).

6. "Ten-fold enhancement of photoluminescence emission from InAs nanowires passivated with InP", 2017, UK Semiconductors, Sheffield (UK).

Chapter 1:

Introduction

In 2012, the International Energy Agency (IEA) estimated the total energy consumption in the world at 8979 megatoe[1] (toe – tonne of oil equivalent, approximately 42 gigajoules or 11.6 MWh). [2] This number is predicted to increase by 37% until 2035,[3] population growth and rise in income per person being the main reasons behind the increasing demand for energy. At present most efforts are directed towards limiting the use of fossil fuels (currently 86% shares of the primary energy) [3] and developing more efficient ways of obtaining energy from renewable sources (solar, hydro, biofuels etc.). The most abundant of the clean sources is solar radiation, which led to great developments in photovoltaic (PV) technology and helped to

commercialise it on global scale. Usually PV cells are used to convert the visible part of the solar spectrum into electricity. However, they can also be used to provide significant amounts of energy from the infrared radiation, i.e. radiant heat. This approach is called thermophotovoltaics (TPV) and it can be used with a vast number of sources. The two most researched and popular areas are concentrated solar thermal converters and micro burners-based TPV systems. The first one uses the solar radiation to generate large amounts of heat and then convert it into electricity using TPV cells. The second approach relies of the premise that TPV devices can be much more efficient at converting the energy generated from burning fossil fuels into electricity than the conventionally used methods. Systems with e.g. oil burners can be easily scaled to create portable energy sources. Another application for the TPVs is recovering unused heat from industrial processes, effectively reducing the amount of wasted energy and hence limiting the amount of fossil fuels needed. This chapter gives an introduction to the thermophotovoltaics including a brief history of this technology and examples of materials suitable for TPV cells. The most recent developments are also discussed and some more details are given on the current and potential applications.

1.1 History of thermophotovoltaics

It is hard to determine when exactly thermophotovoltaic (TPV) energy conversion was first envisioned and who should be named as its inventor. P. Aigrain proposed the TPV direct energy conversion concept during a series of lectures at the MIT

between 1960 and 1961 [5] and hence is often cited as the inventor of TPVs [6,7]. However, the first TPV system was built in 1956 by Henry H. Kolm [4] at the MIT Lincoln Lab. It consisted of a camping lantern with an incandescent gas mantle as the radiator and a silicon cell as the photoconverter.

In the 1970s interest in TPVs was on the raise because of the energy crisis. A lot of attention was focused on renewable energy sources, especially solar, and hence solar-TPV systems were considered. Record efficiency of 35% has been recorded for GaAs/GaSb tandem cells [8]. Nevertheless the TPV progress was soon halted when the US army chose the more mature at the time technology of thermoelectric over thermophotovoltaics. This resulted in most of the industrial participants as well as academic institutions and laboratories dropping the TPV-related research.

Interest in TPVs was still low in the 1980s, with most research efforts addressing possible improvements to already established systems i.e. the silicon converters and the rare-earth emitters. 1990s brought renewed interest into the field with developments in III-V semiconductor production, which opened new possibilities for TPV cells. The army became interested once again, with NREL investing in development of narrow bandgap cells. They also started the first global conference on TPVs and assumed responsibility over its proceedings [7]. Since 2000s most research has moved from US to Europe. It focused on development of novel III-V low-bandgap cells (see section 1.2) and later on optimisation of whole systems using the most recent advances like photonic crystals. More details on specific systems and applications they have been developed for can be found in section 1.5.

1.2 Aims and Objectives

The main objective of the project presented in this thesis was to develophighly-efficient and cost-effective III-V semiconductor materials for use in thermophotovoltaic (TPV) energy conversion. As means of converting heat into electricity, thermophotovoltaics aim at reclaiming otherwise wasted thermal energy from sources like industrial furnaces or solar panels. Industrial procedures in production of glass, steel and other high-temperature processed materials waste up to half of the supplied energy as dissipated heat. Reclaiming even a fraction of this energy would lead to significant savings in terms of fabrication cost as well as have a positive impact on the environment as less energy would need to be produced. The TPVs could also be applied to solar panels in order to improve the solar spectrum conversion efficiency or as power generators with other high-temperature heat sources. However, there are several roadblocks on the path from the theoretical TPV operation to realisation of efficient, commercially viable TPV devices. A practical system must have a high conversion efficiency, be low cost and reliable. Moreover, due to the proximity of high-temperature sources, efficient cooling system needs to be used in order to ensure optimal operating conditions for the conversion cells. Due to these obstacles, no commercial TPV devices have been developed so far. In this project we aimed to develop a semiconductor TPV conversion cell which would fulfil two of the objectives listed above: high efficiency and low cost. In order to achieve this specification, several steps have to be completed. Firstly, an optimal semiconductor material for TPV applications needs to be established based on the physical principles of

operation of a TPV cell. Then, an optimal structure needs to be designed to allow for an efficient energy conversion. Finally, the designed structure needs to be grown and fabricated into devices and tested. It is important to make sure that every step of the way is leading to creation of low-cost and highly efficient devices as specified in the objectives of this project.

1.3 Materials and Structures

1.3.1 Typical structures

The basis of a TPV cell, same as any PV cell, is a semiconductor p-n junction which allows for generation of electron-hole pairs via the photovoltaic effect as well as efficient separation and extraction of carriers. Therefore the active region of any TPV cell would comprise of a p-n or a p-i-n junction of semiconductor materials with bandgaps best matched to the heat source with which the TPV cell will be used. Details on semiconductors, p-n junction operation and other aspects of physics relevant to TPVs can be found in Chapter 2 of this thesis.

The main parts of a typical TPV structure are: substrate, buffer layers, contact layers and the active region. The buffer layers are used to gradually change the lattice constant from that of the substrate to that of the active region. In order to minimise the number of dislocations and defects arising from lattice mismatch dislocation filter layers can be used to trap the dislocation in the buffer section of the cell. The contact layers are highly doped in order to make the carrier transport to the outside load more efficient. Structure of the TPV cell discussed in Chapter 5 of the thesis has been

presented in figure 1.1 as an example. All of the layers have their thicknesses, materials and doping levels specified. The specific layers have also been assigned to the functions specified above for reference.

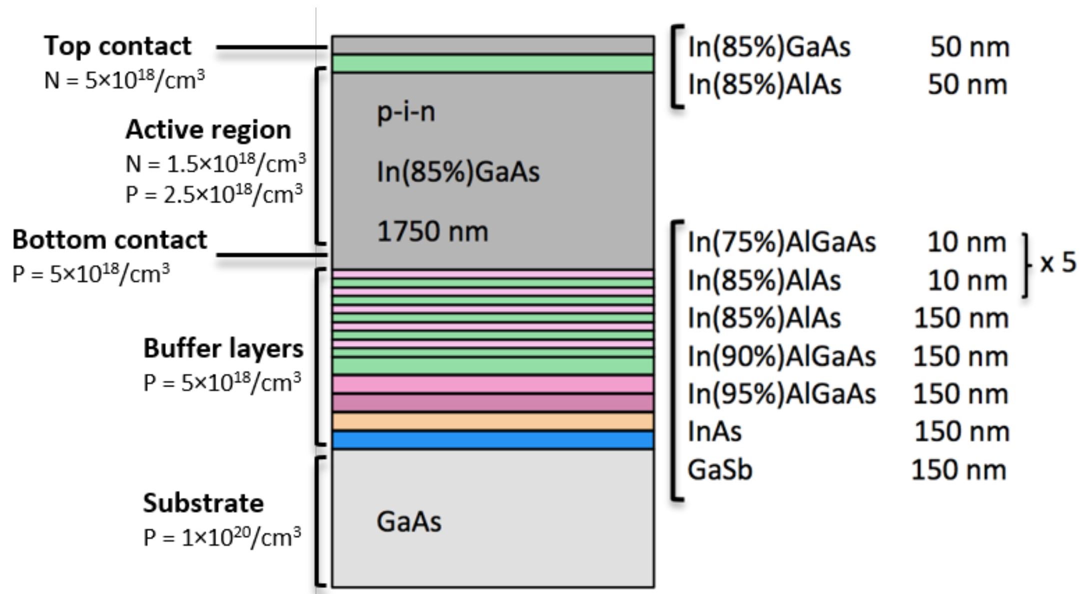

Figure 1.1. Structure of the InGaAs TPV cell discussed in Chapter 5 including thicknesses, compositions, doping levels and functions of the layers.

1.3.2 III-V Semiconductors

The early designs of TPVs used silicon cells as the photovoltaic converters. However, for efficient operation a Si cell would need a source above 2000 K [6]. Therefore researchers started looking into other suitable materials, mostly germanium [9,10]. The results however were very poor, mostly due to the indirect bandgap of Ge. Later on, around 1990s, the research moved to III-V semiconductor compounds when it became possible to fabricate high quality materials with advances in MOCVD and MBE growth techniques.

The most popular III-V semiconductors for TPVs are GaSb and $In_{0.53}Ga_{0.47}As$, for both of which bandgaps are about 0.74 eV, suitable for TPV applications. These two systems are preferred since GaSb can be grown on GaSb substrates and $In_{0.53}Ga_{0.47}As$ on InP to which it is lattice matched. This means that the cells can be grown with a low number of defects ensuring good crystal quality and hence high performances. However, for the best match to the thermal radiators' emission wavelengths, in order to maximise the efficiency of energy conversion, lower bandgap materials would be a better choice. According to most research, bandgaps between 0.5 and 0.6 eV are optimal for majority of TPV applications [6]. Recently it has been proposed that semiconductors with even lower bandgaps, between 0.35 and 0.45 eV, could be more suitable to achieve high efficiencies (see Chapter 4).

Figure 1.2 shows the diagram of energy gap versus lattice constant of various semiconductor compounds. It can be seen that there are many possible options of combining the elements in such a way that materials with bandgaps required for TPV applications are formed. For best conversion efficiency bandgaps should be matched to the wavelength of the photons emitted by the source. The aforementioned GaInAs, especially its In-rich compositions, and GaSb are the most popular choices. Some lower bandgap materials like InAs, InSb and their ternary compound InAsSb are also suitable, as well as As-rich InAsP and some quaternary compounds like e.g. InGaAsSb. The main challenge in realising devices made of these materials lies in growth of high-quality cells. Therefore, it is important not only to find a material with a suitable bandgap, but it is also imperative to choose a substrate closely lattice

matched to that material. Since the choice of suitable low-cost semiconductor substrates is limited, even now any cells other than InGaAs or GaSb are rare and their efficiencies are low.

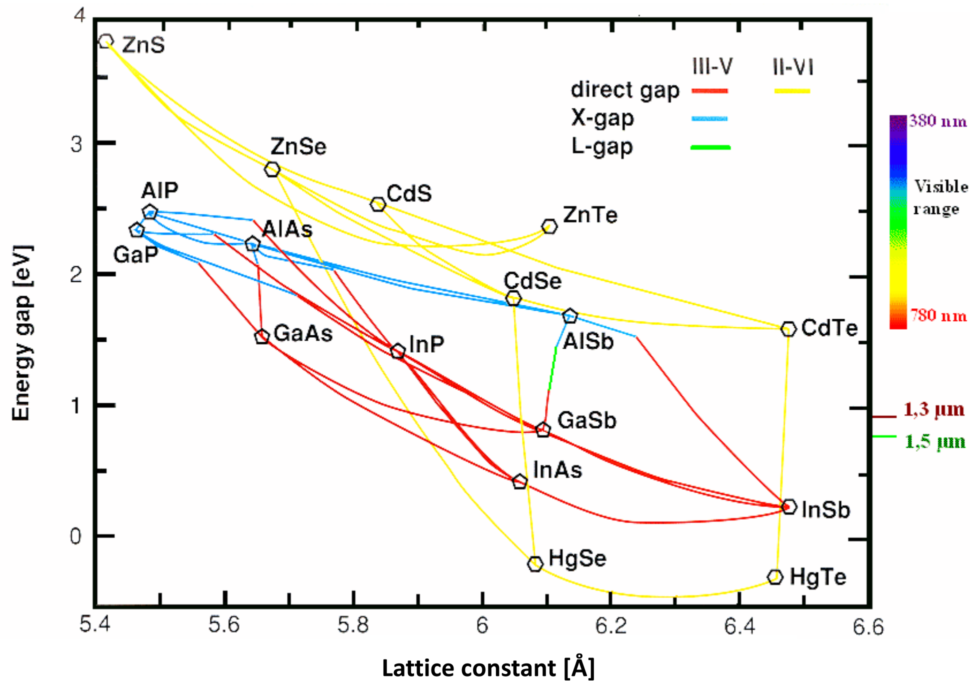

Figure 1.2. Diagram of the bandgaps of various semiconductor compounds and alloys. [11]

The most advanced of thermophotovoltaic cells, GaSb, are currently commercially produced and available for purchase i.e. from JX Crystal [12]. GaInAs compounds however are more interesting from the research point of view since their bandgaps can be engineered to anything between 0.36 and 1.42 eV, making it a flexible choice for various applications. Some of the first GaInAs TPV cells were fabricated by Wilt [13] et al. and Wanlass [14] et al. in the 1990s and later on by Hudait [15] et al. They were all lattice matched to InP, had a 0.74 eV bandgap and were grown by MOCVD [13, 16] or MBE [15] (see section 3.1 for details on the growth methods). Cells

with lower bandgaps became feasible in early 2000s after introduction of step-graded [17] and metamorphic [18] buffers between the InP substrate and the In-rich GaInAs cells. Hudait et al., Wernsman et al. and Cederberg et al., using MBE systems, grew cells with bandgaps of 0.55 eV [16] and 0.6 eV [19-22], achieving higher efficiencies than previously with the lattice-matched cells. There have been no recent advances in InGaAs cells to our knowledge, however several models [23,24] have been developed to better estimate the optimal bandgap of such cells and understand their performance issues, which will hopefully lead to fabrication of better TPV devices in the near future. More information on this can be found in Chapter 4.

1.3.3 Group IV Semiconductors

Most widely used group IV semiconductors are silicon and germanium. Both of these materials have been used in early designs of TPV cells, however they performances were poor due to indirect bandgaps. In the late 1987 Jenkins and Dow [25] proposed germanium tin compound as an alternative group IV material for TPV cells. They modelled the bandgaps of different compositions of GeSn and predicted that compositions with 20% or more of Sn would have direct bandgap in infrared region. This could solve the problem of group IV cells performance problems and help to take advantage of integrating the cells with silicon platform. In 1997 He and Atwater were the first ones to grow and measure GeSn alloys [26]. Measurements of absorption coefficients of compounds with 0-15% Sn showed that the cross from indirect to direct bandgap happens at much lower percentage of tin than predicted before, at around

12%.

He and Atwater's measurements prompted new modelling studies better matching the experimental results [27-29], all focused on simulating the bandgap of GeSn. Further experimental growth also followed using MBE [26, 30-45] and CVD systems [46-53]. The direct bandgap was estimated for compounds with 7% Sn or more. Several simple diode devices [43, 54-60] and structures with quantum dots were made as well [61]. In general, the MBE-grown GeSn has better quality and morphology but low Sn incorporation, while CVD-grown compounds are capable of incorporating much higher Sn percentages but the quality of the material is poor. Therefore so far there are no good results for high quality GeSn growth and much more research is needed in this area.

1.3.4 Nanowire TPVs

There are several advantages of nanowires (NWs) compared to thin film structures because of their properties being different than bulk material. The most important one is that NWs can be integrated with a wide variety of substrates. Since the NWs have a small diameter, the interface between them and the substrate is small, which is beneficial for strain relaxation. Hence materials with large lattice and thermal coefficient mismatch can be integrated and even if misfit dislocations are formed, there are no threading dislocations observed. Effectively, all the defects are confined to the NW/substrate interface. This means that NWs can be grown on transparent and flexible substrates or that III-V nanowires can be grown on Si wafers. This is

important from the perspective of TPVs. InAs, InAsP, GaInAs, GaSb and other compounds with appropriate bandgaps can be used to grow NWs for TPV applications and possibility of integrating them on Si means considerable reduction in production cost. NWs also have much greater surface area and NW cells have very low reflectance, resulting in higher efficiencies of the NW cells compared with their thin film counterparts.

1.4 Advantages and Disadvantages of Thermophotovoltaic Systems

The operation of semiconductor TPVs differs from that of standard solar cells. There are also principal differences between TPVs and other methods of heat conversion. The most important features of TPV systems are [6]:

- High power output – devices with 10-20 kW.m^{-2} of output powers have already been fabricated and these are much higher than e.g. solar cells for which the input power is only 1 kW.m^{-2}.

- Supply and demand are in phase – circumvents one of the biggest problems of solar energy generation that it can only happen when the sun is shining. Hybrid solar-thermal systems can be used, some of which have already been implemented. In such systems the excess heat from solar panels is stored using oil or molten salts. TPVs could then be used to generate electricity when the sun is down.

- Versatile fuel usage – not only solar energy can be used to power TPV systems but also waste industrial heat, gas burners, in principle even nuclear generators,

which makes them much more flexible than solar cells.

- Light-weight, no moving parts – which means that devices are quiet and low-maintenance, which makes them perfect for use in remote locations or as portable power sources i.e. for military applications.

- TPVs can be pollution free – if clean fuels are burned or if sun or waste heat are used as the thermal sources.

- Potentially low cost – especially if integrated on silicon, due to much larger output power densities compared with solar, smaller and fewer cells are needed for the same power output.

- Combined heat and power generation – last but not least the TPV systems can work in a similar way to concentrator solar systems, where the PV cells convert incident radiation into electricity and the excess heat is usually used to heat up water for residential properties. The TPVs could also be added to the existing systems to improve their efficiencies by converting the waste heat into electricity.

All of the features presented above translate directly into applications described in the next section of this thesis. The main problems currently exhibited by TPV systems are the quality of the TPV converter cells themselves and not efficient enough cooling of the devices. Water cooling could be used for simultaneous heat generation as explained above, while more research needs to be done on improving the crystal quality of the cells.

1.5 Applications of Thermophotovoltaic Systems

When thinking about solar TPV systems, the efficiencies of already existing conventional PV panels greatly exceed what has been demonstrated for TPV cells. Therefore in this case the TPV should be considered more of an addition to the PV rather than a solution on its own. Systems collectively named concentrated solar thermal have been implemented by now, however to our knowledge none of them are using TPV cells. Instead, the generated heat is used for water heating or to power steam engines. Adding TPVs to these systems would improve the total efficiency and increase power generation.

Despite the aforementioned shortcomings of TPVs compared to conventional PVs, multiple TPV systems have been design for solar power conversion. These usually contain selective emitters converting solar spectrum into narrow band radiation compatible with the bandgap of the cell. Dursch and Bitnar [62] proposed a concentrator system with Yb_2O_3 emitter, Si conversion cell and water cooling. Bermel et al. [63] proposed a similar one with a selective emitter at 2360 K and cells with 0.81 eV bandgap, which under 100 times concentration was simulated to reach 54% efficiency. Real-life systems have been constructed by Datas and Algora [64], with Ge cells under concentrated system yielding 0.8% total efficiency, and by Lenert et al. [65] with InGaAsSb cells, carbon nanotubes solar absorber and photonic crystal selective emitter reaching 3.2% efficiency.

The far more important application is conversion of waste heat. Mostly applicable to steel, glass and similar industries, it could significantly improve efficiencies of the

manufacturing processes. Up to half of the heat generated in the production of these materials is wasted,[66] therefore if even a small percentage of it is converted back into electricity it would result in significant power savings. Since the furnaces used in production of glass, steel etc. are heated up to 900-1575°C [67,68], they are perfect sources for TPV systems. So far these industries occasionally use thermoelectric devices to recover some of the waste heat, however they are very inefficient. Therefore developing a TPV system capable of working with these crucibles would be highly beneficial for the aforementioned industries and could largely reduce the amount of power they use.

Another potential application for TPVs is their use in portable power sources like micro power generators. Chia and Feng [69] created a system with GaSb cells and hydrogen fuelled micro-combustor, which yielded less than 1% efficiency. Bermel et al. [63] fuelled their system with butane and oxygen mix and used InGaAsSb 0.55 eV cells achieving efficiency under 1% as well.

Nowadays most of the research is focused on optimising the existing designs of whole systems. Some propose use of photonic crystals [63, 65, 70] for selective emitters and tandem filters to control the spectrum incident on the cells. The focus of this thesis is on development of cells for these systems, which are crucial for achieving high efficiencies, yet very little progress has been made on them in past ten or so years.

1.6 Thesis Structure

In this PhD thesis, the investigation of high-efficiency semiconductor thermophotovoltaic cells is presented with 7 chapters.

The 1st chapter is the introduction to the thermophotovoltaics, including material compositions and structures of such devices, their advantages and disadvantages as well as potential applications.

The 2nd chapter describes operational principles of TPVs including some background information on semiconductors, basic physics of the cells, description of their ideal operation and relevant loss mechanisms.

The 3rd chapter details experimental methods used in the project including epitaxial growth, material characterisation, device fabrication as well as optical and electrical characterisation.

The 4th chapter is about modelling of maximum theoretical efficiencies of GaInAs TPV cells. Various parameters of the structures (architecture, thickness, temperature, defects) have been investigated under different illumination conditions (temperature of the source and incident power density). The implications of those findings for real life devices have been discussed as well.

In the 5th chapter design, growth, fabrication and characterisation of GaInAs TPV cells are discussed. The design has been based on the modelling work presented in chapter 4. Details of MBE growth conditions and fabrication steps are followed by results from dark current measurements, illuminated measurements and photoluminescence study of annealed samples. Finally implications on future work

related to these devices are discussed.

The 6th chapter describes growth of InAs and InAs/InP nanowires by MBE, followed by material and optical characterisation. SEM and TEM results are presented to prove the high quality of the grown structures. Detailed photoluminescence study including temperature-dependent and integrated PL results is reported.

The final chapter is a short summary and conclusion of the work presented in this thesis. The main achievements of each of the chapters are discussed as well as the causal relationships between the chapters. The chapter ends with some ideas for future work based on the materials developed for this thesis.

1.7 References

1. 2014 Key World Energy Statistics, International Energy Agency, accessed on 18th August 2015, http://www.iea.org/publications/freepublications/publication/KeyWorld2014.pdf.
2. https://en.wikipedia.org/wiki/Tonne_of_oil_equivalent, accessed on 18th August 2015.
3. BP: Energy Outlook 2035, accessed on 18th August 2015, http://www.bp.com/content/dam/bp/pdf/Energy-economics/energy-outlook-2015
4. H.H. Kolm, Solar-battery power source, *Quarterly Progress Report* Solid State Research, MIT Lincoln Laboratory, 1956.
5. P. Aigrain, Thermophotovoltaic conversion of radiant energy, unpublished lecture series at MIT, 1960-1961.
6. T.J. Coutts, A review of progress in thermophotovoltaic generation of electricity, *Renewable and Sustainable Energy Reviews* 3, 1999.
7. R.E. Nelson, A brief history of thermophotovoltaic development, *Semicond. Sci. Technol. 18*, 2003.
8. L.M Fraas *et al.*, Over 35% efficient GaAs/GaSb stacked concentrator cell assemblies for terrestrial applications, *Proc. 21st IEEE PV Specialists Conf.*, 1990.
9. R.W. Beck and E.N. Sayers, Study of germanium devices for use in a thermophotovoltaic converter, *Progress Report No 2 (final report)*, DA28-043-AMC-02543(E), General Motors Corporation, 1967.
10. R.J. Schwartz, The theoretical and experimental investigation of planar pin

thermophotovoltaic cells, *Contract No.* DAAB07-70-C-0129, Purdue University, 1971.

11. H. Foll, Semiconductor Technology – Script, III-V Semiconductors, accessed on 23rd November 2015, http://www.tf.uni-kiel.de/matwis/amat/semitech_en/kap_2/backbone/r2_3_1.html.
12. JX Crystals, GaSb cells, accessed on 23rd November 2015, http://jxcrystals.com/drupal/GaSb.
13. D.M. Wilt, N.S. Fatemi, R.W. Hoffman, Jr., P.P. Jenkins, D.J. Brinker, D. Scheiman, R. Lowe, M. Fauer, R.K. Jain, “High efficiency indium gallium arsenide photovoltaic devices for thermophotovoltaic power systems”, *Appl. Phys. Lett. 64*, 1994.
14. M.W. Wanlass, J.S. Ward, K.A. Emery, M.M. Al-Jassim, K.M. Jones, and T.J. Coutts, “$Ga_xIn_{1-x}As$ thermophotovoltaic converters”, *Solar Energy Matererials Solar Cells 41-42*, 1996.
15. M.K. Hudait, C.L. Andre, Kwon, M.N. Palmisiano, and S.A. Ringel, "High-performance In/sub 0.53/Ga/sub 0.47/As thermophotovoltaic devices grown by solid source molecular beam epitaxy," *IEEE Electron Device Lett. 23*, 2003.
16. S. Murray, F. Newman, C. Murray, D. Wilt, M. Wanlass, P. Ahrenkiel, R. Messham, and R. Siergiej, "MOCVD growth of lattice-matched and mismatched InGaAs materials for thermophotovoltaic energy conversion," *Semiconductor Science and Technology 18*, 2003.
17. M.K. Hudait, Y. Lin, D.M. Wilt, J.S. Speck, C.A. Tivarus, E.R. Heller, J.P. Pelz,

S.A. Ringel, "High-quality InAs[sub y]P[sub 1−y] step-graded buffer by molecular-beam epitaxy," *Applied Physics Letters 82*, 2003.

18. M.K. Hudait, "Comparison of mixed anion, InAs[sub y]P[sub 1−y] and mixed cation, In[sub x]Al[sub 1−x]As metamorphic buffers grown by molecular beam epitaxy on (100) InP substrates," *Journal of Appl. Phys. 95*, 2004.
19. M.K. Hudait, Y. Lin, M.N. Palmisiano, and S.A. Ringel, "0.6-eV bandgap In/sub 0.69/Ga/sub 0.31/As thermophotovoltaic devices grown on InAs/sub y/P/sub 1-y/ step-graded buffers by molecular beam epitaxy," *IEEE Electron. Device Lett. 24*, 2003.
20. B. Wernsman, T. Bird, M. Sheldon, S. Link, and R. Wehrer, "Molecular beam epitaxy grown 0.6 eV n⁄p⁄n InPAs⁄InGaAs⁄InAlAs double heterostructure thermophotovoltaic devices using carbon as the p-type dopant," *Journal of Vacuum Science & Technology B: Microelectronics and Nanometer Structures 24*, 2006.
21. J. Cederberg, J. Blaich, G. Girard, S. Lee, D. Nelson, and C. Murray, "The development of (InGa)As thermophotovoltaic cells on InP using strain-relaxed In(PAs) buffers," *Journal of Crystal Growth 310*, 2008.
22. M.K. Hudait, M. Brenner, and S.A. Ringel, "Metamorphic In 0.7 Al 0.3 As/In 0.69 Ga 0.31 As thermophotovoltaic devices grown on graded InAsyP 1− y buffers by molecular beam epitaxy," *Solid State Electron. 53(1)*, 2009.
23. R.S. Tuley, R.J. Nicholas, “Band gap dependent thermophotovoltaic device performance using the InGaAs and InGaAsP material system”, *Journal of Appl.*

Phys. 108, 2010.

24. P. Jurczak, A. Onno. K. Sablon, and H. Liu, Efficiency of GaInAs thermophotovoltaic cells: the effects of incident radiation, light trapping and recombinations, *Optics Express 23(19)*, 2015.
25. D. Jenkins and J. Dow, Electronic properties of metastable Ge_xSn_{1-x} alloys, *Physical Review B 36*, 1987.
26. G. He and H. Atwater, Interband Transitions in Sn_xGe_{1-x} Alloys, *Review Letters 79*, 1997.
27. P. Moontragoon, Z. Ikonic, and P. Harrison, Band structure calculations of Si-Ge-Sn alloys: achieving direct band gap materials, *Semicond. Sci. Technol. 22*, 2007.
28. W.-J. Yin, X.-G. Gong, and S.-H. Wei, Origin of the unusually large band-gap bowing and the breakdown of the band-edge distribution rule in the Sn_xGe_{1-x} alloys, *Phys. Rev. B 78*, 2008.
29. R. Soref, G. Sun, and H. Cheng, Franz-Keldysh electro-absorption in germanium-tin alloys, *J. Appl. Phys. 111*, 2012.
30. R. Ragan and H.A. Atwater, Measurement of the direct energy gap of coherently strained Sn_xGe_{1-x}/Ge (001) heterostructures, *Appl. Phys. Lett. 77*, 2000.
31. S. Takeuchi and A. Sakai, Growth and structure evaluation of strain-relaxed $Ge_{1-x}Sn_x$ buffer layers on virtual Ge substrates, *IEEE Conference Proceedings*, 2006.
32. S. Takeuchi et al., Growth of highly strain-relaxed $Ge_{1-x}Sn_x$ / virtual Ge by a Sn precipitation controlled compositionally step-graded method, *Appl. Phys. Lett. 92*, 2008.

33. S.J. Su et al., GeSn on Si Photodetectors Grown by Molecular Beam Epitaxy, *IEEE Conference Proceedings*, 2010.
34. R. Chen et al., Increased photoluminescence of strain-reduced, high-Sn composition $Ge_{1-x}Sn_x$ alloys grown by molecular beam epitaxy, *Appl. Phys. Lett. 99*, 2011.
35. S. Su et al., The contributions of composition and strain to the phonon shift in GeSn alloys, *Solid State Comm. 151*, 2011.
36. S. Su et al., Epitaxial growth and thermal stability of $Ge_{1-x}Sn_x$ alloys on Ge-buffered Si(001) substrates, *Journal of Crystal Growth 137*, 2011.
37. Y. Huo et al., Strong enhancement of direct transition photoluminescence with highly tensile-strained Ge grown by molecular beam epitaxy, *Appl. Phys. Lett. 98*, 2011.
38. H. Lin, R. Chen, Y. Huo, T. Kamins, and J. Harris, Low-temperature growth of $Ge_{1-x}Sn_x$ thin films with strain control by molecular beam epitaxy, *Thin Solid Films 520*, 2012.
39. H. Lin et al., Investigation of the direct band gaps in $Ge_{1-x}Sn_x$ alloys with strain control by photoreflectance spectroscopy, *Appl. Phys. Lett. 100*, 2012.
40. H. Lin et al., Structural and optical characterisation of $Si_xGe_{1-x-y}Sn_y$ alloys grown by molecular beam epitaxy, *Appl. Phys. Lett. 100*, 2012.
41. H. Lin, Optical properties of $Ge_{1-z}Sn_z$/ $Si_xGe_{1-x-y}Sn_y$ heterostructures, *IEEE Conference Proceedings*, 2012.
42. N. Bhargava, M. Coppinger, J. Gupta, L. Wielunski, and J. Kolodzey, Lattice

constant and substitutional composition of GeSn alloys grown by molecular beam epitaxy, *Appl. Phys. Lett. 103*, 2013.

43. V. Machanov, H.H. Cheng, G. Sun, and R.A. Soref, Mid-infrared electroluminescence from a Ge/$Ge_{0.922}Sn_{0.078}$/Ge double heterostructure pin diode on a Si substrate, *Appl. Phys. Lett.*, 2013.
44. A. Talochkin and V. Machanov, Formation of GeSn alloy on Si (100) by low-temperature molecular beam epitaxy, *Appl. Phys. Lett. 105*, 2014.
45. D'Costa V. et al., Above-bandgap optical properties of biaxially strained GeSn alloys grown by molecular beam epitaxy, *Appl. Phys. Lett. 104*, 2014.
46. M. Bauer et al., Ge-Sn semiconductors for band-gap and lattice engineering, *Appl. Phys. Lett. 81*, 2002.
47. P. Aella et al., Optical and structural properties of $Si_xSn_yGe_{1-x-y}$ alloys, *Appl. Phys. Lett. 84*, 2004.
48. V. D'Costa et al., Optical critical points of thin-film $Ge_{1-y}Sn_y$ alloys: A comparative $Ge_{1-y}Sn_y$/$Ge_{1-x}Si_x$ study, *Phys. Rev. B 73*, 2006.
49. V. D'Costa et al., Sn-alloying as a means of increasing the optical absorption of Ge at the C- and L-telecommunication bands, *Semicond. Sci. Technol. 24*, 2009.
50. G. Grzybowski et al., Next generation of $Ge_{1-y}Sn_y$ (y = 0.01-0.09) alloys grown on Si (100) via Ge_3H_8 and SnD_4: Reaction kinetics and tunable emission, *Appl. Phys. Lett. 101*, 2012.
51. R. Chen et al., Material characterisation of high Sn-content, compressively-strained GeSn epitaxial films after rapid thermal processing,

Journal of Crystal Growth 365, 2013.

52. S. Ghetmiri et al., Shortwave-infrared photoluminescence from $Ge_{1-x}Sn_x$ thin films on silicon, *J. Vac. Sci. Technol. B 32*, 2014.
53. J. Margetis et al., Growth and characterisation of epitaxial $Ge_{1-x}Sn_x$ alloys and heterostructures using a commercial CVD systems, *ECS Transitions*, 2014.
54. M. Oehme et al. GeSn p-i-n detectors integrated on Si with up to 4% Sn. *Appl. Phys. Lett. 101*, 2012.
55. S. Kim et al., Current-Voltage Characteristics of GeSn/Ge Heterojunction Diodes Grown by Molecular Beam Epitaxy, *IEEE Electron. Device Lett. 34*, 2013.
56. M. Oehme et al., Heterojunction LEDs on Si Substrates, *IEEE Photon. Technol. Lett.*, 2014.
57. K. Ye et al., Absorption coefficients GeSn extracted from PIN photodetector response, *Solid-State Electronics*, 2015.
58. C.L. Xue et al., GeSn on Si Photodetectors Grown by Molecular Beam Epitaxy, *IEEE Conference Proceedings*, 2010.
59. S. Wirths et al., Band engineering and growth of tensile strained Ge/ (Si) GeSn heterostructures for tunnel field effect transistors, *Appl. Phys. Lett. 102*, 2013.
60. S. Wirths et al., Epitaxy and Photoluminescence Studies of High Quality GeSn Heterostructures with Sn Concentrations up to 13 at.%, *IEEE Conf. Proceedings*, 2014.
61. F. Oliveira et al., Multi-stacks of epitaxial GeSn self-assembled dots in Si: Structural analysis, *J. Appl. Phys. 117*, 2015.

62. W. Durisch and B. Bitnar, Novel thin film thermophotovoltaic system, *Sol. Energ. Mat. Sol. C,* 2010.
63. P. Bermel et al., Design and global optimization of high-efficiency thermophotovoltaic systems, *Optics Express*, 2010.
64. A. Datas and C. Algora, Development and experimental evaluation of a complete solar thermophotovoltaic system, *Progress in Photov.: Research and Appl.*, 2013.
65. A. Lenert, D.M. Bierman, N. Youngsuk, W.R. Chan, I. Celianovic, M. Soliacic, and E.N. Wang, A nanophotonic solar thermophotovoltaic device, *Nature Nanotechnology*, 2014.
66. Glass industry technological roadmap (USA), accessed April 2015, http://www.energetics.com/resourcecenter/products/roadmaps/Pages/Glass-Industry-Roadmap.aspx.
67. B.H.W.S. de Jong, Glass, Ullmann's Encyclopedia of Industrial Chemistry, 5th edition, vol. A12, VCH Publishers, Germany, 1989.
68. Making iron, The chemistry of steelmaking, accessed on 8th December 2015, http://resources.schoolscience.co.uk/Corus/14-16/steel/msch2pg2.html.
69. L. Chia and B. Feng, The development of a micropower (micro-thermophotovoltaic) device, *Journal of Power Sources*, 2007.
70. Y.X. Yeng, Performance analysis of experimentally viable photonic crystal enhanced thermophotovoltaic systems, *Optics Express*, 2013.

Chapter 2:

Operational Principles of TPVs

A comprehensive understanding of thermophotovoltaic cells requires an insight into the interactions between electromagnetic radiation and semiconductors. This chapter describes the principles of blackbody radiation and photovoltaic energy conversion. A brief introduction on semiconductors physics, p-n junctions and ideal cell operation is followed by a description of loss mechanisms and their impact on the TPV cells.

2.1 Physics of the Cells

2.1.1 Thermal Emitters

Conventional photovoltaic cells receive the incident radiation from the sun at a temperature of 5777 K from a distance of 150×10^{9} m, while the TPVs operate with thermal emitters at temperatures of 1000-1800 K placed from several nanometres up to a few centimetres from the cell [1]. This results in power densities incident on TPV cells being much higher than those on solar cells, usually about 50 to 500 kW/m^2 compared to 1kW/m^2 of the solar spectrum [2]. Thermal emitters used for TPV systems emit infrared radiation around 2-3 μm. Their spectra can be approximated as radiation spectra of a blackbody at a specific temperature and described using Planck's formula[3]:

$$b(E) = \frac{2n_r^2E^2}{h^3c^2} exp\left(\frac{-E}{kT}\right) \quad \text{2-1}$$

where E is the energy of emitted photons, n_r is the ambient refractive index, h is Planck's constant, c is the speed of light, k is the Boltzmann's constant and T is the temperature of the blackbody. Figure 2.1 shows spectra of blackbody emission for a range of temperatures typical for thermal sources used with TPVS, between 1000 and 1800 K, plotted as intensity of radiation versus the wavelength of emitted photons.

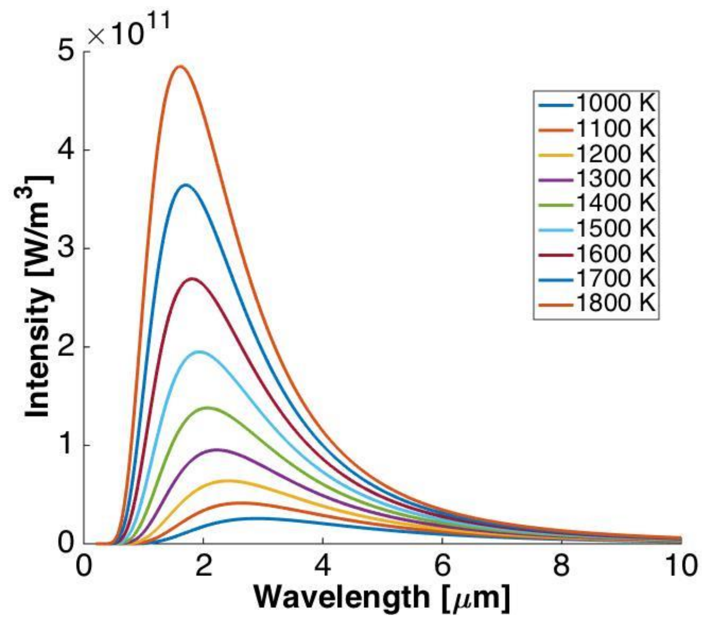

Figure 2.1. Intensity of blackbody radiation at a range of temperatures from 1000 to 1800 K as a function of the wavelengths of emitted photons.

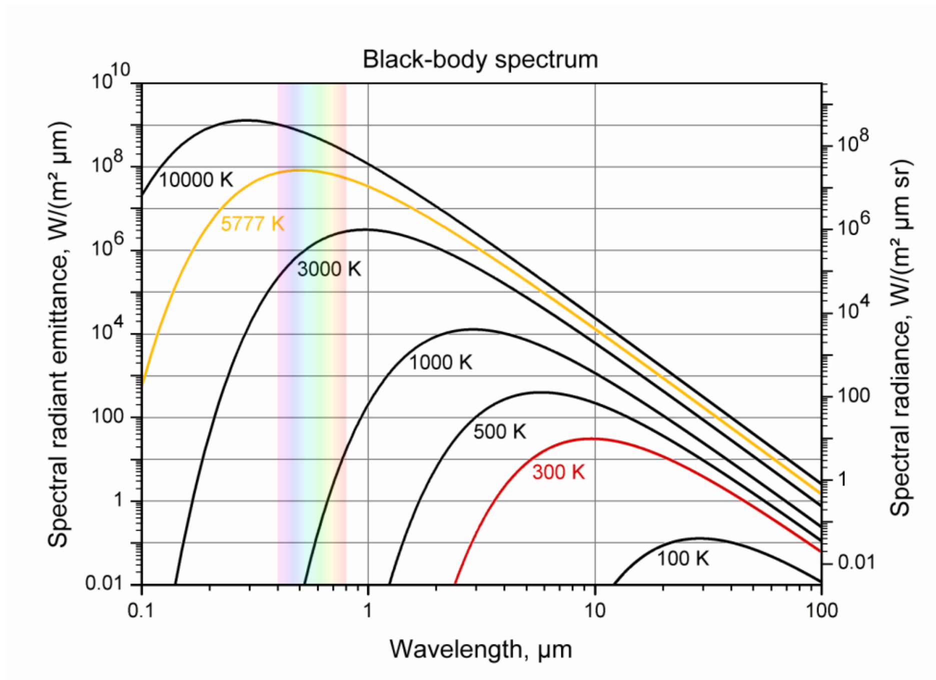

Figure 2.2. Spectra of black bodies at temperatures ranging from 100 to 10000 K including room temperature (red line) and solar spectrum (yellow line) as a function of the wavelengths of emitted photons. [4]

As can be observed from Figure 2.1, the intensity of the emission increases with the temperature of the blackbody emitter and the highest emission peak shifts towards shorter wavelengths. Since the solar spectrum can be approximated as a blackbody source at around 5777 K, it is easy to compare the spectra of TPV emitters and solar irradiation. Figure 2.2 shows blackbody emission spectra for a wide range of emitter temperatures, from 100 to 10000 K. It can be observed that the difference between highest emission wavelengths at around 5777 K and around 1000 K is large. Peak emission from solar spectrum comes at wavelengths between 400 and 800 nm whilst the peak emission from a typical TPV emitter is centred between 2 and 4 μm (see Figure 2.1.). Therefore for optimum efficiency the bandgaps of TPV cells need to be much lower than those of solar cells. More details on the impact of bandgap on cell efficiency can be found in section 2.2.3.

2.1.2 Basics of Semiconductors

Semiconductor materials have electronic bandgaps (“forbidden” states between the valence and conduction band) larger than conductors but smaller than insulators, which allows them to conduct electricity under specific conditions. At room temperature, with no applied bias, only few electrons have sufficient energy to jump from the valence band to the conduction band, making the semiconductor a weak insulator. More electrons can be promoted to the conduction band by applying electrical bias, which lowers the bandgap and hence improves the conductivity. Another way of exciting electrons to the conduction band is by illuminating the

semiconductor with electromagnetic radiation, i.e. light or heat. This is the basis of photovoltaic and thermophotovoltaic energy conversion. Photons with energy E_{ph} equal to or higher than the bandgap E_g are absorbed into the material. Their energy is used to break up covalent bonds and create electron-hole (E-H) pairs, giving the freed electron enough energy to jump to the conduction band. Photons with energies lower than E_g are not absorbed and excess energy of photons with E_{ph} higher than the bandgap is dissipated as heat in the lattice. If the electrons created in this process are not extracted soon enough, they will recombine with the holes. This will reduce the efficiency of energy conversion within the semiconductor. These recombination processes are enhanced by defects and impurities in the crystal lattice acting as recombination centres.

Depth of absorption varies with the energy of incoming photons. High energy ones are absorbed close to the surface while lower energy ones deeper in the material. The number of created E-H pairs per unit volume can be estimated using the generation rate equation [5]:

$$G(x) = \alpha N_0 \exp(-\alpha x) \qquad \text{2-2}$$

where N_0 is the photon flux at the surface (photons per unit area per second), α is the absorption coefficient and x is distance into the material.

The absorption coefficient determines how far a particular wavelength can penetrate into the material before it is absorbed. The absorption spectra of specific materials are usually empirically measured. Examples of absorption coefficients of various semiconductor materials are shown in Figure 2.3.

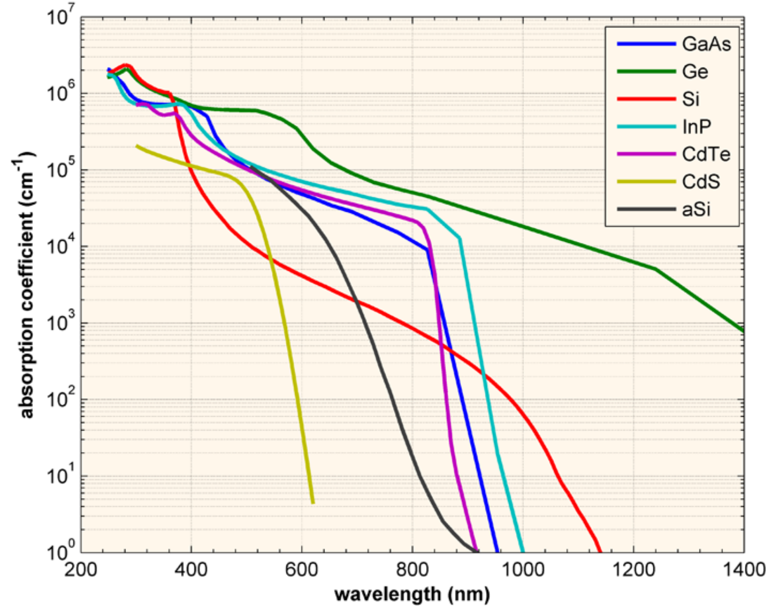

Figure 2.3. The absorption coefficient in a variety of semiconductor materials at 300 K as a function of the vacuum wavelength of light. [5]

The absorption coefficient can also be calculated using the absorption model for semiconductors derived by Yablonovitch et al. [3]:

$$\alpha(E) = \begin{cases} \alpha_0 exp\left(\frac{E - E_g}{E_0}\right), E \leq E_g \\ \alpha_0 \left(1 + \frac{E - E_g}{E'}\right), E > E_g \end{cases} \quad \text{2-3}$$

where α_0 is the absorption coefficient near the band edge and E_0 is the Urbach energy. This model gives a good approximation of absorption coefficients of specific compositions of compound semiconductor materials that have not been empirically measured. It has been used to simulate the absorption spectra of various compositions of GaInAs in the work presented in Chapter 4 of this thesis. Figure 2.4 shows the absorption coefficient spectra of a range of GaInAs compositions, calculated using formula 2-3, as a function of photons energy.

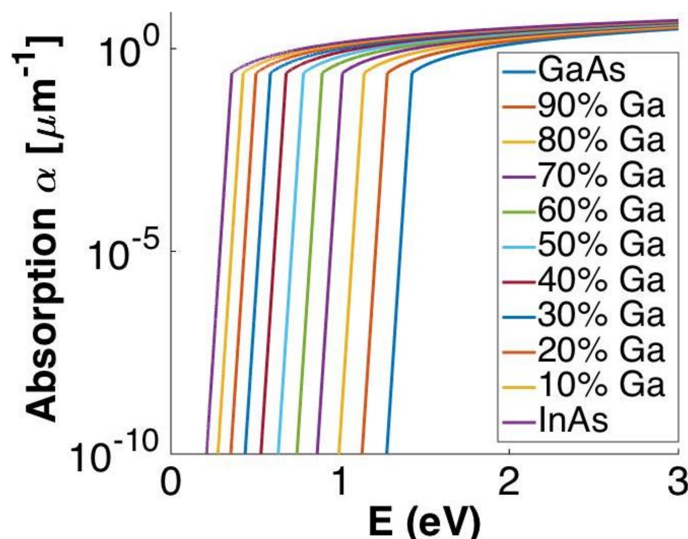

Figure 2.4. The absorption coefficient of various compositions of GaInAs at 300 K as a function of the energy of the photons.

2.1.3 P-N Junction

The p-n junction forms the basis of many electronic and photonic devices such as transistors, LEDs, solar cells, lasers and photodiodes. It is formed by joining a p-type (doped for high holes density) and n-type (doped for high electrons density) semiconductor materials. The two materials in the junction behave differently than each of them separately. Most importantly, the current will only flow in one direction. When the two materials are joined, electrons from the n-type side diffuse into the p-type and analogously holes from the p side diffuse into the n side. When the carriers diffuse to the opposite sides, they leave behind exposed opposite charge on dopant atoms sites fixed in the crystal lattice of the material. The positive ion cores on the n side and the negative ones on the p side establish an electric field across the junction.

There are no free carriers left in this region (at equilibrium, i.e. no bias applied) and hence it is called the depletion zone. Details of this process are illustrated in Figure 2.5.

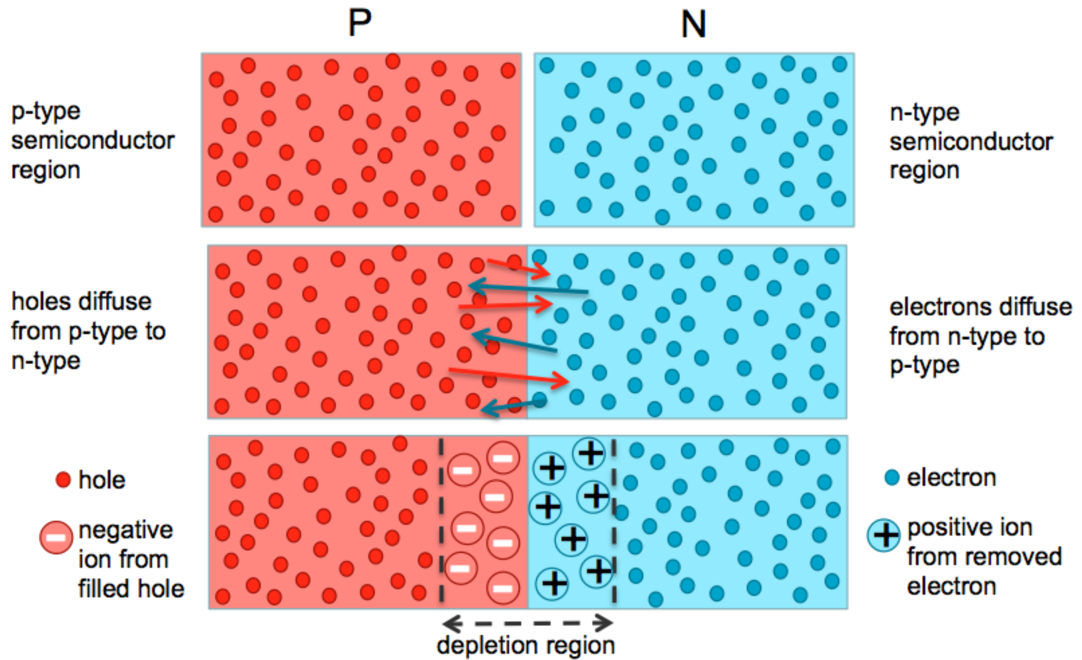

Figure 2.5. Illustration of the formation of a P-N junction.

In order to reduce the strength of the electric field across the junction, forward bias voltage is applied. If reverse bias is applied, the field is increased creating a higher barrier for the carriers and reducing the current flow. Figure 2.6 illustrates the band diagram of a p-n junction at thermal equilibrium and when the two types of bias are applied [6].

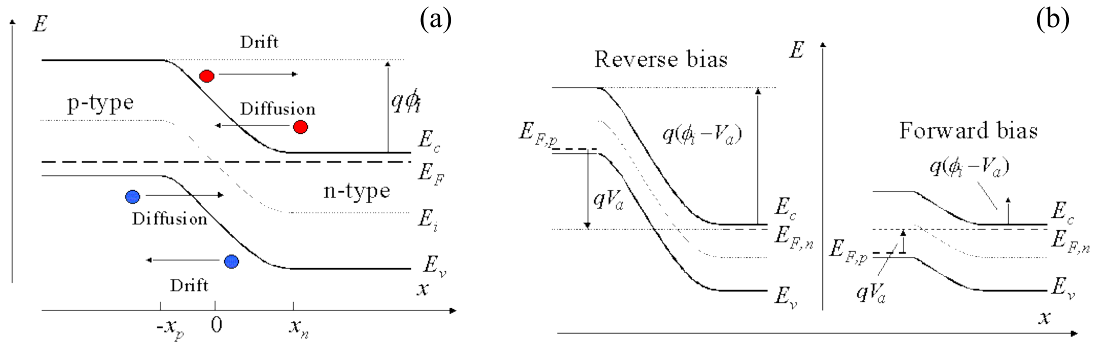

Figure 2.6. The band diagrams of p-n junction at thermal equilibrium (a) and under reverse and forward bias (b) [6].

The flow of current in a p-n junction as a function of voltage is described by the diode equation. It has been derived by Shockley and assumes that the junction is abrupt and there is no recombination or generation in the depletion region. The Shockley J_D current, referred to as dark current (without illumination) in solar cells related applications including TPVs, can be described as [7]:

$$J_D = J_0\left(exp\left(\frac{qV}{nkT}\right) - 1\right) \qquad \text{2-4}$$

where J_0 is the diode leakage current in the absence of light ("dark saturation current"), q is the charge of an electron, V is the applied voltage, n is the ideality factor (n=1 for an ideal diode), k is the Boltzmann's constant and T is the temperature of the diode.

2.2 Cell Operation

2.2.1 Ideal Cell Operation

A TPV cell is an electronic device that converts heat (infrared radiation) directly into electricity. The physics behind an operation of a thermophotovoltaic cell is the

same as for solar cells. During the operation of a TPV cell, photons emitted by the heat source are absorbed within the semiconductor leading to generation of free carriers (electron-hole pairs). Then the carriers are collected at opposite terminals creating current flow, potential difference is generated across the cell and finally the power is dissipated in an external load. Figure 2.7 shows a cross section of a typical semiconductor p-n junction TPV cell.

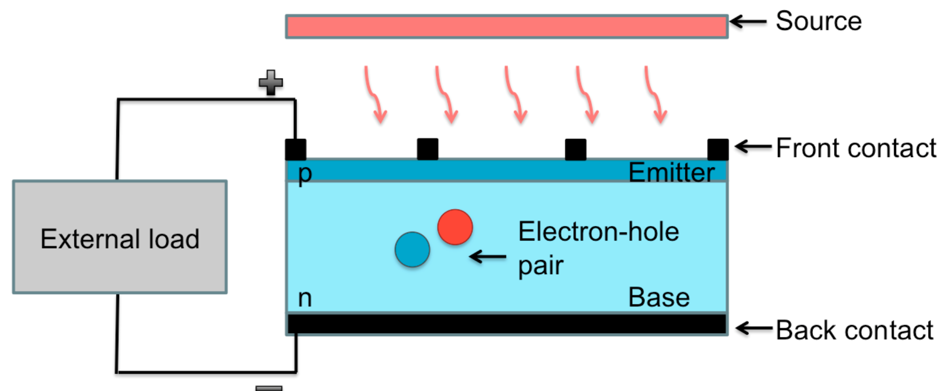

Figure 2.7. Cross-section of a TPV cell.

The first process in generation of light-generated current is the absorption of the incident photons in order to create the E-H pairs. Details of absorption process in semiconductors have been described in section 2.1.2 of this chapter. Lifetimes of the minority carriers (electrons in the p-type material and holes in the n-type material) are very short and the carriers can easily recombine annihilating the photo-generated E-H pair and preventing generation of power within the cell. Therefore a second process, collection of the generated carriers before they recombine, is necessary for efficient operation of the cell. The main technique of efficient extraction of carriers is use of a

p-n junction. The photo-generated carriers are spatially separated by the electric field established across the junction (see section 2.1.3 of this chapter for details). They are swept across the junction and become majority carriers. If the emitter and the base are connected (short-circuit), the carriers generated in this process flow through the external circuit and hence current is generated. The probability of collection can be further enhanced if the carriers are generated within the diffusion length of the junction, which minimises the probability of them recombining. The photo-generated (light-generated) current density can be described as

$$J_L = q\int_0^W G(x)CP(x)dx \qquad 2\text{-}5$$

where W is the thickness of the cell, $G(x)$ is the generation rate (Eq. 2-2) and $CP(x)$ is the collection probability at depth x into the material.

In order to generate power, not only current needs to be generated within a cell but also voltage needs to be established between the opposite terminals. In a photovoltaic cell the voltage is generated by the photovoltaic effect. The collection of carriers in a p-n junction causes the electrons to move to the n-type side and the holes to the p-type side. If the emitter and the base are connected (short-circuit), there is no build-up of charge and hence no potential difference between the two terminals. However, if the carriers are prevented from leaving the cell, they will accumulate on opposite sides and this separation of positive and negative charges will cause formation of an electric field at the junction, opposite to the one already established during the depletion region formation (see section 2.1.3). The net electric field is then reduced increasing the diffusion current leading to a new equilibrium. The total current

from the cell is equal to the difference between the dark current J_D and the light generated current J_L:

$$J = J_D - J_L = J_0\left(exp\left(\frac{qV}{nkT}\right) - 1\right) - q\int_0^W G(x)CP(x)dx \quad \text{2-6}$$

Figure 2.8 shows the equivalent circuit of an ideal photovoltaic cell. It consists of a current source, representing the photo-generation of current, in parallel with a rectifying diode representing the radiative recombination process.

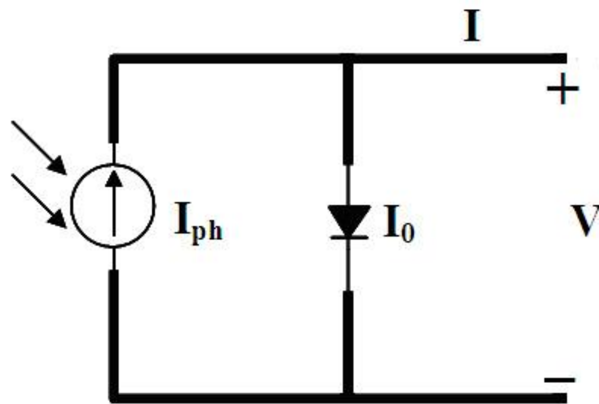

Figure 2.8. An equivalent circuit of an ideal single junction photovoltaic cell [8].

2.2.2 Loss Mechanisms

There are two main types of loss mechanisms in real-life PV and TPV cells, optical losses and electrical losses. Main optical losses include reflection off the front surface of the cell, shadowing by the top contacts, sub-bandgap losses and lattice thermalisation by high-energy photons. Reflection losses can be minimised by texturing the surface of the cell in order to accept photons coming from a large variety of incident angles and randomise the angle at which they enter the cell. Together with a back surface reflector, surface texturing can be used to significantly extend the optical path of photons inside the semiconductor and hence further improve the

absorption probability. This technique is called light trapping.

Shadowing from the top contacts is hard to avoid unless transparent materials are used. With metal contacts the only way to limit this loss is to minimise the area of the front contacts. Sub-bandgap losses originate from the fact that photons with low energy will not be absorbed in the cell, therefore not all of the incident spectrum can be used which results in reduction of the output current. It is hard to circumvent this issue with single junction cells, however multiple cells with different bandgaps connected in parallel can be used to maximise the absorption spectrum (multi-junction cells). Electrons with high energies cause the last of the optical losses, lattice thermalisation. Energy equal to the bandgap of the material is used to excite an electron to the conduction band while the excess energy is dissipated as heat. This causes an increase in the temperature of the cell causing generation of more defects, lowering the bandgap and hence reducing the output voltage.

The electrical losses can be divided into two main categories, recombination losses and parasitic resistance losses. There are several main recombination mechanisms. First of them is radiative recombination, also known as spontaneous emission. In this case, an electron spontaneously relaxes from the conduction band to the valence band, releasing a photon. In photovoltaic cells this happens if the generated carriers are not extracted quickly enough and reduces the efficiency of the cell since no power can be drawn. There are several non-radiative recombination processes, i.e. when the energy from electron and hole recombination is released in a different form than a photon. For TPVs the most important one is Auger

recombination since it is most significant in low bandgap materials with higher carrier densities, where the interactions between carriers are stronger. In Auger recombination two similar carriers collide, one of which is excited to a higher kinetic energy and the other recombines across the bandgap giving its energy to another carrier. Eventually the excess energy is lost as heat contributing to thermalisation of the lattice. The Auger recombination is unavoidable since it is intrinsic to the physical processes within the material. Other type is Shockley-Read-Hall (SRH) recombination involving trap states in the band gap. Trap states “capture” free carriers slowing down the carrier transport through the material. They can be released through thermal activation or annihilated if an opposite charge is captured before the first one is released. In the second case the traps are called recombination centres. Trap states arise from defects in the crystal lattice of the semiconductor. These can be caused for example by thermal cracking, surface states or lattice mismatch between subsequent layers resulting in stress build-up and hence formation of dislocations.

There are two types of parasitic resistances within photovoltaic cells. Series resistance has three causes: movement of carriers through the cell, contact resistance between the semiconductor and the metal and the resistances of the metal contacts themselves. It reduces the fill factor of the cell (see section 2.2.3) and can also negatively affect the short-circuit current. Low shunt resistance, resulting usually from fabrication errors, provides alternative current path for the photo-generated current. This reduces the amount of current flowing through the p-n junction and lowers the voltage across the cell resulting in significant power loss. Taking into

account the resistive losses, an equivalent circuit of an ideal diode can be updated, as shown in Figure 2.9.

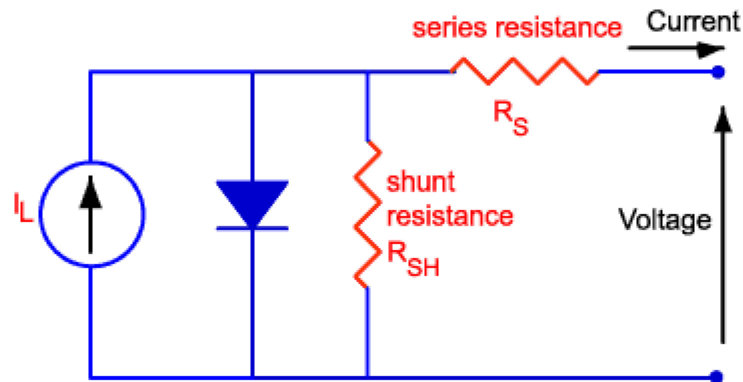

Figure 2.9. An equivalent circuit of a non-ideal single junction photovoltaic cell [9].

2.2.3 Performance Parameters

Quantum Efficiency

The quantum efficiency (Q.E.) describes how efficiently the incoming radiation is converted into electricity. Specifically, it is the ratio of carriers collected from the solar cell to the number of incident photons of certain energy. An example of a quantum efficiency plot is shown in Figure 2.10.

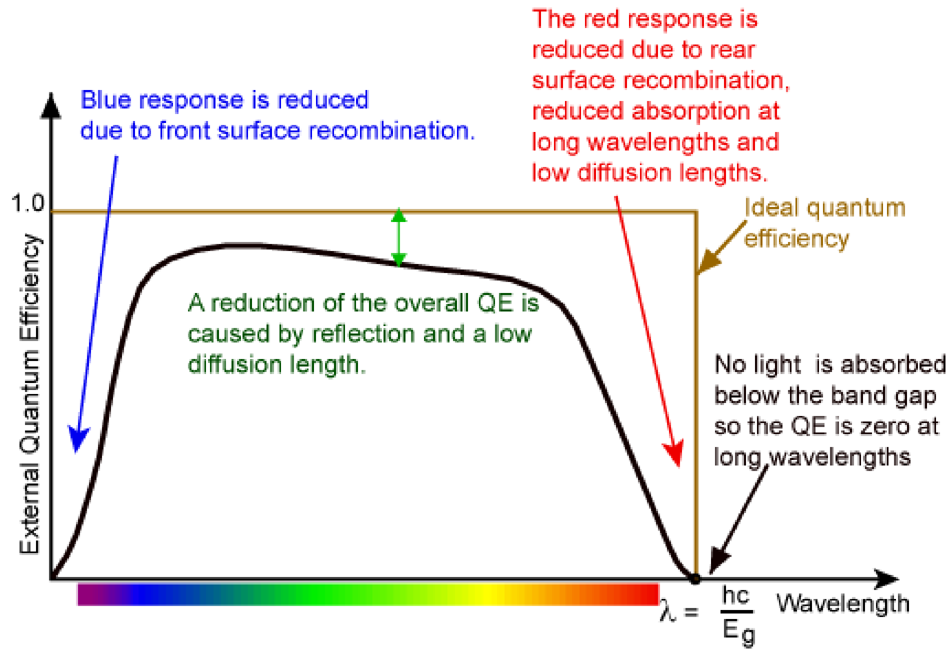

Figure 2.10. An example of quantum efficiency plot (single junction silicon solar cell) vs. ideal quantum efficiency as a function of the wavelength of incoming photons [9].

In an ideal case, if all the photons at a specific wavelength are absorbed and resulting carriers are extracted, the Q.E. is equal to 1. No light is absorbed below the bandgap so the E.Q. is zero for longer wavelengths. For real cells the quantum efficiency is reduced due to recombination effects. The annotations on Figure 2.10 explain in detail which processes are responsible for reducing the Q.E. at specific wavelengths.

External quantum efficiency (E.Q.E.) is often measured for practical devices. It includes the optical losses such as reflection off the front surface. It allows for realistic estimation of the performance of fabricated cells after all loss mechanisms have been included. By measuring the reflectance and transmission of the devices, the internal quantum efficiency (I.Q.E.) can be calculated from the E.Q.E. results.

Short-Circuit Current

The short-circuit current (I_{sc}) is the maximum current that can be extracted from a PV cell. It is the current through the cell when it is short-circuited, i.e. when the voltage across the cell is zero. For an ideal cell the short-circuit current is equal to the light-generated current (Eq. 2-5).

The short-circuit current depends mainly on the area of the cell, the incident power density (i.e. number of photons), the spectrum of the incident radiation, the absorption and reflection of the cell and the collection probability. In order to remove the dependence on the area of the cell and be able to more accurately compare similar devices, the short-circuit current density J_{sc} is often used instead of I_{sc}.

Open-Circuit Voltage

The open-circuit voltage (V_{oc}) is the maximum voltage that can be produced by a PV cell and is achieved at zero current. It depends mostly on the light-generated current I_L and the dark saturation current I_0. The I_0 depends on the recombination in the cell and hence the V_{oc} is a measure of the amount of recombination. The V_{oc} can be described as:

$$V_{oc} = \frac{nkT}{q} ln\left(\frac{J_{sc}}{J_0} + 1\right) \qquad 2\text{-}7$$

where n is the ideality factor, k is the Boltzmann constant, T is the temperature of the cell and q is the charge of an electron.

J-V Curve

The J-V curve is one of the most important pieces of information used to characterise the performance of a photovoltaic cell. It is the superposition of the dark J-V curve and the light-generated current J_L, as described by Eq. 2-6. It can be used to determine some important parameters of the cell like short-circuit current and open-circuit voltage. The fill factor and the efficiency of a cell, described below, are also obtained from the J-V curve. Figure 2.11 shows a typical I-V curve of a solar cell. The general shape of the curve is the same for other p-n diode devices including the TPVs. Conventionally, the current density is inverted to bring it into the first quadrant.

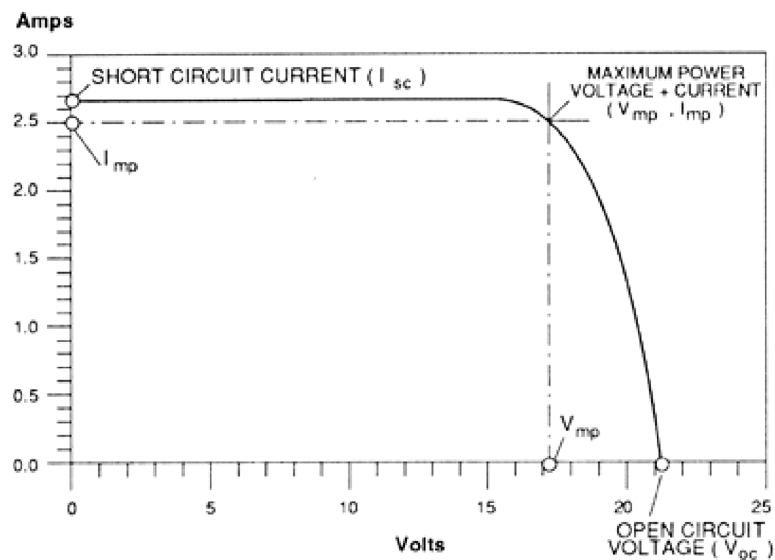

Figure 2.11. An I-V curve of a typical solar cell plotted in conventional way showing the open-circuit voltage, the short-circuit current and the maximum power point [10].

Fill Factor

At the points of maximum voltage (V_{oc}) and maximum current (J_{sc}), the power from the solar cell is zero. The fill factor (FF), together with V_{oc} and J_{sc}, is used to

determine the maximum power output of the cell. It measures the quality of the p-n junction and series resistance of the cell. It is defined as:

$$FF = \frac{J_{mp}V_{mp}}{J_{sc}V_{oc}} \quad \text{2-8}$$

where J_{mp} and V_{mp} are respectively the voltage and the current density at the maximum power point. Figure 2.12 illustrates how the fill factor is obtained from power and J-V curves. The maximum power density can be calculated using the fill factor as:

$$P_{max} = J_{sc}V_{oc}FF \quad \text{2-9}$$

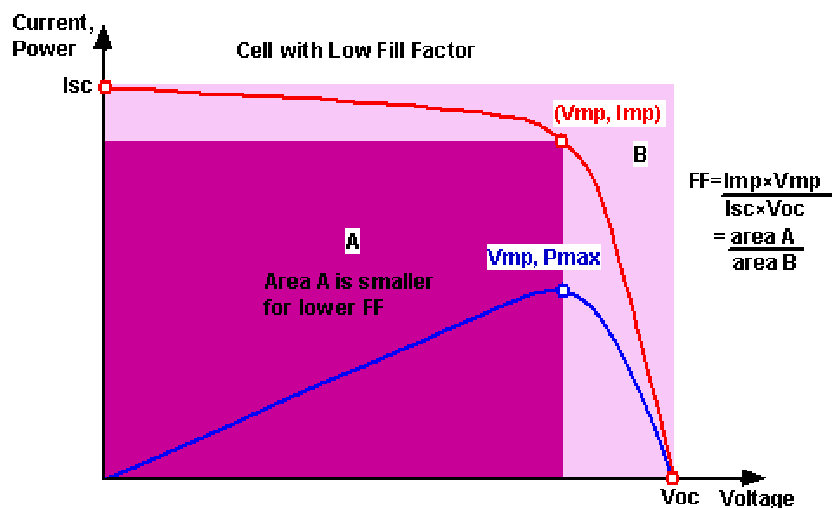

Figure 2.12. Output power (blue) and current (red) as a function of voltage in a typical solar cell [9].

Efficiency

Efficiency is usually the most important parameter used to compare performances of cells. It is defined as the ratio of the energy outputted by the cell and

the input energy delivered to the cell:

$$\eta = \frac{P_{max}}{P_{in}} = \frac{J_{sc}V_{oc}FF}{P_{in}} \quad 2\text{-}10$$

The efficiency depends not only on the quality of the cell itself but also on the intensity of the incident radiation (power density) and the temperature of the cell. Therefore the measurements are performed in controlled conditions in order to obtain comparable results. For solar cells the AM1.5 solar spectrum with 1 kW/m^2 incident power is normally used, while for TPV measurements a blackbody source is used where the power density depends on the temperature of the source and the aperture size used (see section 2.1.1 for details on blackbody radiation). The practical measurement of cell efficiency via measuring its J-V curve is described in section 3.3.2.

For cells with low bandgaps, like TPVs, the J_{sc} is increased because photons with lower energies are absorbed. However, the V_{oc} is lower due to increase in the dark current density. The relations are opposite for cells with high bandgaps. Since these two parameters are included in the efficiency calculation, there has to be an optimum bandgap to obtain highest efficiency. This optimum bandgap varies with the incident spectrum, i.e. the higher the temperature of the source, and hence the energy of most photons, the larger the bandgap is required for best performance (see section 2.1.1). Therefore in case of TPVs the cells have to be designed so that their bandgap matches the temperature of the specific source they will be used with.

2.3 References

1. T.J. Coutts, A review of progress in thermophotovoltaic generation of electricity, *Renewable and Sustainable Energy Reviews* 3, 1999.
2. R.S. Tulley and R.J. Nicholas, Band gap dependent thermophotovoltaic device performance using the InGaAs and InGaAsP material system, *Journal of App. Phys. 108*, 2010.
3. O. Miller, E. Yablonovitch, and S. Kurtz, Strong Internal and External Luminescence as Solar Cells Approach the Shockley-Queisser Limit, *IEEE Journal of Photovoltaics 2*, 2012.
4. Black-body spectrum for temperatures between 300 K and 10,000 K in a log-log diagram, accessed on 19th November 2015, https://commons.wikimedia.org/wiki/File:BlackbodySpectrum_loglog_150dpi_en.png
5. C. Honsberg and S. Bowden, Generation rate, accessed on 4th November 2015, http://www.pveducation.org/pvcdrom/pn-junction.
6. B. Van Zeghbroeck, Principles of Semiconductor Devices, Chapter 4: p-n Junctions, University of Colorado Boulder, 2011, accessed on 13th November 2015, http://ecee.colorado.edu/~bart/book/book/chapter4/ch4_2.htm.
7. W. Shockley, The theory of pn junctions in semiconductors and pn junction transistors, *Bell Syst. Tech. J.,* 1949.
8. Y. Zhao *et al.*, A solar photovoltaic system with ideal efficiency close to the theoretical limit, *Opt. Express 20*, 2012.

9. C. Honsberg and S. Bowden, Solar Cell Operation, accessed on 17th November 2015, http://www.pveducation.org/pvcdrom/pn-junction.

10. D. Darling, I-V curve of a photovoltaic device, accessed on 18th November 2015, http://www.daviddarling.info/encyclopedia/I/AE_I-V_curve.html.

Chapter 3:

Experimental Methods

This chapter describes in detail all the experimental methods used in this project. The devices are designed and grown at the Department of Electronic and Electrical Engineering at UCL using the Veeco Gen930 solid-source molecular beam epitaxy. Material characterisation is performed using AFM at UCL, SEM at London Centre for Nanotechnology (LCN) and TEM at Universidad de Cádiz, Spain. The LCN cleanroom facilities are used for fabrication of test TPV devices. Photoluminescence and dark J-V measurements are performed at UCL and blackbody illuminated J-V at the US Army Research Laboratories (ARL).

3.1. Epitaxial Growth

There are several methods used to grow semiconductor materials of desired compositions. During epitaxial growth crystalline materials are deposited on a crystalline substrate. The most popular techniques used for this growth are multiple variants of Chemical Vapour Deposition (CVD) and Molecular Beam Epitaxy (MBE). While CVD methods are favoured by industries due to low cost and high throughput, MBE offers a unique level of precision by controlling deposition at atomic scale and allows adjustment of a wide range of growth parameters. Hence MBE is a better choice for research purposes and all the devices produced for this PhD project are grown with this method. In order to assess morphology and crystal structure of the grown materials, high-resolution imaging equipment is used such as atomic force microscope (AFM), scanning electron microscope (SEM) and transmission electron microscope (TEM).

3.1.1 Molecular Beam Epitaxy

Molecular beam epitaxy is an epitaxial growth method where atoms and molecules are beamed from effusion cells onto a crystalline surface [1-4]. The growth is carried in an ultra-high vacuum environment and the substrate is heated to a few hundred degrees Celsius, precise values depending on the material being grown. It was invented in the late 1960s at Bell Labs by J.R. Arthur and A.Y. Cho [5]. Until now, several variations of MBEs have been developed such as solid-source MBE, gas-source MBE and metal-organic MBE. Figure 3.1 shows the Veeco Gen930 solid-

source MBE used to grow III-V TPV cells for this thesis. The system used for growth of group-IV materials is also a Veeco Gen930 MBE.

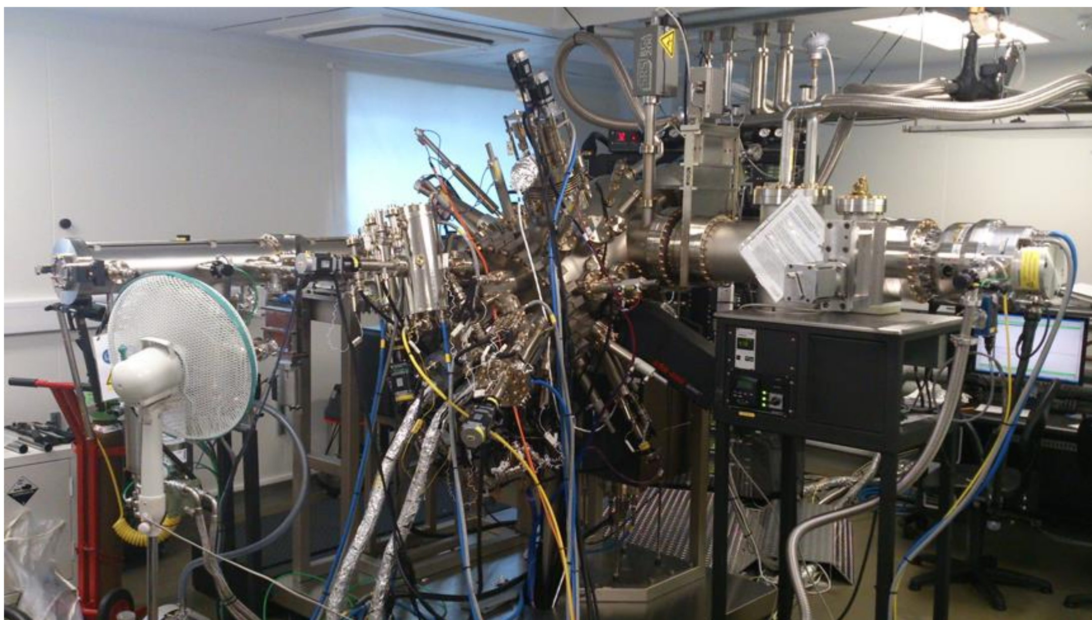

Figure 3.1. Veeco Gen930 solid-source MBE.

The Veeco Gen930 systems have three main vacuum chambers: the loadlock chamber, the prep chamber and the growth chamber. A phosphorus recovery system has been added to the group III-V system in order to minimise the safety and environmental hazards related to use of phosphorus. The chambers are separated with ultra-high vacuum (UHV) gate valves to prevent cross-contamination.

The loadlock (LL) chamber is used to load wafers and unload grown samples without affecting the UHV environment in the other chambers. It is also used for preliminary outgassing of new samples. During that process the chamber is heated up to 100-200°C by two quartz infrared lamps mounted inside. This helps to remove water and hydrocarbon contaminants from the wafer. The vacuum level in the

loadlock is normally maintained around 10^{-8} Torr. Usually a turbo and scroll pump configuration is used for rough pumping the LL, where the scroll pump provides backing for the turbo pump. These pumps are also used to rough pump the other chambers from atmospheric pressure to high vacuum. A cryogenic pump is usually attached to the LL as well in order to improve the vacuum capability, but it is only opened at high vacuum levels.

The prep chamber is used as a buffer between the loadlock and growth chamber. It can also be used for degassing but at much higher temperatures than in the LL, up to 600°C. This allows removal of virtually all evaporable contaminants such as hydrocarbons or water, as well as substrate oxide. Because the heater in the prep chamber is separate from the one in the growth chamber, thermal preparation of substrates can be carried out while another sample is being grown. The prep chamber is also used as a storage chamber for wafers before and after growth. Because this chamber has direct contact with the growth chamber, the vacuum needs to be maintained at UHV levels, usually up to 5×10^{-10} Torr. Rough pumping for the prep chamber is carried out through the loadlock, while the UHV levels are reached using an ion pump integrated with titanium sublimation pump (TSP).

In the growth chamber there is a heated substrate stand, substrate manipulator, a thermocouple, effusion cells, liquid nitrogen cooled cryopanels and various analytical instruments. A schematic of an MBE growth chamber is shown in Figure 3.2.Vacuum level in this chamber can reach order of 10^{-11} Torr. Usually a closed-loop helium cryogenic pump is used to maintain UHV levels in the growth chamber

because it provides fast, high capacity pumping for a wide range of vapours. However, it needs to be regularly regenerated by pumping out the trapped gases. Ion pump and TSP are also often used to provide pumping of a range of active and noble species. Cryopanels with a coolant like liquid nitrogen or water-alcohol solution running inside it are used to provide stable temperature environment for the cells. Due to their cryogenic temperature volatile species in the chamber “stick” to the panels, which further improves the vacuum and helps with minimising incorporation of contaminants into the grown structures.

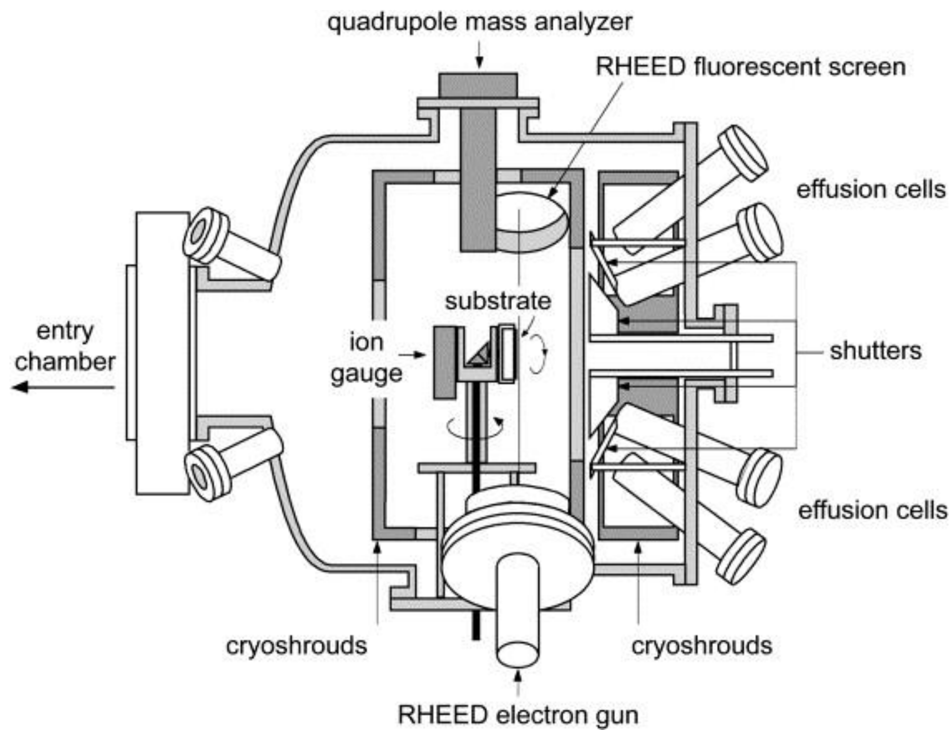

Figure 3.2. Schematic diagram of the MBE growth chamber [6].

Knudsen cells (K-cells) are the standard effusion sources for most solid-source MBE systems. They consist of a heating element surrounded by a heat shield and a

crucible thermocouple. Some cells also include a water jacket for more efficient cooling. A schematic of a typical K-cell is shown in Figure 3.3. Source materials are placed in a crucible and fitted into the heating assembly. Large capacity cells (up to 200cc) are used for the main evaporants, which in our III-V MBE system include indium, gallium and aluminium and in the group-IV system germanium and tin. Smaller cells, usually around 5cc, are used for doping materials like silicon, beryllium and boron.

Group V species such as arsenic, phosphorus or antimony require use of so called cracking cells, which apart from the standard thermal K-cell also include a second heating zone. In this zone, also called a cracking zone, tetramers such as e.g. As_4 are broken into two dimers (e.g. As_2). This process is beneficial because the smaller molecules have significantly higher sticking coefficients than the bigger molecules therefore they are easier incorporated into the grown crystal and cause less defects.

For efficient deposition of silicon from solid source, because of its high evaporation temperature, electron beam evaporators are used. The main elements of such a system include an electron beam source and a pocket with source material placed in a separate vacuum chamber connected to the growth chamber via an UHV valve. Usually a mirror inside the chamber is used to guide the electron beam onto the source material. Efficient water cooling is required to maintain safe operation temperature of the e-beam evaporator.

In order to control the molecular beams of the evaporated species, shutters are

mounted in front of each source flange. Our systems use pneumatic blade shutters with actuation time of less than 300 ms ensuring swift interruption of the beam flux. This allows for growth of sharp interfaces with atomic precision. For most precise operation pre-programmed computer controls are used to open and close the shutters.

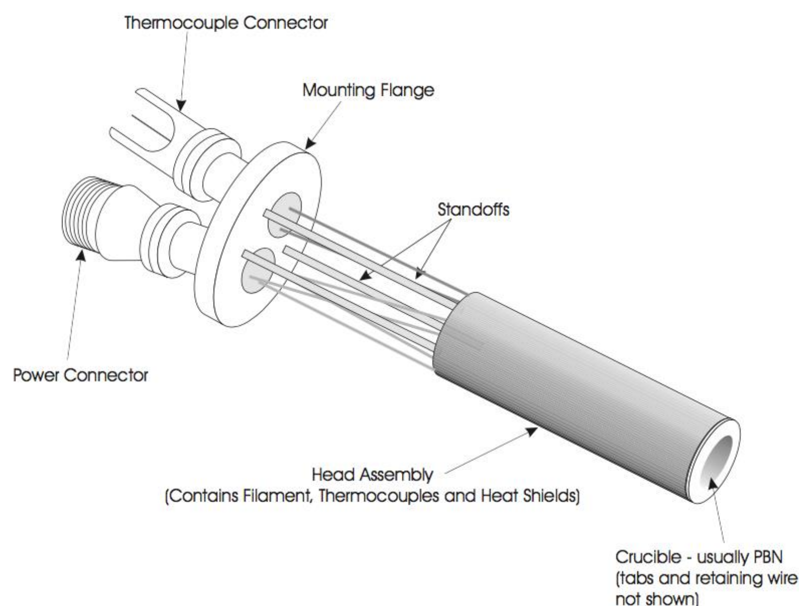

Figure 3.3. Schematic diagram of a standard thermal effusion cell [7].

The substrate heater is mounted on a substrate manipulator allowing for position adjustments about two axes. One of the axes is for positioning the wafer for growth, transfer or beam flux measurement, and the other one for rotating the sample along its own axis in order to achieve more uniform growth across the wafer. The substrate heater has a wound wire heating filament inside that can heat the substrate to a temperature higher than 1000°C [7] and is placed at the focal point of the effusion cells.

A pyrometer placed behind an optical viewport outside the chamber, together with a thermocouple placed right behind the substrate, is used to monitor the temperature

of the wafer during growth. Use of phosphorus in the MBE requires a special phosphorus recovery system in order to eliminate environmental pollution and safety hazards that could arise if phosphorus containing residue gas was directly vented. Ion vacuum gauges are used to monitor vacuum levels in the chambers as well as the beam equivalent pressure. Residual Gas Analysis (RGA) is used to monitor the background gas composition by analysing the mass-to-charge ratios of ionised gas molecules.

A Reflective High Energy Electron Diffraction (RHEED) system is used to monitor the growth in-situ. Electrons from a 10-20 keV electron gun are fired onto the wafer at a grazing angle. The diffracted electrons are collected at a fluorescent screen and form patterns according to the crystal structure of the grown sample. These diffraction patterns have been studied in detail and can give qualitative information about surface roughness. Intensity oscillation of the RHEED pattern at different stages of monolayer growth is presented in Figure 3.4. The period of the oscillation of the RHEED pattern gives the time it takes to grow one monolayer. The decay in intensity occurs due to imperfect growth mechanism when new islands are formed on top of currently grown layer before it is completed.

In order to precisely control the growth process and ensure repeatable results, several calibration steps need to be carried out before starting the growth. First the temperature of the substrate is calibrated using the pyrometer and thermocouple. Because the readings vary every time the state of the machine is altered i.e. by opening the chamber, baking etc., the same readings before and after in reality

correspond to different temperatures. In order to establish by how much the readings change, a growth for which precise growth conditions have been developed is performed. The results are then compared with previous ones and the substrate temperature adjusted until the optimal conditions are met. The second parameter to calibrate is the beam flux. Each of the sources used in the specific growth is calibrated separately. Using the ion gauge readings of vacuum levels with the beam on and off, the flux is calculated as the difference between the two. The temperature of the source is then adjusted to reach the flux levels required for specific growth recipe. The growth rate is the last calibrated parameter. It can either be extracted from the RHEED oscillation measurement or calculated from the beam flux using sticking coefficients of the different elements.

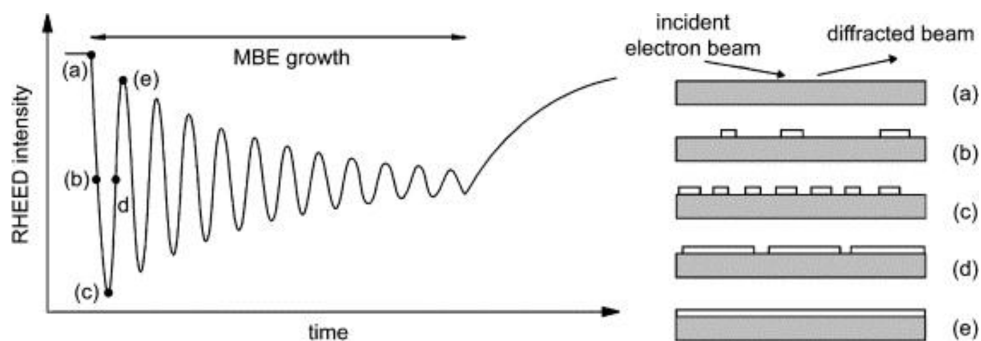

Figure 3.4. RHEED intensity oscillation at different growth stages [6].

3.1.2 MBE Growth Mechanisms

In a solid-source MBE system like Veeco Gen930, high purity crucibles in cells are heated up to evaporate the source materials inside them. The beamed atoms

bond with each other on the surface of the substrate following its crystal template. Figure 3.5 illustrates the epitaxial growth in an MBE system.

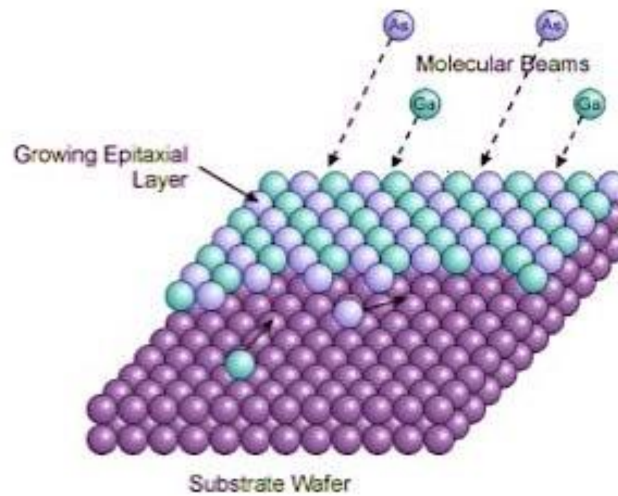

Figure 3.5. Simplified MBE growth mechanism [8].

During the MBE growth of III-V semiconductors, fluxes of group-III and group-V materials arrive at the surface of the heated substrate. At typical growth temperatures, group-III elements have a unity sticking coefficient and hence adhere to the substrate, while group-V elements do not stick to the surface if there are no group-III atoms already on it [2]. Therefore the growth rate of III-V semiconductor films is governed by the group-III flux as excess group-V atoms are desorbed from the surface. Figure 3.6 shows different behaviours of atoms arriving at the substrate, including adsorption and desorption.

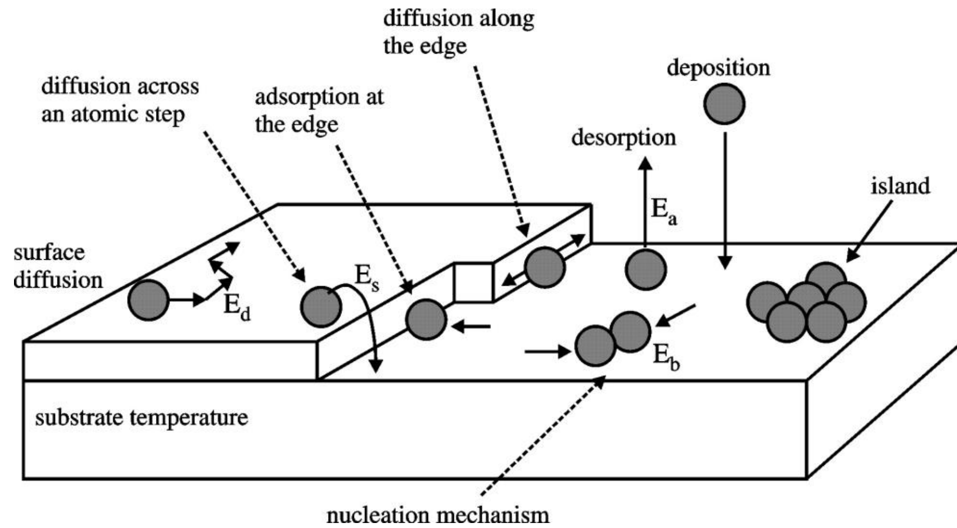

Figure 3.6. Atoms behaviour during surface deposition [9].

There are three different growth modes that can be adopted during epitaxial growth, depending on the lattice strain and free energy of the interfaces. The Frank-van der Merwe mode is a 2D layer-by-layer growth mode, Volmer-Weber is an island mode (3D) and Stranski-Krastanov combines the two (layers plus islands mode). The 2D growth occurs when the energy change $\Delta \mathrm{E} = E_{film} + E_{int} - E_{sub}$ is lower or equal 0, where E_{film}, E_{int} and E_{sub} are respectively the free energies of the film surface, the interface and the substrate. The group-III atoms then prefer incorporation at the edge of existing island to incorporation on top of them resulting in a layer-by-layer growth. When lattice-mismatched materials are grown, the epilayer is forced to follow the crystal template of the substrate by fitting to its lattice constant. This leads to build up of strain, which can cause increase of E_{film} with increasing thickness of the epitaxial film. The energy change ΔE becomes positive and the growth switches to the 3D island mode, typically used for growth of self-assembled quantum dots. Figure 3.7 below illustrates the three main growth modes.

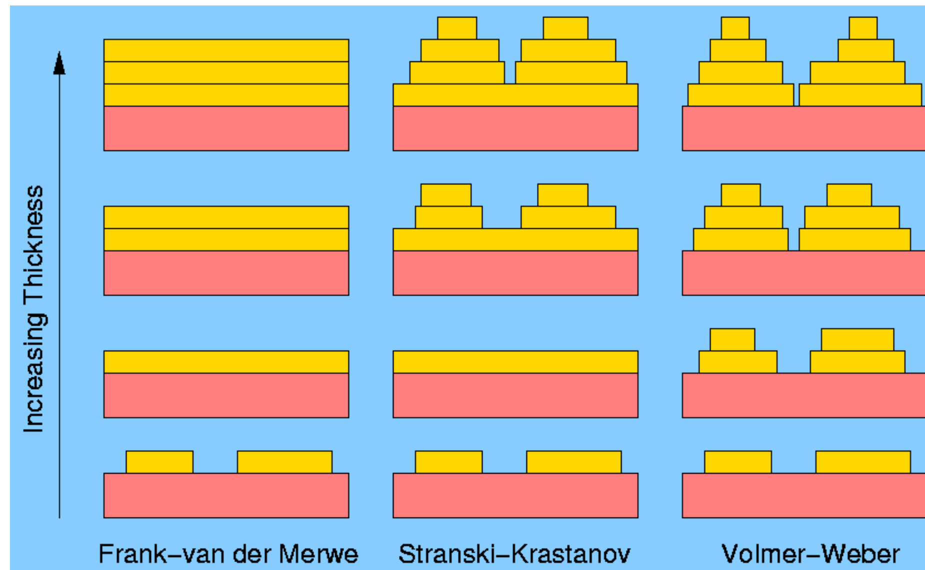

Figure 3.7. Illustration of the three main growth modes: Frank-van der Merwe, Stranski-Krastanov and Volmer-Weber [10].

3.1.3 Atomic Force Microscopy

The atomic force microscope (AFM) is a type of scanning probe microscope (SPM). It is used to investigate nano-scale topography of various surfaces measuring properties like height, friction or magnetism with a probe. The AFM works by measuring the force between a pyramid-shaped tip, located at the end of a cantilever, and the sample. It is a good alternative to scanning electron microscope (SEM), which can only be used to image conductive surfaces. The lateral resolution of the AFM is relatively low (about 30nm), but the vertical resolution can be as high as 0.1nm due to the convolution [10]. To acquire an image, the AFM measures deflections off the cantilever using a laser and a photo-detector. The AFM is the main technique used to analyse surface morphology of the epitaxial TPV cells for this thesis. Figure 3.8 shows an AFM image of the surface of an $In_{0.85}Ga_{0.15}As$ TPV cell grown on GaAs substrate

with an InAlAs buffer (a) and an AFM image of InAs/GaAs quantum dots.

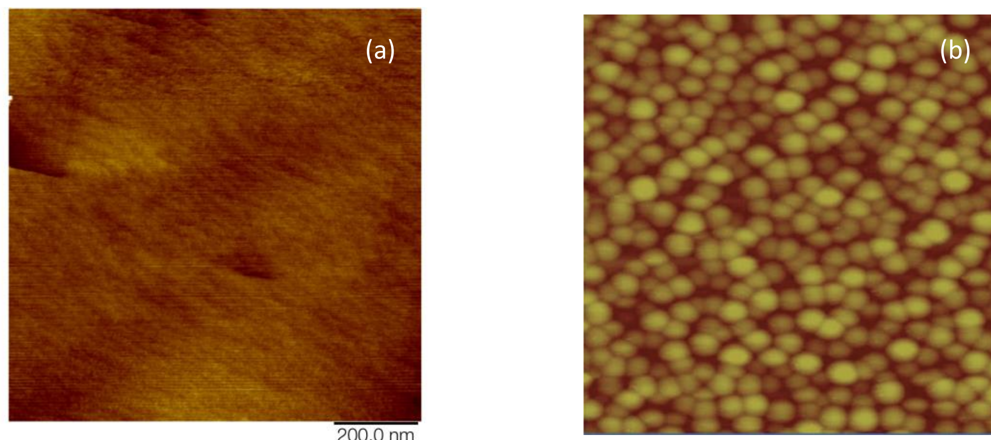

Figure 3.8. AFM image of an (a) $In_{0.85}Ga_{0.15}As$ TPV cell grown on GaAs substrate with an InAlAs step-graded buffer grown by MBE and (b) InAs/GaAs quantum dots [12], both 1μm × 1μm.

3.1.4 Scanning Electron Microscopy

Scanning electron microscope (SEM) is a type of electron microscope that uses focused electron beam to produce images. It detects electrons interactions with the atoms in the sample and can be used to obtain information about the topography and composition of the sample. The resolution of an SEM can be as good as sub-nanometre since it depends on the de Broglie wavelength of the electrons in the electron beam described as $\lambda=h/p$, where h is the Planck constant and p is the momentum of the electrons. For example, if electrons with 100 eV kinetic energy are used, according to this equation their de Broglie wavelength is only 0.12 nm. Therefore this imaging technique is specifically useful for observing nano-scale structures such as for example nanowires.

Before the measurement the sample needs to be prepared to prevent

accumulation of charge. It occurs when the sample is nonconductive therefore electrically grounding the sample is crucial for obtaining high-quality images. This is usually achieved by using silver paste to attach the conductive samples to the specimen holder or by creating discharge paths for nonconductive ones i.e. by coating the sample with an ultrathin layer of gold.

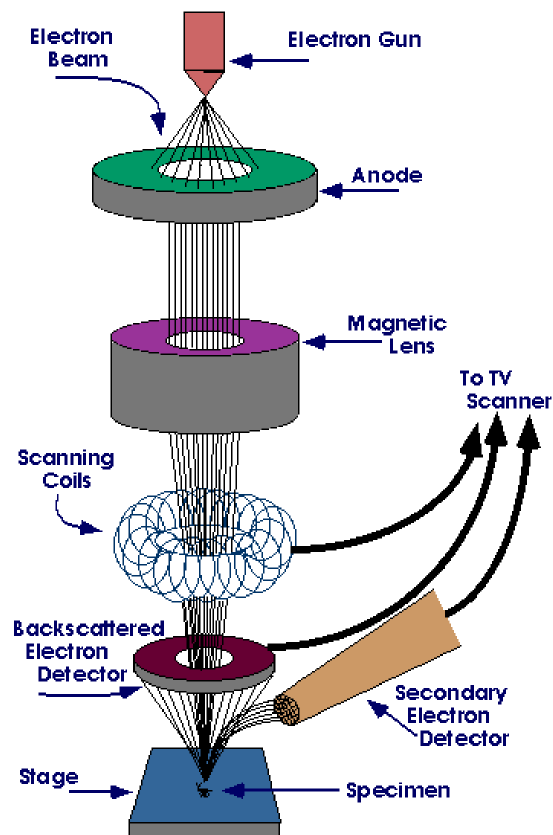

Figure 3.9. Schematic diagram of a scanning electron microscope [13].

Figure 3.9 shows a schematic drawing of an SEM system. An electron gun emitting a beam of electrons with energies ranging between 1 and 50 keV [14] is usually used for the measurements. Applying a voltage between anode and cathode placed below the thermionic emission electron gun accelerates the electrons to desired

energies, while in field-emission guns high negative fields are used to expel high-energy electrons. The electron beam is then focused using electromagnetic lenses to a spot of about 0.4-5 nm in diameter. When it hits the surface of the sample, electrons interact with the atoms of the sample and generate different kinds of signals. They include primary and secondary electrons, back-scattered electrons, transmitted electrons, characteristic x-rays, sample current and cathodoluminescence. Secondary electron detection is most commonly used in characterising the morphology of semiconductor samples. Figure 3.10 shows sample SEM images of InGaP nanowires.

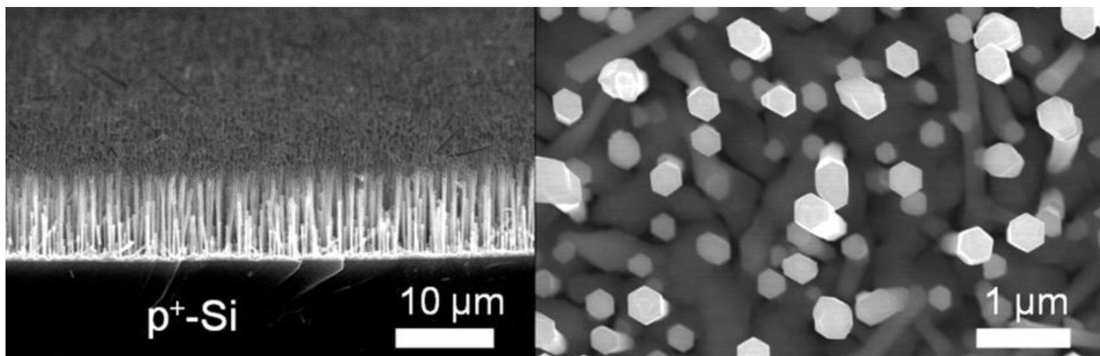

Figure 3.10. Low-magnification side-view and top-view and high-magnification top-view SEM images of vertically orientated GaAsP p–n homojunction nanowires grown onto a p^+-Si (111) substrate[15].

3.1.5 Transmission Electron Microscopy

Similarly to an SEM, a transmission electron microscope (TEM) uses an electron beam to obtain information about the measured sample. It is a high resolution imaging technique, which is the best one to be used to investigate crystal quality of MBE grown

materials. While SEM usually focuses on detecting secondary electrons, a TEM uses the transmitted electrons to obtain images at atomic scale. The beam in a TEM is highly converged allowing observation of single atoms in the sample and is usually used to observe crystal defects and dislocations. Samples used for measurements need to be ultra-thin in order to allow transmission of electrons through the specimen. There are two main modes of TEM imaging. The most frequently used "bright field imaging mode" relies on measuring the levels of transmitted electrons, while the "dark field imaging mode" detects scattered electrons. In both modes the variation in contrast caused by some electrons being transmitted and some being scattered is used to map information about the sample. Images obtained with these two modes are opposite in brightness and contrast. Figure 3.11 shows TEM images of an InGaAs TPV cell grown on GaAs substrate using an InAlAs buffer. The structure of the cell has been shown in Figure 1.1 in section 1.3.1 in Chapter 1 and it is the structure of the cell analysed in Chapter 5 of this thesis.

From the images in Figure 3.11 the crystal quality of specific layers of the TPV structure can be observed. The lines visible in (a) and (c) are threading dislocations (example marked with red circle) arising from lattice mismatch between the GaAs substrate and subsequently grown epitaxial layers. The top part of the structure shown in the upper half of (a) and in (b) shows good crystal quality free from threading dislocations which is highly important for obtaining good quality devices.

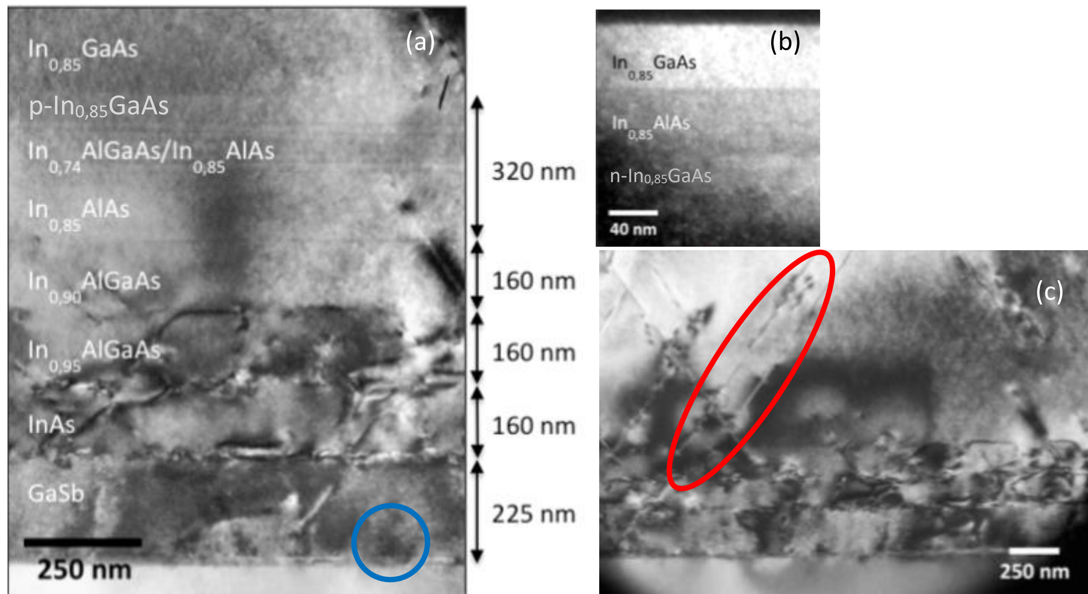

Figure 3.11. TEM images of (a) cross section of an InGaAs TPV cell, (b) the top layers and (c) cross section of the buffer layers (indicated with blue circle in a) with visible threading dislocations. The red circle marks one of the threading dislocations for clarity.

3.1.6 X-ray Diffraction

The X-ray diffraction (XRD) technique is used to precisely determine the composition of the materials within a structure. The wavelength of X-rays is comparable with the interatomic distances in crystals. When the X-ray interacts with the periodic atom array in the crystal, it can be diffracted. The resulting diffraction pattern is rich in crystallographic information. Thus, X-ray diffraction is widely used in semiconductor field to determine the parameters of epitaxial layers, such as the composition, lattice mismatch, defects, mis-orientation, layer thickness, tilt, relaxation, strain, interface quality, and area homogeneity.

The most important parts of the XRD machine are X-ray tube, sample stage and

the X-ray detector, as can be seen in Fig. 3.12. During the measurement, as illustrated in Fig. 3.12b, the X-ray irradiates parallel planes of atoms and can be scattered by the atoms inside. At a certain incident angle θ, the light-path difference of scattered waves can satisfy the Bragg's Law, $n\lambda = 2d \sin\theta$, where n is positive integer, λ is the wavelength of the X-ray, d is the interplanar spacing, and θ is the incident angle. In this case, the interference of the scattered light can lead to enhanced peak intensity, also called diffraction. Since the X-ray wavelength λ is fixed, a family of planes, with an interplanar spacing of d, produces a diffraction peak only at a specific angle θ. Therefore, the space between diffracting planes of atoms determines peak positions. Because the interplanar spacing of atomic planes is governed by the material composition, XRD can be used to check the composition and lattice mismatch between the epitaxial layers.

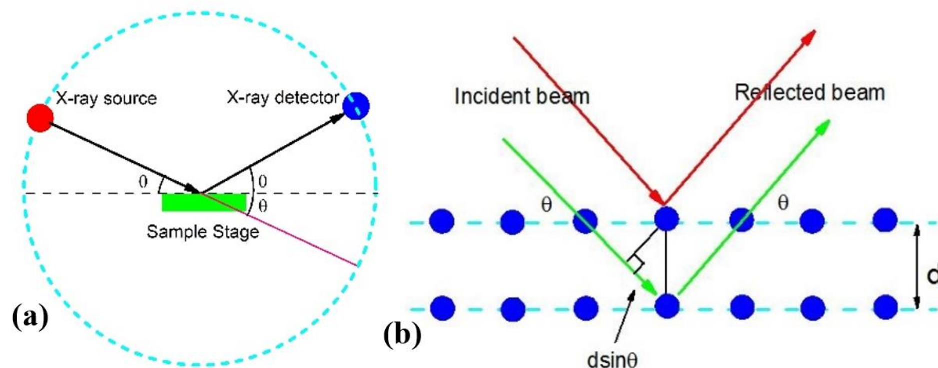

Figure 3.12. Illustration of an XRD system (a) and the measurement mechanism (b).

3.2. Device Processing

In order to create working devices from epitaxially grown wafers, some processing is required. It usually consists of five major steps: cleaning,

photolithography, wet etching, metallisation and thermal annealing. Details of these processes are described in this section. An outline of a typical process flow for fabrication of TPV cells is summarised in Figure 3.13.

Figure 3.13. Flow chart of standard device fabrication process for TPV test cells.

3.2.1 Cleaning

Contaminants present on the wafer surface during fabrication process have detrimental effects on the quality of produced devices. Therefore the key to high

quality reproducible devices is thorough initial cleaning and maintaining proper level of cleanliness throughout all the processing steps. Solvents like acetone and isopropyl alcohol (IPA) are good at removing organic materials and oil, additional methanol cleaning step can be added for better results or butyl acetate for especially stubborn contaminations (i.e. finger prints). Cleaved samples are placed in butyl acetate in an ultra-sonic bath for one minute, then soaked in acetone, methanol (optionally) and IPA for 5 minutes each, ultra-sonic bath can also be used for each of these solvents. IPA rinse is often applied between the processing steps as well, for example after photoresist removal, in order to remove any possible contaminants transferred i.e. from equipment or tools used. Natural oxides on the semiconductor surface also need to be removed in order to ensure good metal adhesion. The samples are soaked in ammonia water solution or HCl water solution and then rinsed with DI water. This step is usually performed during initial cleaning as well as before metal evaporation steps. It is also crucial to remove all contaminants from the tools and glassware used during processing steps so that they are not transferred onto the wafer and do not compromise the quality of final devices.

3.2.2 Photolithography

Due to its simplicity, photolithography is the most popular technique used to define fine features during nano-scale processing, i.e. etch patterns or metallisation grids. Light-sensitive photoresist is deposited onto the sample using a spin-coater in order to achieve uniform thickness. This step is usually followed by a so-called soft

bake, which improves photoresist adhesion by removing solvents and water. The recommended temperature and duration of bake is specific for each photoresist. Illuminating photoresist with UV light through an optical mask allows for selection of areas of semiconductor to be exposed for further processing. There are two types of photoresist, each reacting with the UV light in opposite way. When positive photoresist is developed, parts that have been exposed to UV are removed leaving features on the wafer identical to those on the mask, while negative photoresist leaves and opposite pattern. For mesa photolithography, positive photoresist Shipley S1818 is spun-on at 4000 rpm (repeats per minute) for 30 seconds, followed by soft bake, UV exposure and development. An additional layer of Lift-Off Resist LOR10B is added before S1818 deposition for metallisation patterns photolithography in order to create undercut, which allows for easier lift-off process after the metals are evaporated onto the surface of the sample. It is spun-on at 4000rpm for 30s, same as S1818. Each of these photoresist require a separate soft bake, 10 minutes at 190°C for LOR10B and 1 minute at 105°C for S1818, for optimal adhesion. The coated samples are exposed to UV for 4-5s, depending on the thickness of the photoresist, and then developed in MF319 (dilute ammonium hydroxide) for 40-45s followed by a DI water rinse. After deposition of the top contacts acetone is used to remove the S1818 and achieve lift-off. Same process is used to remove remaining photoresist after etching. LOR10B is removed by soaking the sample in MF319 for a few hours. A standard lift-off process is illustrated in Figure 3.14.

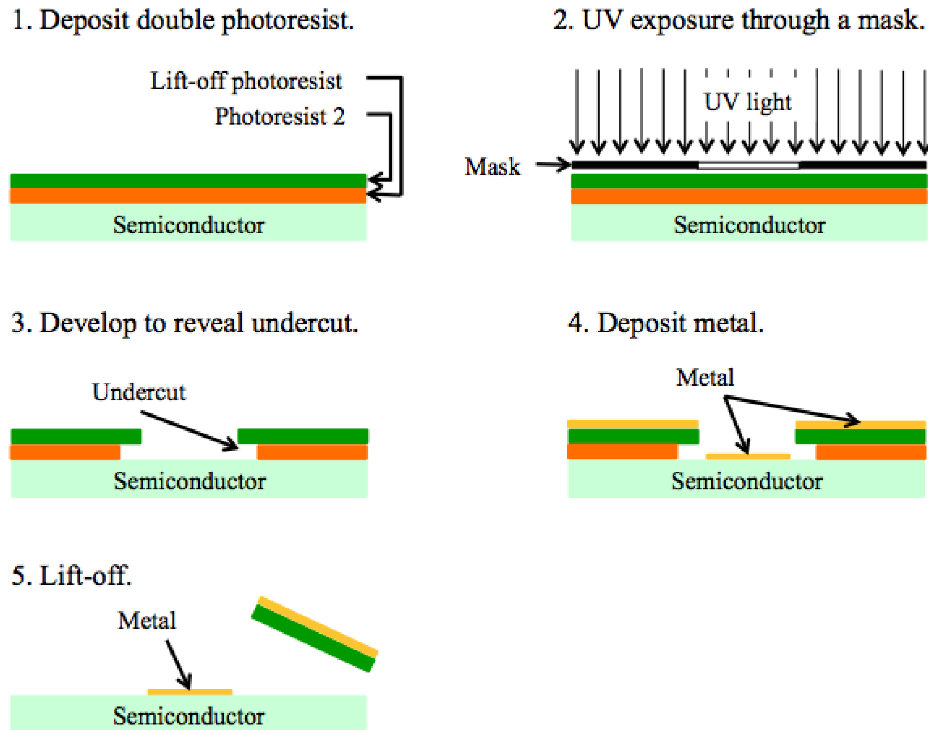

Figure 3.14. Main steps of a standard lift-off procedure.

3.2.3 Wet Etching

In order to ensure good current and optical confinement, devices on the sample need to be isolated. To achieve this a mesa is created with wet etching. A photolithography step is required in order to create a suitable pattern of the mesa and protect the active area of the devices from being etched away, as described in section 3.2.2. Wet etch is also used to access the bottom contacting layer of the devices when top-top approach is used for contacts formation. Most semiconductor etchants work in two steps. First they oxidise the surface and then remove the formed oxide layer together with some atoms of the semiconductor. The etch is carried out by immersing the samples in an appropriate solution, for semiconductors like InAs/GaAs/AlGaAs H_3PO_4:H_2O_2:H_2O (1:1:3) is usually used. The solution can be made more dilute by

adding more water in order to achieve more precise control over the etch rate. To confirm that the correct depth has been reached, Dektak measurements are performed.

3.2.4 Metallisation

To create working devices, it is necessary to create ohmic contacts to the highly doped p and n layers of the TPV samples. Ohmic contacts are thin Schottky barriers that allow conduction across the metal-semiconductor junction via tunnelling. There are several methods used for deposition of metals for creation of contacts, in this project thermal and e-beam evaporators are used. In a thermal evaporator metals are places in molybdenum boats, which are resistively heated in order to melt and then evaporate the metals. E-beam evaporators are mostly used for metals with high melting points and a high-energy electron beam is used to evaporate them from a crucible. Thickness monitors are used to ensure correct thicknesses are being deposited. Typical metals combinations for GaAs based devices are Zn/Au (10nm/200nm) for the p-type contacts and Ni/AuGe/Ni/Au (10nm/100nm/30nm/200nm) for the n-type. These metals however are not suitable for contacting low bandgap semiconductors like In-rich GaInAs, InAs, InAsSb etc. For these materials Ti/Au (20nm/200nm) is one of the suitable options for both p and n-type contacts. Ti ensures good adhesion to the highly doped semiconductor epilayer and Au has good conductance characteristics. They are deposited using an e-beam evaporator system.

For two-terminal devices such as TPVs or solar cells, there are two general methods of designing the contacts. One of them is to deposit the bottom contact on the back side of the substrate surface and the top contact on top of the sample using a shadow mask or a photolithography mask. This method is referred to in this thesis as top-bottom. However, using the bottom contact on the back of the substrates requires the current to travel through all the layers below the active region, i.e. the buffer layers and the substrate. If the lattice mismatch between the active region and the substrate is large and many dislocations are formed within the buffer layers, carriers passing through those layers can easily recombine and the resulting output current will be severely reduced. Therefore, a different contacting method should be used where the contacts are directly applied to the highly doped contacting layers within the sample. This approach is referred to as top-top in this thesis. The top contact is deposited in the same way as in the top-bottom approach, usually using photolithography for masking. In order to access the bottom contacting layer, the top layers in the contact area need to be etched away. Usually a photolithography mask is used to define the etch area as well as the areas for both the n and p type contacts.

3.2.5 Thermal Annealing

Thermal annealing simply means heating up the sample to a high temperature for a certain period of time, usually in forming gases atmosphere or just under nitrogen flow. It is often used after metallisation to aid the formation of ohmic contacts by inducing diffusion of the deposited metals into the sample. Temperatures in the range

of 350-400°C and durations of 5-30 seconds are typically used, details depending on specific metals combinations used. The temperature in the RTA (Rapid Thermal Annealer) is quickly ramped up, held at the programmed level for a specified period of time and then cooled down in nitrogen atmosphere. An RTA system can also be used to treat as-grown samples to improve the quality of the crystal by inducing movement of particles at high temperatures (600-800°C) often for a long period of time (few minutes to few hours). An annealing study, i.e. high temperature RTA treatment for a range of durations and temperatures aimed at establishing optimal annealing conditions, is often conducted for MBE grown samples to remove crystal defects and improve the performances of fabricated devices.

3.3. Characterisation

3.3.1 Photoluminescence

Photoluminescence (PL) is an optical characterisation technique widely used for various semiconductor materials (epitaxially grown III-V and II-IV compounds, Si, Ge, GeSn etc.) and nanostructures (quantum dots, quantum wells, nanowires). It allows detailed analysis of the band structures of abovementioned structures. It is also very useful in studying defects and impurities within the samples. Being a non-destructive technique it is often the preferred tool for assessing quality of the material.

The setup for mid-IR PL measurements used for characterisation of TPV materials consists of an excitation light source (532 nm laser), sample holder stage with a cryostat (He compressor cooling system), monochromator, lenses,

photoreceiver (liquid nitrogen cooled InSb detector), pre-amplifier, lock-in amplifier and signal analyser (computer software, BenWin). The setup is illustrated in Figure 3.15.

During the measurement, the sample is excited by a laser with photon energy higher than the bandgap of the measured material. The incoming photons help electrons to jump to conduction band generating electron-hole pairs. Then the electrons relax back to valence band emitting radiation that can be detected by an optical receiver. Typically measurements are taken at room temperature, where band-to-band recombinations dominate the emission, and at low temperatures. Taking measurements at low temperatures (up to 10 K) is advantageous because phonon-induced peak broadening is reduced, thermally activated non-radiative recombinations are supressed and carriers' interactions with excited states are limited. Measuring the energy of emitted photons, energy levels of impurities can be obtained.

PL measurements can be used to check the crystal quality of the material. Stronger PL signal means that radiative recombination dominates and, since defects normally contribute to non-radiative recombinations, that the crystal quality is good. Power-dependent measurements where the laser power is varied can also provide useful information about the material. Filling of the excited states help to extrapolate the band structure and observe effects like quantum-confinement-induced energy levels splitting. Temperature-dependent measurements can help to deduce carrier confinement barriers. Increasing the temperature of the sample will cause some electrons to thermally escape and their emission can be measured. It will also result

in redshift of the emission peak, which is an evidence of temperature-induced bandgap change. This relation is explained by a semi-empirical relationship known as the Varshni equation [16].

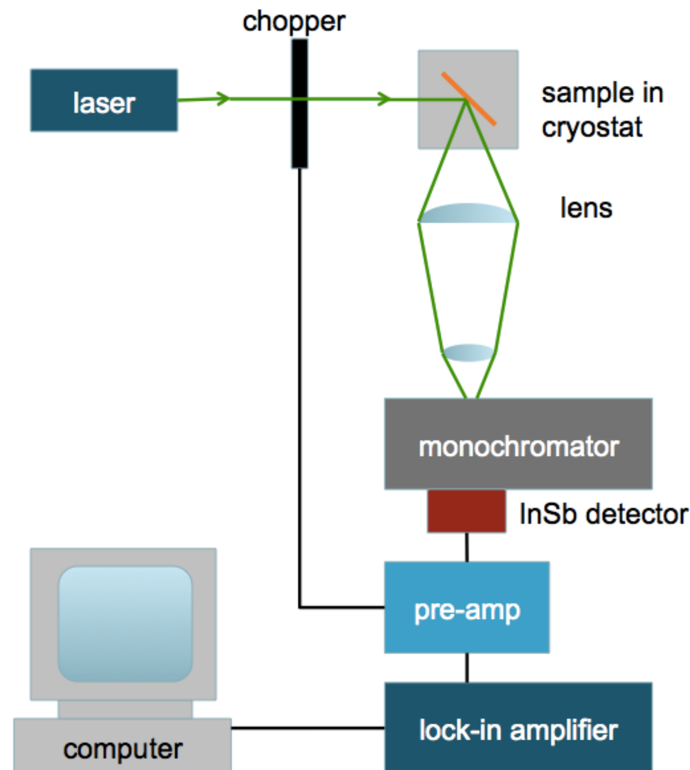

Figure 3.15. Simplified PL equipment setup.

3.3.2 Electrical Characterisation

After the devices are fabricated, usually the dark current is measured first since it can give a good estimate of how good the device is. The dark JV was measured at UCL using solar simulator setup without turning on the xenon lamp. During the measurement a small forward bias is applied to the device using a Keithley source-measure unit. The current flowing through the device is then measured and the J-V characteristics of the device are plotted using system manufacturer-provided software.

To ensure accurate measurements a temperature controlled copper stage is used to maintain constant temperature of the cells.

To further characterise the performance of the TPV devices, illuminated J-V measurements are needed. The general setup is similar to the solar simulator setup described above, the main difference being the illumination source. For measuring solar cells J-Vs a xenon lamp with an AM1.5 Global filter and power density of $1kW/m^2$ is usually used, while for mid-IR radiation needed for TPVs a blackbody source is used. The setup at the Army Research Lab (ARL), where the devices fabricated for this thesis were measured, uses a blackbody source calibrated to 1000°C. Different aperture sizes are used to adjust the amount of power delivered to the cells.

3.4. References

1. R.F.C. Farrow, Molecular Beam Epitaxy – Applications to Key Materials, *William Andrew Publishing/Noyes*, 1995.
2. A.Y. Cho and J.R. Arthur, Molecular beam epitaxy, *Prog. Solid-State Chem.,* vol. 10, 1975.
3. A.Y. Cho, How molecular beam epitaxy (MBE) began and its projection into the future, *J. Cryst. Growth,* vol. 201-202, 1999.
4. J.R. Arthur, "Molecular beam epitaxy", *Surf. Sci.,* vol. 500, no. 1-3, 2002.
5. W.P. McCray, MBE deserves a place in history books, *Nature Nanotechnology* 2, 259-261, 2007.
6. S. Franchi, G. Trevisi, L. Seravalli, and P. Frigieri, Quantum dot nanostructures and molecular beam epitaxy, *Prog, Cryst. Growth Charact. Mater.*, vol. 47, no. 2-3, 2003.
7. Veeco GEN II GEN930 Operation Manual, Document 580009.
8. Molecular Beam Epitaxy, Details of the MBE facility at UCL, accessed on 22nd October 2015, https://www.ee.ucl.ac.uk/about/MBE.
9. Molecular beam epitaxy (MBE), Technische Universitat Kaiserslautern, accessed on 22nd October 2015, https://www.physik.uni-kl.de/hillebrands/research/methods/molecular-beam-epitaxy/.
10. Epitaxial growth, Universidad Autonoma de Madrid, accessed on 2nd November 2015, http://www.uam.es/personal_pdi/ciencias/jdemigue/research/growth.html.

11. W. Mai, Fundamental Theory of Atomic Force Microscopy, Georgia Institute of Technology, accessed on 2nd November 2015, http://www.nanoscience.gatech.edu/zlwang/research/afm.html.
12. T. Wang, A. Lee, F. Tutu, A. Seeds, H. Liu, K. Groom, and R. Hogg, The effect of growth temperature of GaAs nucleation layer on InAs/GaAs quantum dots monolithically grown on Ge Substrates. *Appl. Phys. Lett.* 100, 2012.
13. Scanning Electron Microscope, Purdue University, accessed on 2nd November 2015, https://www.purdue.edu/ehps/rem/rs/sem.htm.
14. L. Reimer, Scanning Electron Microscopy: Physics of Image Formation and Microanalysis, *Springer*, 2013.
15. J. Wu *et.al.*, Wafer-Scale Fabrication of Self-Catalyzed 1.7 eV GaAsP Core-Shell Nanowire Photocathode on Silicon Substrates, *Nano Lett.* 14(4), 2014.
16. 3.2.1. E. Grilli, M. Guzzi, R. Zamboni, and L. Pavesi, High-precision determination of the temperature dependence of the fundamental energy gap in gallium arsenide. *Phys. Rev. B. Condens. Matter,* vol. 45, no 4, 1992.

Chapter 4:

Theoretical Performances of GaInAs Thermophotovoltaic Cells

The main challenge in modelling III-V semiconductors with variable compositions is lack of accurate data on their optical and electronic parameters. The first part of this chapter describes how to circumvent this issue using a thermodynamic approach based solely on the absorption spectrum of the material for the radiative recombination rates calculations. All the steps of the simulations are explained in detail and relevant methods are described. The model has been developed in MATLAB®2014b and the simulations have been run with rectangular integration on the wavelength from 200 to 10000 nm with a 1 nm step.

The impacts of various cell parameters and illumination conditions on the efficiencies of the GaInAs TPVs have been investigated in detail in this chapter. The effects of different architectures and thicknesses of the cells as well as crystal quality and cell temperature have been described in detail. At the end of the chapter we also discuss how the results for various source temperatures and incident power densities can be used to determine the optimal operating conditions for real life devices.

4.1 The Basis of the Model

4.1.1 Architecture of the Cells

Cells with two different architectures have been investigated in this project. The first one implements a perfect light trapping system consisting of a textured front surface and a perfectly reflecting back mirror. The surface texturing randomises the photon flux in order to obtain a Lambertian distribution of the scattered light. The mirror at the back of the cell allows for substantial lengthening of the optical path of the photons in the cell and eliminates the dark-current radiative reemissions from the bottom side of the cell. This architecture is used to evaluate the maximum possible theoretical efficiencies of the cells. The second one is much simpler, its front surface is flat and there is no back mirror. This means that there is no light trapping in the cell and that radiative reemissions occur from the back surface. This architecture gives a better approximation for real-life cells that are relatively easy to fabricate and allows for estimation of realistic efficiencies. In both cases it has been assumed that there is no reflection from the top surface of the cells and that there is no shadowing from the

front contacts.

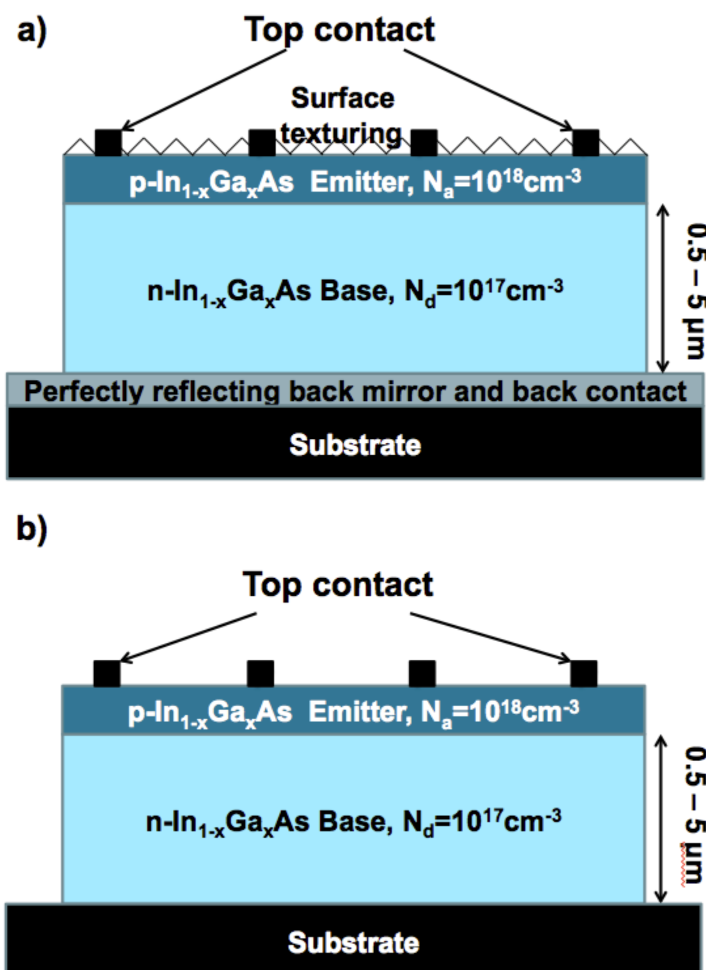

Figure 4.1. The details of the cell architectures with (a) and without (b) light trapping mechanism investigated in this chapter.

Figure 4.1 shows the details of the two architectures described above. Both cell have p^+/n structures and variable thickness between 0.5 and 5 µm. The emitter is p-type with doping of $N_a=10^{18}cm^{-3}$ and fixed thickness of 0.1 µm. The n-type base has a variable thickness and is slightly less doped, $N_d=10^{17}cm^{-3}$. Both emitter and the base of the cell are made of same composition of $Ga_xIn_{1-x}As$ and the gallium content varies from x=0 to 0.5. This range of compositions have been chosen in order to obtain a

wide spectrum of bandgaps, between 0.36 and 0.78 eV, relative to TPV operation.

4.1.2 Absorptivity Models

The absorptivity of the cell depends on its structure. In the model presented in this chapter we use two architectures, as described in the previous section. Figure 4.2 shows the simplified picture of how the light travels through the cell in these two cases and hence how it affect the absorption within the cells.

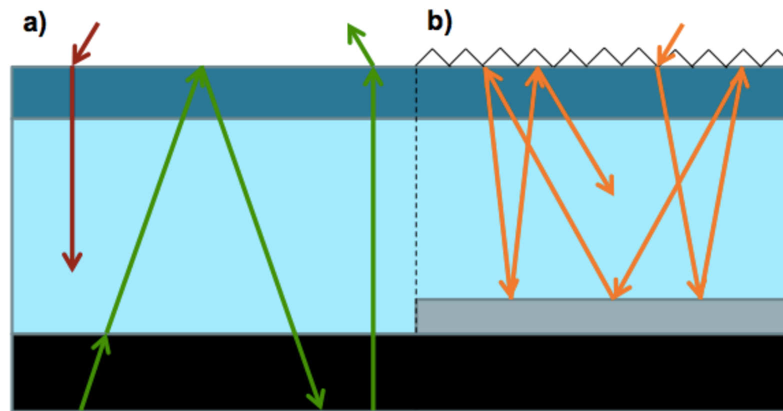

Figure 4.2. The details of the absorptivity models used in the simulations: (a) flat top surface with front surface (red arrows) and back surface (green arrows) absorption and (b) ideally textured surface with a back mirror creating light trapping (orange arrows).

In the architecture with light trapping there is no absorption through the back surface therefore the absorptivity from the back of the cell $a_{back}=0$ and hence the total absorptivity is equal to the absorptivity from the front of the cell $a(\lambda)=a_{front}(\lambda)$. This model of absorption is depicted in Figure 4.2(b) by the orange arrows. With this architecture we consider the light trapping to be ideal [1], therefore the absorptivity of this cell can be expressed as:

$$a(\lambda) = \frac{4n_r^2 \alpha_{GaInAs}(\lambda)}{1 + 4n_r^2 \alpha_{GaInAs}(\lambda)} \quad \text{4-1}$$

where $\alpha_{GaInAs}(\lambda)$ is the wavelength-dependent absorptivity coefficient of $Ga_xIn_{1-x}As$ (eq. 2-3), n_r is the refractive index and L is the cell thickness.

In the cell without light trapping the total absorptivity is the sum of both front and back absorptivities so that $a(\lambda)=a_{front}(\lambda)+ a_{back}(\lambda)$. The light incident on a planar surface is refracted at the front surface of the cell with an angle close to perpendicular due to large difference between the refractive indices of air and GaInAs, as shown with red arrows in Figure 4.2(a). The front surface absorptivity $a_{front}(\lambda)$ can then be expressed as:

$$a_{front}(\lambda) = 1 - \exp(-\alpha_{GaInAs}(\lambda) \cdot L). \quad \text{4-2}$$

Because there is no back mirror in this architecture, the cell is also absorbing through its back surface. The radiative recombination rate calculations have to therefore include this back absorptivity. $a_{back}(\lambda)$ has to take into account the increase in absorption due to total internal reflection at the front side of the cell of photons with high incident angles (see green arrows in Figure 4.2(a)) like shown by Miller et al. [2]:

$$a_{back}(\lambda) = 2n_r^2 \begin{pmatrix} \int_0^{\theta_{esc}} \left(1 - exp\left(-\alpha_{GaInAs}(\lambda) \cdot \frac{L}{cos\theta}\right)\right) cos\theta sin\theta d\theta \\ + \int_{\theta_{esc}}^{\frac{\pi}{2}} \left(1 - exp\left(-2\alpha_{GaInAs}(\lambda) \cdot \frac{L}{cos\theta}\right)\right) cos\theta sin\theta d\theta \end{pmatrix} \quad \text{4-3}$$

where θ is the polar angle at which light is reflected and $\theta_{esc}=arcsin(1/n_r)$ is the critical escape angle.

4.1.3 Blackbody Theory and Flow Equilibrium

In order to obtain the J(V) characteristics and hence maximum efficiencies of the

modelled cells it is necessary to calculate the radiative recombination rates under ideal conditions first. The conditions are considered ideal if there are no other sources of recombination in the cells. In this model the blackbody theory and the flow equilibrium in the cell, in the dark and under illumination, have been used to obtain the radiative recombination rates. Hence the radiative limit is the theoretical maximum efficiency achievable by the investigated devices. This limit arises from the flow equilibrium within the diode. Not all of the absorbed photons are contributing to generation of photocurrent, some of the excited carriers recombine emitting back the photons which escape through the surfaces of the cell. These radiative reemissions are the fundamental loss mechanism intrinsic to the physics of the semiconductors and are unavoidable. More detail on these processes can be found in section 2.2.2 of this thesis.

Würfel's blackbody theory extended to semiconductors, under the Bose-Einstein approximation ($E >> k_B T$), gives the emission rate of each cell under ideal conditions and in the dark [3]:

$$R_{r,rad}(V) = e^{\frac{qV}{k_B T}} \int_0^{+\infty} \frac{2\pi c a(\lambda)}{\lambda^4} e^{-\frac{hc}{\lambda k_B T}} d\lambda = R_{r,rad,sc} e^{\frac{qV}{k_B T}} \tag{4-4}$$

where q is the elementary charge, V the voltage of the cell, k_B the Boltzmann constant, T temperature (set at 300 K), c the speed of light, $a(\lambda)$ is the wavelength-dependent absorptivity of the cell, λ is the wavelength of photons and h the Planck constant.

The voltage-independent part of the equation (under the integral) describes the short-circuit recombination rate and hence can be renamed $R_{r,rad,sc}$ for simplification of the expression. Its value is equal to the radiative recombination rate at the thermal

equilibrium in the dark $R_{r,rad,sc}=R_{r,rad}(V=0)$ and describes how many photons are reemitted from the cell in the dark in order to balance the flow received from the surrounding blackbody environment at 300 K.

Next we consider the flow equilibrium in the cell under illumination and also take into account the non-radiative recombinations. In this case the current density can be described using the Shockley diode equation under illumination [4]:

$$J(V) = J_{ph} + qR_{r,rad,sc}\left(1 - e^{\frac{qV}{k_B T}}\right) + q\sum_{m} R_{r,m}\left(1 - e^{\frac{qV}{n_m k_B T}}\right) \qquad 4\text{-}5$$

where J_{ph} is the photo-generated current, $R_{r,m}$ the short-circuit non-radiative recombination rates and n_m the associated ideality factor for each non-radiative recombination mechanism m ($m \in \{SRH, Auger, \ldots\}$).

Under TPV operating conditions, J_{ph} is several orders of magnitude higher than $q\ R_{r,rad,sc}$ and $q\ R_{r,m}$ so it can be approximated under illumination as:

$$J(V) = J_{ph} - qR_{r,rad,sc}\ e^{\frac{qV}{k_B T}} - q\sum_{m} R_{r,m}\ e^{\frac{qV}{n_m k_B T}}\ . \qquad 4\text{-}6$$

The photo-generated current J_{ph}, assuming perfect external quantum efficiency, can be calculated by counting the number of photons absorbed within the material

$$J_{ph} = q\int_{0}^{+\infty} \frac{\lambda}{hc}\ I(T_{source}, \lambda) a_{front}(\lambda) d\lambda = qR_g \qquad 4\text{-}7$$

where $I(T_{source},\lambda)$ is the temperature and wavelength-dependent blackbody irradiance, $a_{front}(\lambda)$ is the absorptivity from the front of the cell and R_g is the photo-generation rate.

The losses arising from Auger and Shockley-Read-Hall (SRH) recombination processes are important for TPV cells, as outlined in section 2.2.2 of this thesis. Therefore both of these have been included in this model while other recombination mechanisms like surface recombination have been neglected. The current density

equation can hence be rewritten as

$$J(V) = q\left(R_g - R_{r,rad,sc}e^{\left(\frac{qV}{k_BT}\right)} - R_{r,SRH}(V) - R_{r,Auger}(V)\right) \quad 4\text{-}8$$

where $R_{r,SRH}(V)$ is the voltage-dependent Shockley-Read-Hall recombination rate and $R_{r,Auger}(V)$ is the voltage-dependent Auger recombination rate.

4.1.4 Bulk Non-Radiative Recombination

As mentioned in the previous section, one of the non-radiative recombination mechanisms considered in this model are the Shockley-Read-Hall recombinations. It is assumed that the SRH recombinations arise only due to threading dislocations and impacts of all other crystal defects have been neglected. This is due to the fact that the density of threading dislocations, formed as a result of lattice mismatch between the GaInAs cell and the substrate it has been grown on, has much higher impact on creation of recombination centres and trap states than any other crystal defects that could form during MBE growth. For more details on loss mechanisms and recombination centres see section 2.2.2.

Based on these assumptions, the model developed by Yamaguchi et al. [5] was used to determine the Shockley-Read-Hall recombination rates in the analysed cells. According to this model, the minority-carrier diffusion length associated with the threading dislocation density N_{TD}, for both types of carriers, can be expressed as:

$$L_{TD} = \sqrt{\frac{4}{\pi^3 N_{TD}}}, \quad 4\text{-}9$$

while the voltage-dependent threading-dislocations-related recombination rate is given by

$$R_{r,SRH} = \frac{n_i W_D}{2} \frac{D_p}{L_{TD}^2} e^{\left(\frac{qV}{2k_BT}\right)} = R_{r,SRH,sc} e^{\left(\frac{qV}{2k_BT}\right)} \quad 4\text{-}10$$

where n_i is the intrinsic carrier concentration given by the classic relation

$$n_{i,GaInAs} = \sqrt{N_c N_v} e^{\frac{-E_g}{2k_BT}} , \quad 4\text{-}11$$

D_p is the minority-carrier diffusion coefficient of holes and W_D is the depletion width of the cell calculated using

$$W_D = \sqrt{\frac{2\varepsilon_0 \varepsilon_r}{q} \frac{k_BT}{q} ln\left(\frac{N_a N_d}{n_{i,GaInAs}^2}\right)\left(\frac{1}{N_a} + \frac{1}{N_d}\right)} . \quad 4\text{-}12$$

From these equations it can be noted that the only parameters needed to evaluate the impact of threading dislocation density (TDD) on the performances of the cells are the diffusion coefficients of electrons and holes, $D_n(Ga_xIn_{1-x}As)$ and $D_p(Ga_xIn_{1-x}As)$, the densities of states in the conduction and valence bands, $N_c(Ga_xIn_{1-x}As)$ and $N_v(Ga_xIn_{1-x}As)$, and the relative permittivity $\varepsilon_r(Ga_xIn_{1-x}As)$. The formulas used to calculate all of these electrical parameters of the modelled $Ga_xIn_{1-x}As$ cells can be found in Table 4.1.

Effects of another non-radiative recombination mechanism, the Auger recombination, have been included in the model as well since they are the dominant loss mechanism in low-bandgap semiconductors as those used for TPV cells (see section 2.2.2 for details on Auger recombination mechanisms). Low doping density has been assumed within the cell in order to simplify the calculations, although this is not strictly correct for real devices.

Electronic parameter	**Equation**	**Source**
Bandgap **[eV]**	$E_g(Ga_xIn_{1-x}As)$ = $0.436x^2+0.629x+0.36$	[6]
Diffusion coefficient of electrons **[cm²/s]**	$D_n(Ga_xIn_{1-x}As)$ = $(10-20.2x+12.3x^2)\cdot 10^2$	[7]
Diffusion coefficient of holes **[cm²/s]**	$D_p(Ga_xIn_{1-x}As)$ = $16.42x^2-19.42x+13$	Extrapolated from [7], [8] and [10]
Density of states in the conduction band **[cm⁻³]**	$N_c(Ga_xIn_{1-x}As) = 2.289\cdot 10^{17} x^2 +1.541\cdot 10^{17} x +8.7\cdot 10^{16}$	Extrapolated from [7], [9] and [10]
Density of states in the valence band **[cm⁻³]**	$N_v(Ga_xIn_{1-x}As) = 1.124\cdot 10^{17} x^2 +2.288\cdot 10^{18} x +6.6\cdot 10^{18}$	Extrapolated from [7], [9] and [10]
Relative permittivity	$\varepsilon_r(Ga_xIn_{1-x}As)$ = $0.67x^2-2.87x+15.1$	[7]

Table 4.1. Formulas used for calculations of electronic parameters of GaInAs and their respective sources.

As given by Tidje et al., the voltage-dependent Auger recombination rate can be expressed as:

$$R_{r,Auger} = C_{Auger} L n_{i,GaInAs}^3 e^{\left(\frac{3qV}{2k_BT}\right)} = R_{r,Auger,sc} e^{\left(\frac{3qV}{2k_BT}\right)} \qquad 4\text{-}13$$

where L is the thickness of the cell and the ambipolar Auger coefficient C_{Auger}=3.2×10^{-28} cm^6.s^{-1} has been used [11]. The cell is assumed to be cooled down to 300 K since the simulations showed that performances of the cells are severely

reduced if their temperature is increased. For more detail on this effect see section 4.2.1 where the aforementioned simulations results are presented.

Having derived the expressions for voltage-dependent Auger and SRH recombinations, the full current-voltage characteristic of the modelled cell is given by

$$J(V) = q\left(R_g - R_{r,rad,sc}(V) - R_{r,SRH}(V) - R_{r,Auger}(V)\right) \tag{4-14}$$
$$= q\left(R_g - R_{r,rad,sc}e^{\left(\frac{qV}{k_BT}\right)} - R_{r,SRH}e^{\left(\frac{qV}{2k_BT}\right)} - R_{r,Auger}e^{\left(\frac{3qV}{2k_BT}\right)}\right).$$

The voltage and current density at the maximum power point are then calculated by maximising the $J \times V$ product using the formula from Eq. 4-14. From there the efficiency η of the cell can be expressed as

$$\eta = \frac{J_{mpp} \times V_{mpp}}{P_{in}} \tag{4-15}$$

where J_{mpp} is the current density at maximum power point, V_{mpp} is the voltage at maximum power point and P_{in} is the power delivered to the front surface of cell from the thermal emitter.

4.2 Results and Discussion

4.2.1 Effects of Cell Temperature

Due to high incident power densities used in TPV systems it is logical to assume that the cell material would be heated up during the operation of the device due to non-ideal energy conversion caused by various loss mechanisms as described in sections 2.2.2 and 4.1.4. The temperature of the cell is included in all the recombination rates expressions, as can be seen from the equations in the previous

section, and is inversely proportional to the related current densities. This in turn indicates that it has a significant impact on the final efficiency calculation. The exact scale of this effect was however unknown, therefore the model was first used to simulate the impact of increase in the temperature of the cell on its performance.

In these simulations the temperature of the source has been set to 1300 K and the power density delivered to the cell to 500 kW.m^{-2}. Auger recombinations have been taken into account and SRH recombinations have been assumed to be low enough not to impact the operation of the cell. Figure 4.3 shows the impact of the increase of the cell temperature on the performance of a 5-μm-thick $Ga_xIn_{1-x}As$ TPV cell with perfect light trapping. Since the temperature of the material has a large impact on its bandgap, the composition has been plotted instead of the bandgap.

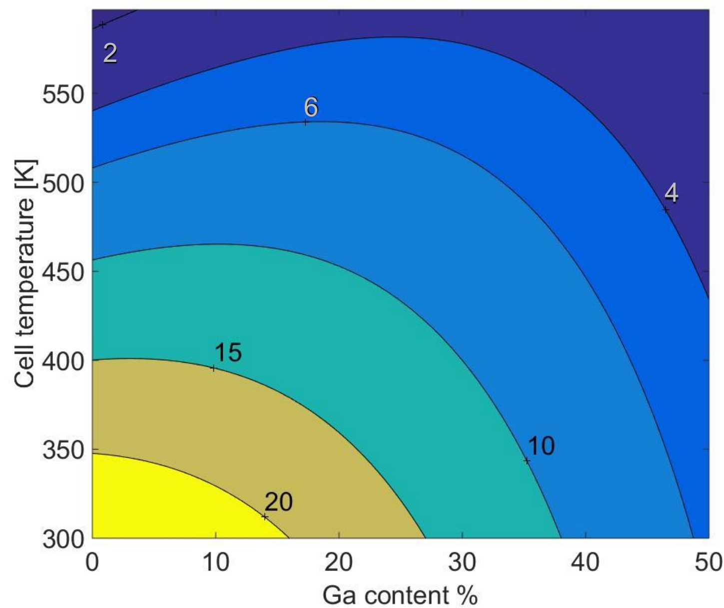

Figure 4.3. Maximal theoretical efficiency *η* of a $Ga_xIn_{1-x}As$ cell with perfect light trapping as a function of the temperature of the cell *T* and the Ga composition.

From Figure 4.3 above it can be noted that increasing both the temperature and the gallium content in the modelled cell very quickly has a severe negative impact on the maximum efficiency. The effects of different thicknesses and architectures of the cell are discussed in detail in the next section of this chapter. To better visualise the impact of the increase in cell temperature on the performance as well as the optimal bandgap, another plot was created and is presented as Figure 4.4 below. Once again, the gallium percentage for the best-matched bandgap rather than the optimal bandgap itself has been used since the bandgap varies with temperature and composition does not. Therefore, it is more important to know the composition of the material used and the bandgap can be calculated from there if needed.

From the black line on the plot in Figure 4.4 we can see that increasing the temperature of the cell from 300 to 400 K reduces the maximum theoretical efficiency from 24.7% to only 15.3%. Further increase in cell temperature causes the efficiency to drop even faster, reaching a mere 3.5% at 600 K. The main reason behind this trend is Auger recombination. When the temperature of the cell is increased, its bandgap drops leading to immense levels of Auger recombinations.

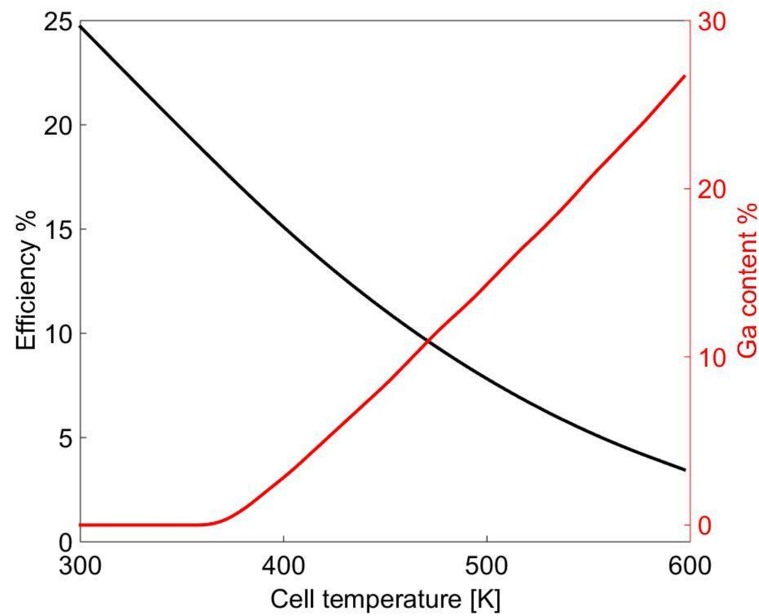

Figure 4.4. Maximal theoretical efficiency η (black, left scale) and optimal Ga composition for best-matched bandgap (red, right scale) of a $Ga_xIn_{1-x}As$ cell with perfect light trapping as a function of the temperature of the cell T.

Looking at the red line in Figure 4.4 representing Ga content, we can see that at low cell temperatures, between 300 and 370 K, the optimum Ga content is zero so a pure InAs cell gives the highest efficiency. As the temperature of the cell increases further, the preferred bandgap increases as well. This is to be expected since increasing the bandgap through increasing the Ga composition reduces the Auger recombination rate and hence improves the efficiency of the cell.

Figure 4.5 shows the dependence of the bandgap of GaInAs compounds on the composition of the material as well as its temperature. It is a good illustration of how severely the bandgap is impacted by even a small increase in the temperature of the cell. The resulting non-radiative recombination rates are so high that they prevent the extraction of the photo-generated carriers by severely reducing their lifetimes.

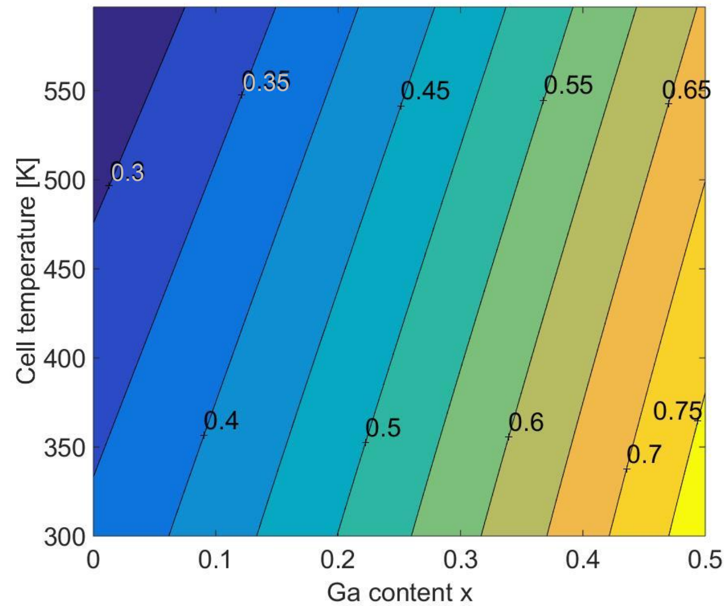

Figure 4.5. The bandgap E_g of a $Ga_xIn_{1-x}As$ cell with perfect light trapping as a function of the temperature of the cell T and the Ga composition.

Based on these findings the cell temperature was set to 300 K throughout all the further simulations. These results confirm that cell cooling is essential in TPV systems in order to maintain good efficiency of power conversion.

4.2.2 Impact of the Cell Thickness and Light Trapping

The next set of simulations was designed to investigate the impact of the thickness of the cell on the maximum theoretical efficiency achievable and to examine any differences between the results for both modelled architectures. The temperature of the source has been set to 1300 K and the power density delivered to the cell to 500 kW.m^{-2}, both reasonable for TPV systems. Auger recombinations have been taken into account and SRH recombinations are assumed to be too low to impact the

operation of the cells.

From Figure 4.6 it can be immediately noticed that there are significant differences in the behaviour of cells with different architectures. Figure 4.6(a) shows the impact of the thickness of the cell on the performance of a device with a textured front surface and a perfect back mirror, i.e. with an ideal light trapping mechanism. It can be seen that it takes about 350 nm to achieve a reasonable level of absorption and the maximum efficiency is reached at around 500 nm, exact value depending on the bandgap. It is possible to achieve high efficiencies in these cells with only 0.5-1 μm because of the light trapping. Increase in the effective optical path of the incoming photons makes the absorption of the cell much better than its thickness would suggest. Making the cell thicker does not impact the efficiency of cells with bandgaps of 0.45 eV and above. However, an interesting trend is observed for cells with lower bandgaps. The maximum efficiency is achieved between 0.5 and 1 μm, while further increase in thickness reduces it. This is due to increased level of Auger recombination rate in low-bandgap materials, as explained in section 4.2.1 above.

For cells without light trapping the general trend is much simpler. The efficiency reaches its maximum when the cell is sufficiently thick to absorb all the incoming photons, in this case around 3 μm is enough. Further increase in the thickness does not impact the efficiency in any way. Auger-related efficiency boost for smaller thicknesses is not observed since without light trapping the optical path of the incoming photons is at most equal to the thickness of the cell and hence the losses due to partial absorption are much greater than those generated by Auger

recombinations.

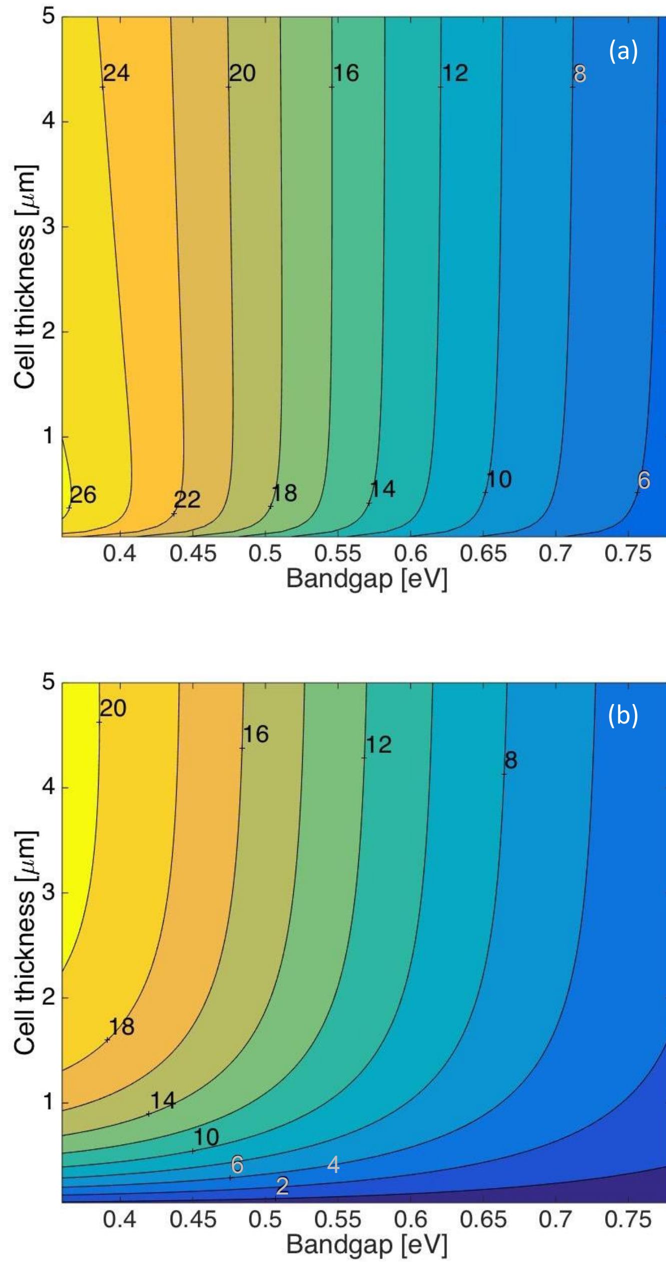

Figure 4.6. Maximal theoretical efficiency η of a $Ga_xIn_{1-x}As$ cell with (a) and without (b) perfect light trapping as a function of the thickness of the cell L and the bandgap of the cell E_g.

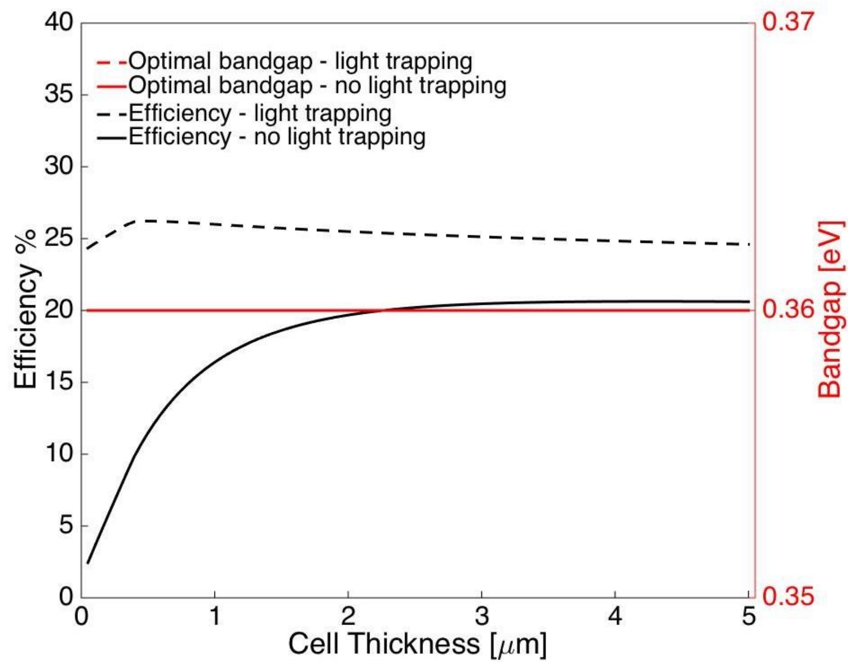

Figure 4.7. Maximal theoretical efficiency η (black, left scale) and the bandgap of the cell E_g (red, right scale) of a $Ga_xIn_{1-x}As$ cell with (dashed lines) and without (solid lines) perfect light trapping as a function of the thickness of the cell L.

Trends for the both architectures are best visible in Figure 4.7 where the maximum theoretical efficiency and the optimum bandgap have been plotted for cell thicknesses up to 5 μm. The boost in efficiency for thin cells with light trapping can be observed as a “bump” in the dashed line around 0.5 μm. Optimum bandgap for both architectures at all thicknesses is the lowest one possible, 0.36 eV of InAs. This is to be expected for the temperature of the thermal radiator used (see section 4.2.4) and confirms that the thickness of the material does not impact the blackbody temperature – optimum bandgap relation.

4.2.3 Threading Dislocations

In the previous simulations the impact of threading dislocations-related Shockley-Read-Hall (SRH) recombinations has been neglected by assuming that the density of the dislocation is low and does not cause any noticeable losses. Logically, it was an important step to investigate in detail up to what levels exactly the threading dislocation density (TDD) has no impact on the performance of the cells and when it becomes a problem.

A 5-μm-thick $Ga_xIn_{1-x}As$ TPV cell has been chosen for these simulations, the thermal emitter temperature has been set to 1300 K and the incident power to 500 $kW.m^{-2}$. The losses related to Auger recombinations have been taken into account, same as for all the other simulations presented in this chapter. Figure 4.8 shows the plots of maximum theoretical efficiencies for cells of various compositions with (a) and without (b) light trapping as a function of the TDD. The shapes of the contour lines look practically identical for both architectures, only the numerical values of efficiencies vary with up to 4% boost for cells with textured front surface and a back mirror with the same bandgap and TDD.

It can be observed from Figure 4.8 and Figure 4.9 that the TDD densities up to 10^4 cm^{-2} have a negligible impact on the efficiencies. When the dislocation density is increased to 10^5 cm^{-2}, the impact of the SRH recombinations starts to be noticeable. They reduce the open-circuit voltage and hence lower the efficiency of the cells. Increasing the TDD even further, over 10^6 cm^{-2}, shortens the diffusion lengths of the carriers since they are more easily trapped by the dislocations.

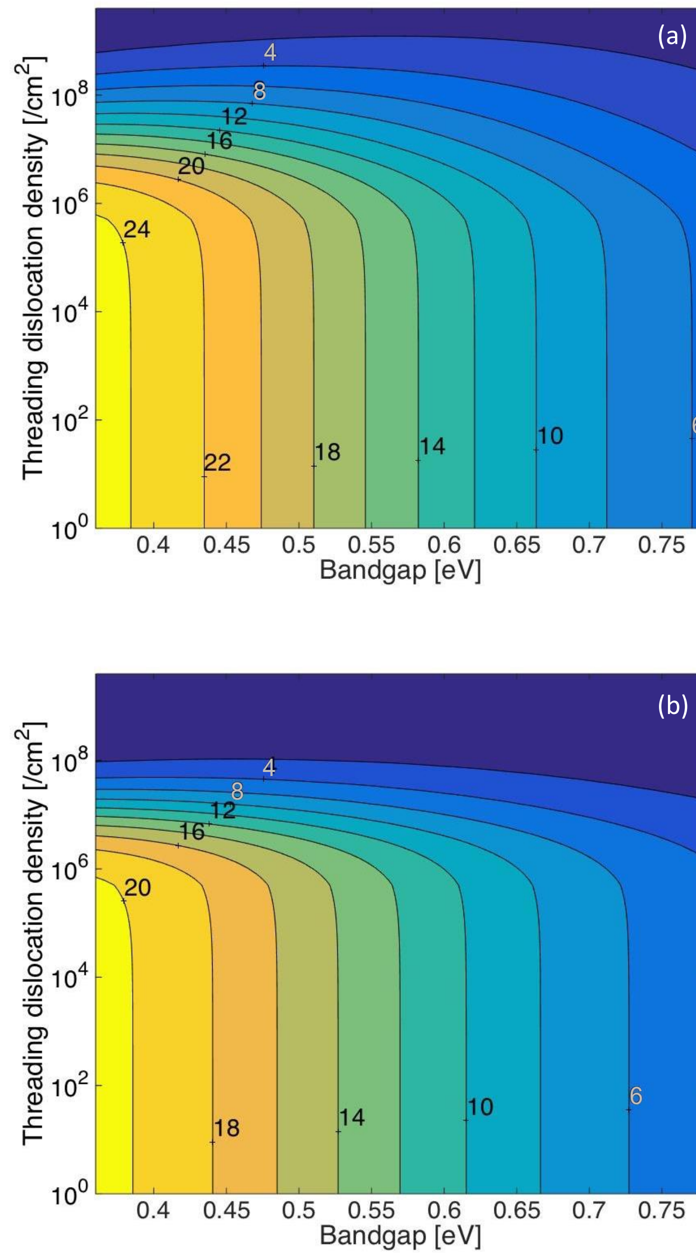

Figure 4.8. Maximal theoretical efficiency η of a $Ga_xIn_{1-x}As$ cell with perfect light trapping (a) and without it (b) as a function of the threading dislocation density N_{TD} and the bandgap of the cell E_g.

Eventually, the diffusion lengths become smaller than the thickness of the cell and hence the carriers collection is impacted resulting in reduction in short-circuit current and further lowering of the overall efficiency. It can be observed that at

densities of 10^7 cm^{-2} the efficiency is only half of the original one and it drops to as low as 7% (3%) for cells with (without) the light trapping mechanism at 10^8 cm^{-2}, to eventually reach zero. The optimal bandgap of 0.36 eV remains unaffected up to TDD values of 10^7 cm^{-2}. Based on these results it can be concluded that TDD up to 10^5 cm^{-2} are acceptable and this number should not be exceeded for real devices to ensure good performance of the cells.

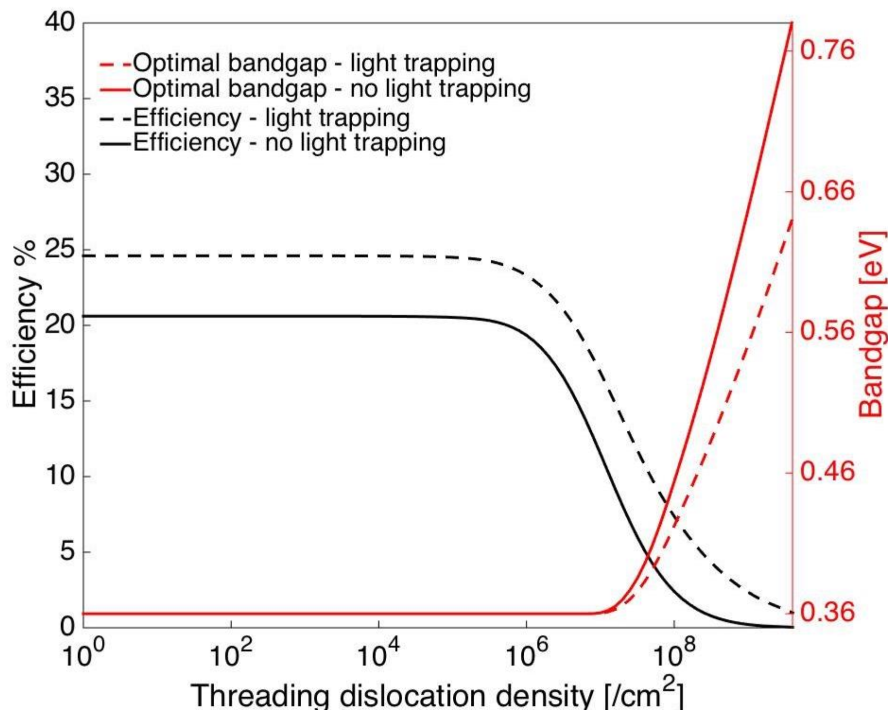

Figure 4.9. Maximal theoretical efficiency η (black, left scale) and the bandgap of the cell E_g (red, right scale) of a $Ga_xIn_{1-x}As$ cell with (dashed lines) and without (solid lines) perfect light trapping as a function of the threading dislocation density N_{TD}.

The model used for the evaluation of the impact of the reduced diffusion lengths of the minority carriers assumes a uniform generation rate. As this hypothesis is not verified in real devices, results for TDDs over 10^6 cm^{-2} are not strictly accurate.

However, the overall model gives a good approximation on how threading dislocations affect the performance of the cells.

4.2.4 Impact of the Thermal Emitter Temperature and Incident Power Density

The most important parameters of a thermal emitter used as a source in a TPV system are its temperature and the distance at which it is from the cell. The temperature dictates the spectrum of emission, especially the main emission wavelength, and the distance determines the amount of power that is delivered to the cell. Usually in TPV systems the two are linked since a blackbody at a certain temperature emits a set amount of power. All the previous modelling of TPV systems I have come across in my research just assume that all the power emitted by the blackbody is delivered to the cell. However, in reality significant amount of power is lost and only part of the initial energy arrives at the cell, unless the cell is within thermal coupling distance from the radiator. On the other hand, if a concentrator system was to be used, like those for concentrated solar, more power could be delivered. In our model we decouple the temperature of the emitter and the power density incident on the cell in order to investigate all of the aforementioned possibilities.

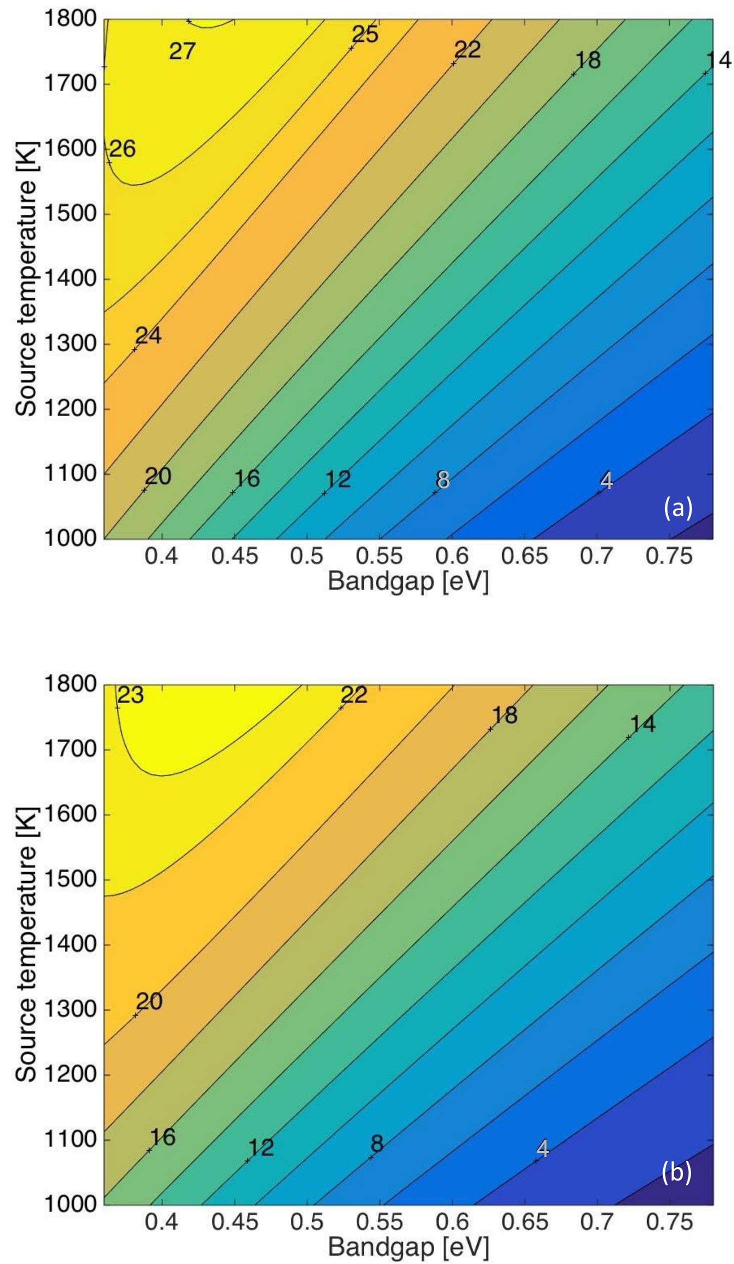

Figure 4.10. Maximal theoretical efficiency η of a $Ga_xIn_{1-x}As$ cell with perfect light trapping (a) and without it (b) as a function of the temperature of the thermal emitter T_{source} and the bandgap of the cell E_g.

At first, a range of source temperatures between 1000 and 1800 K was investigated. The incident power density was set to 500 kW.m^{-2}, which can be

achieved at most of these temperatures without need for any concentrator systems. More details on the effects of the incident power density on the performances of the cells are presented later on in this section. From there it can be seen that choosing a different value for power in the temperature-dependent plot would not affect the general shape of the graph. Therefore the trends observed for these parameters from plots in Figure 4.10 are independent of the power used, just the values for efficiencies would change. In these simulations we have used two architectures, one with the perfect light trapping and one with a flat front surface and no back mirror. The impact of Auger recombinations have been taken into account and SRH recombination rate set to low enough not to affect the performance of the cells. A 5-μm-thick cell was chosen for all of the simulations presented in this section in order to ensure full absorption for both investigated architectures.

From the plots (a) and (b) in Figure 4.10 it can be easily noticed that the general shape of the two graphs is exactly the same, which indicates that the architecture has no impact on the response of the cell to specific spectral wavelength and it only impacts the overall efficiency. Two general trends can be observed here: the efficiency drops when the bandgap of the cell is increased and it is increases with rising temperature of the source. The optimal bandgap for specific temperatures can be more easily seen from plot in Figure 4.11. Up to just over 1400 K the cells prefer the lowest possible bandgap, 0.36 eV of InAs. However, when the temperature rises further, the optimal bandgap is increased as well. This is due to the fact that the peak wavelength of the blackbody emission decreases with temperature so cell with higher

bandgap is more efficient at converting the incoming radiation (see section 2.1.1 for details). Also higher bandgap means less Auger recombinations, which further contributes to the increase in efficiency.

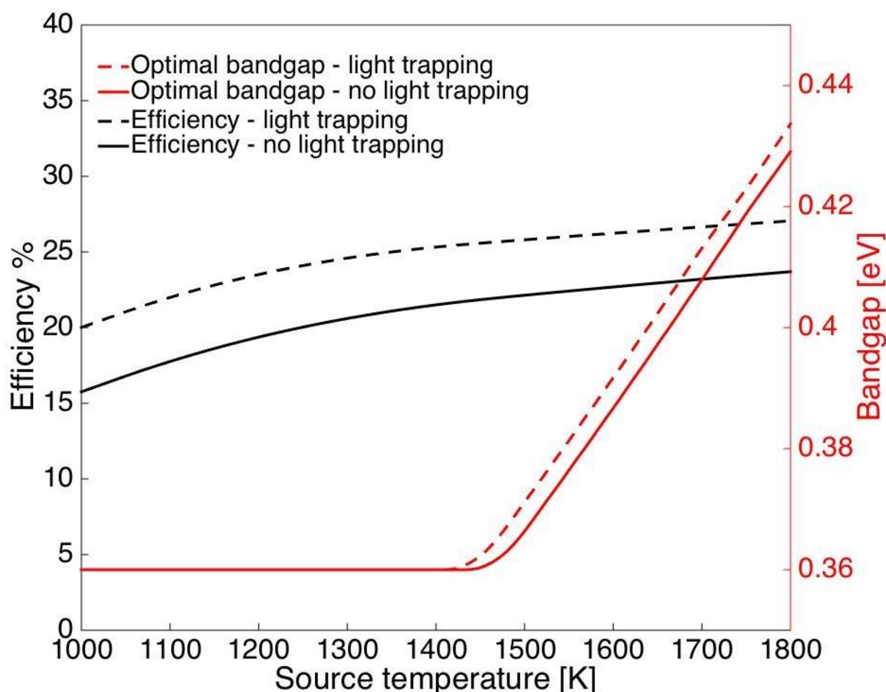

Figure 4.11. Maximal theoretical efficiency η (black, left scale) and the bandgap of the cell E_g (red, right scale) of a $Ga_xIn_{1-x}As$ cell with (dashed lines) and without (solid lines) perfect light trapping as a function of the temperature of the thermal emitter T_{source}.

From the maximum efficiency plot in Figure 4.11 it can be noted that the general trends are the same for both architectures, as observed before from Figure 4.10. The only difference is an increase by approx. 4% in the overall efficiency of the cell when the architecture with light trapping is used. At source temperature of only 1000 K the maximum efficiency of 20% can be achieved. It increases to 25% around 1350 K to reach over 27% at 1800 K. Further increase in the temperature of the source would

further improve the performance of the cells, however in practice it is not a feasible option to use sources at higher temperatures for TPV applications. It is also worth noticing that increasing the temperature of the source by 450 K from 1350 to 1800 K results in only 2% boost in efficiency and also requires bandgap adjustments. Therefore in all of our other simulations we have used 1300 K as the temperature of the source as it seems to be the best realistically achievable value yielding good performances but also limiting overheating of the cell.

Figure 4.12 shows the maximum theoretical efficiencies of cells with different bandgaps for a range of incident power densities. The impact of Auger recombinations has been taken into account, while the threading dislocation density has been assumed to be low enough to have negligible effect on the operation of the cell. The temperature of the thermal emitter has been set to 1300 K, a typical value for TPVs.

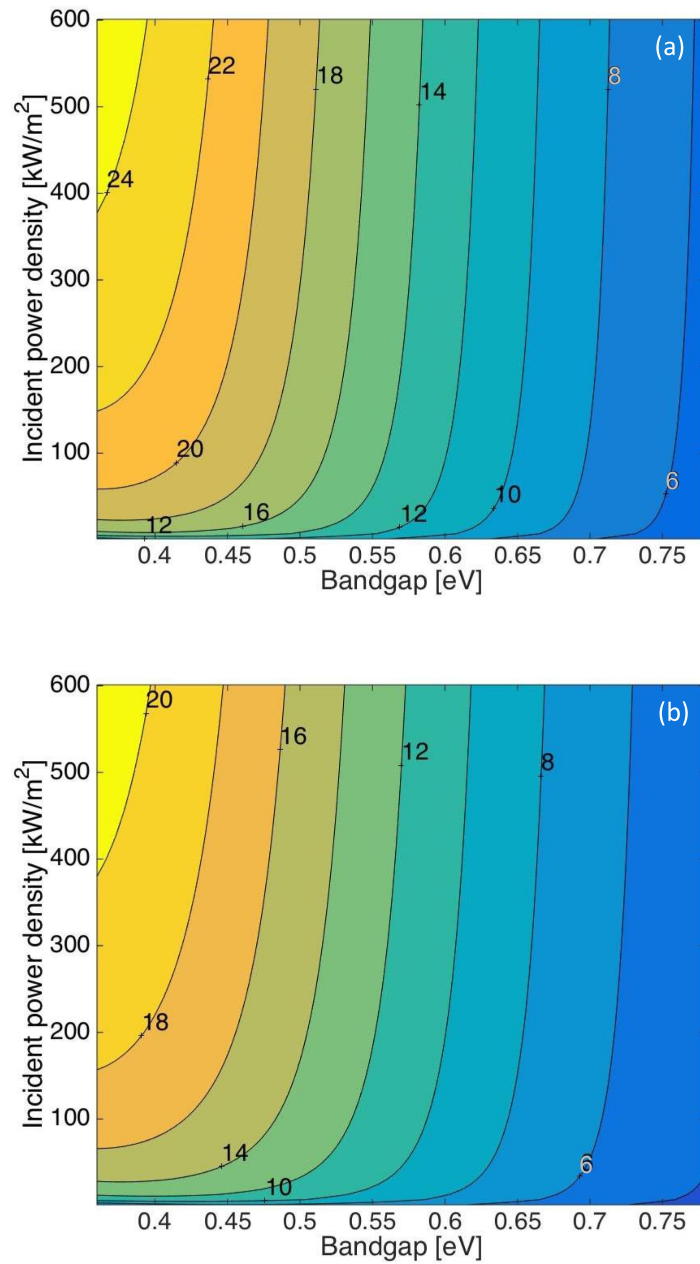

Figure 4.12. Maximal theoretical efficiency η of a $Ga_xIn_{1-x}As$ cell with perfect light trapping (a) and without it (b) as a function of the incident power density P_{in} and the bandgap of the cell E_g.

Similarly to the source temperature-dependent plots, the general shape does not change between the two different architectures investigated. Increasing the incident

power density improves the efficiency, especially for cells with low bandgaps. Using just 1 kW.m^{-2} (intensity of solar spectrum AM1.5) yields 15% efficiency for an InAs cell with light trapping architecture. Increasing the intensity to 100 kW.m^{-2} boosts the efficiency to 21% for the same cell. Applying much higher intensity of 500 kW.m^{-2} results in an improvement by an absolute of 3.5% to 24.5% in total. The small difference in efficiencies for a large increase in power from 100 to 500 kW.m^{-2} is to be expected due to the logarithmic nature of evolution of the efficiency as a function of incident power density. This is confirmed by the plots in Figure 4.13, which shows the maximum efficiencies and optimal bandgaps for cells with and without light trapping for a range of incident power densities from 1 to 600 kW.m^{-2}.

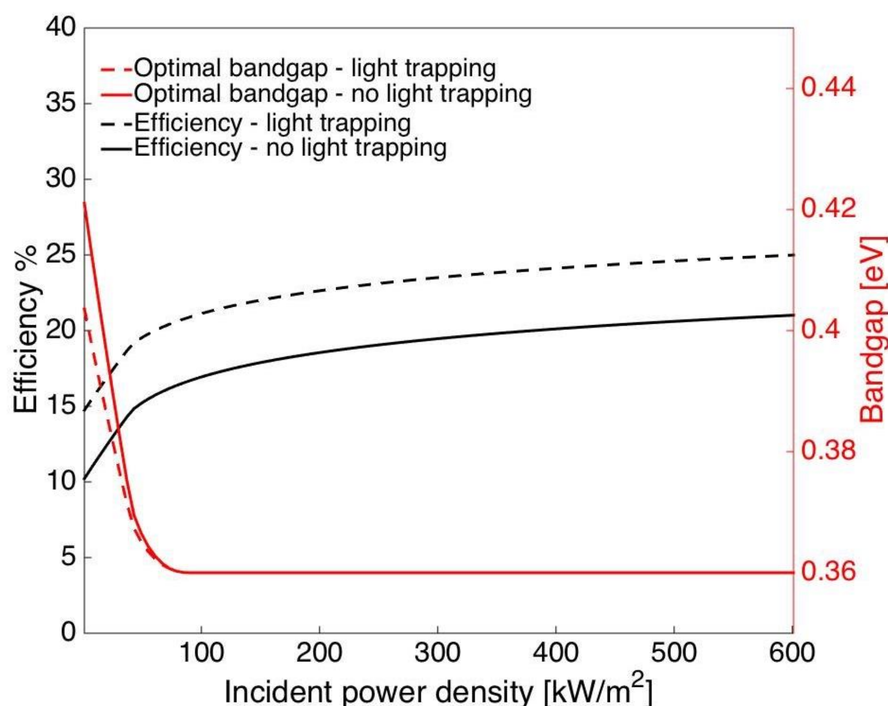

Figure 4.13. Maximal theoretical efficiency η (black, left scale) and the bandgap of the cell E_g (red, right scale) of a $Ga_xIn_{1-x}As$ cell with (dashed lines) and without (solid lines) perfect light trapping as a function of the incident power density P_{in}.

From Figure 4.13 it is easy to see the trend of the efficiency as a function of incident power. The improvement is minimal for values over 100 kW.m^{-2}, therefore in real life the distance between the cell and the source can be adjusted so that the cell does not overheat but still at last 100 kW.m^{-2} is delivered. From this plot it can also be seen that choosing any value between 100 and 600 kW.m^{-2} for all of the other simulations in this paper would give the same results in terms of trends, the only difference being the maximum efficiency values. The optimal bandgap is as could be expected 0.36 eV of InAs for most of the incident power densities, namely all powers above 90 kW.m^{-2}.

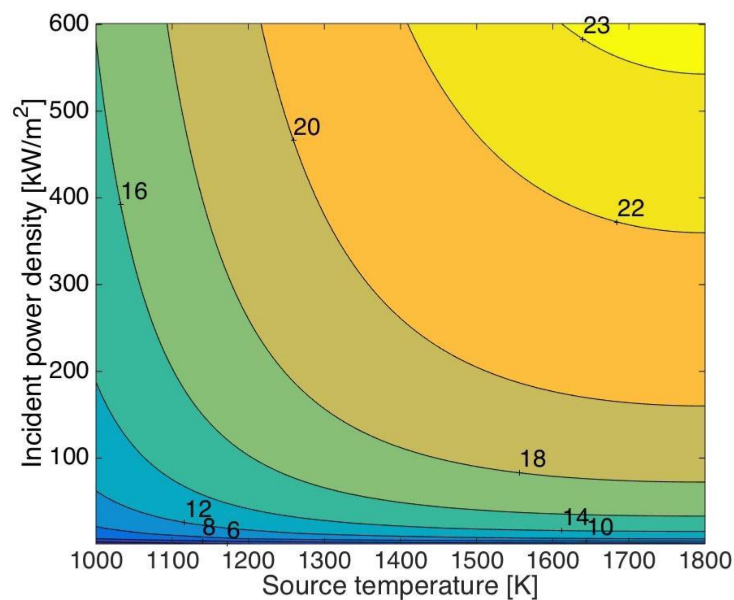

Figure 4.14. Maximal theoretical efficiency η of an InAs cell with perfect light trapping as a function of the incident power density P_{in} and temperature of the thermal emitter T_{source}.

The aim of the simulations presented in this section is to determine the optimal bandgap to be used with a source at a specific temperature with set power density.

The model can also be used the other way around, i.e. to determine optimal operating conditions for a cell with a specific bandgap. An example of this is shown in Figure 4.14, which shows the maximum theoretical efficiencies of an InAs cell operating with sources at temperatures between 1000 and 1800 K and incident power densities between 1 and 600 kW.m^{-2}. It can be observed that for example if we are aiming at efficiencies of 20% and above, there is a wide range of operating parameters to choose from, depending if it is more important to lower the power density or to adjust the temperature of the source. These results can be useful in establishing the best-matched operating parameters for real devices and shows how these two can be adjusted to achieve high efficiencies.

4.3 Conclusions

A theoretical model has been developed in order to evaluate performances of different compositions of $Ga_xIn_{1-x}As$ TPV cells. Blackbody theory extended to semiconductors and flow equilibrium in the cell have been used as the main basis. Also two absorption models have been used in order to investigate different architectures of the cells. The number of electronic parameters required for simulations have been minimised in order to circumvent the issue of lack of accurate data on the properties of the investigated materials. The number of inputs into the model has been reduced to only three, namely the blackbody emission spectrum, bandgaps of various compositions of $Ga_xIn_{1-x}As$ and their absorption spectra. Because of low bandgaps of the investigated materials, Auger recombination-related

losses have been taken into account in all the simulations as they are intrinsic to the semiconductors and cannot be avoided.

At first the impact of heating of the cell was investigated in order to establish an optimal realistic temperature that the cell should be cooled down to for best performance. It was shown that temperatures above 300 K have a devastating impact on the maximum efficiencies achievable by the cells. Increasing the temperature by 50 degrees cuts about 5% of the total efficiency therefore cell cooling is essential in all TPV systems.

The next set of simulations focused on the effects of the thickness of the cell for both types of architectures used. Significant differences have been observed between the cells with and without the light trapping mechanism. Cells with flat front surface and no back mirror need 3 μm or more to be able to absorb all the incoming photons and hence reach their maximum efficiencies. On the other hand cells with textured front surface and reflective back mirror achieved highest efficiencies at just 0.5 μm due to significant increase in the length of the optical path of photons within the cell. However, when the cell is thicker, the efficiency does not improve any further, it actually drops slightly, especially for cells with lowest bandgaps. This is due to a great increase in Auger recombination rate when the bulk volume of the cells increases.

Because the main goal of the modelling of these $Ga_xIn_{1-x}As$ TPV cells was to help with design of real life devices to be grown later by the MBE system, the impact of crystal defects on the performances of the cells was studied in detail. As In-rich $Ga_xIn_{1-x}As$ compositions are not lattice-matched to any of the substrate materials,

there is a need of buffered growth on substrates with different lattice constant than the cell material. This introduces strain, which leads to defects and formation of threading dislocations. If the density of these threading dislocations (TDD) is high, the trap states they form "catch" some free carriers, which impacts the diffusion lengths of the carriers and affect their collection. The higher the TDD, the more negative impact it has on the efficiency of the cells. We have demonstrated that 10^5 cm^{-2} should not be exceeded for real life devices.

The impact of the incident power density and the temperature of the thermal emitter have been investigated as well. It has been shown that increasing the power density between 100 and 600 $kW.m^{-2}$ has a small impact on the total efficiency achievable by the cell and therefore there is no need for very high power densities for the cells to perform well. The temperature of the source has more impact on the efficiencies of the cells, especially that at each temperature the blackbody has a different peak emission wavelength. This means that different bandgaps are optimal for different source temperatures. For range between 1000 and 1400 K, usual values for TPV systems, the optimal bandgap is that of InAs and efficiencies up to 25% can be achieved. Increase in the temperature does further improve the performance of the cells, however the optimal bandgap is shifted towards higher values. Both of these parameters can be used to either determine the optimal bandgap for a cell operating at set conditions or to establish the best operating conditions for a cell with a specific bandgap. They can also help to estimate how close practical devices are to their maximum potential. Moreover, this model can be easily adapted to simulate cells with

different architectures than those presented here and made of different semiconductor materials.

4.4 References

1. E. Yablonovitch and G. Cody, Intensity enhancement in textured optical sheets for solar cells, *IEEE Trans. Electron Devices 29(2)*, 1982.
2. O. Miller, E. Yablonovitch, and S. Kurtz, Strong Internal and External Luminescence as Solar Cells Approach the Shockley–Queisser Limit, *IEEE J. Photovoltaics 2*, 2012.
3. P. Würfel, The Chemical Potential of Radiation, *J. Phys. C: Solid State Phys. 15(18)*, 1982.
4. S. S. Li, Semiconductor Physical Electronics, Chap. 11, *Springer*, 2005.
5. M. Yamaguchi and C. Amano, Efficiency calculations of thin-film GaAs solar cells on Si substrates, *J. Appl. Phys.*, 1985.
6. R. Nahory, M. Pollack, W. Johnston, and R. Barns, Band gap versus composition and demonstration of Vegard's law for $In_{1-x}Ga_xAs_yP_{1-y}$ lattice matched to InP, *Appl. Phys. Lett. 33*, 1978.
7. Basic Parameters at 300K, Band structure and carrier concentration and Electrical Properties of GaxIn1-xAs, *Ioffe Physical Technical Institute 2015*, accessed on 5th March 2015, http://www.ioffe.ru/SVA/NSM/Semicond/GaInAs/.
8. Band structure and carrier concentration of GaxIn1-xAsyP1-y, *Ioffe Physical Technical Institute 2015*, accessed on 5th March 2015, http://www.ioffe.ru/SVA/NSM/Semicond/GaInAs/.
9. Band structure and carrier concentration and Electrical Properties of GaAs, *Ioffe Physical Technical Institute 2015*), accessed on 5th March 2015,

http://www.ioffe.ru/SVA/NSM/Semicond/GaAs/.

10. Band structure and carrier concentration and Electrical Properties of InAs, *Ioffe Physical Technical Institute 2015*, accessed on 5th March 2015, http://www.ioffe.ru/SVA/NSM/Semicond/InAs/.

11. S. Hausser, G. Fuchs, A. Hangleiter, and K. Streubel, Auger recombination in bulk and quantum well InGaAs, *Appl. Phys. Lett. 56*, 1990.

Chapter 5:

GaInAs Thermophotovoltaic Cells Grown by MBE on GaAs Substrates

The main purpose of this thesis is growth and fabrication of high-quality semiconductor thermophotovoltaic cells. This chapter first describes the design of the devices and details of the MBE growth. Then it moves on to analysing the quality of the grown material and fabrication processes used to create working devices. Results from dark and illuminated JV measurements as well as photoluminescence before and after annealing are discussed. Finally, conclusions are drawn and future work ideas related to this chapter are presented.

5.1 Design of the Cells and MBE Growth

5.1.1 Structure of the Cells

It was decided to first grow the GaInAs TPV cells on GaAs substrate in order to minimise the lattice mismatch between the substrate and the cell and hence limit the density of threading dislocations arising from built up stress. Composition of the cell was chosen to be $Ga_{0.15}In_{0.85}As$ aiming for bandgap of around 0.45 eV, which has been demonstrated to be highly suitable for TPVs in Chapter 4 of this thesis and Ref. [1] to this chapter. Figure 5.1 shows the schematic drawing of layers within the structure and their compositions.

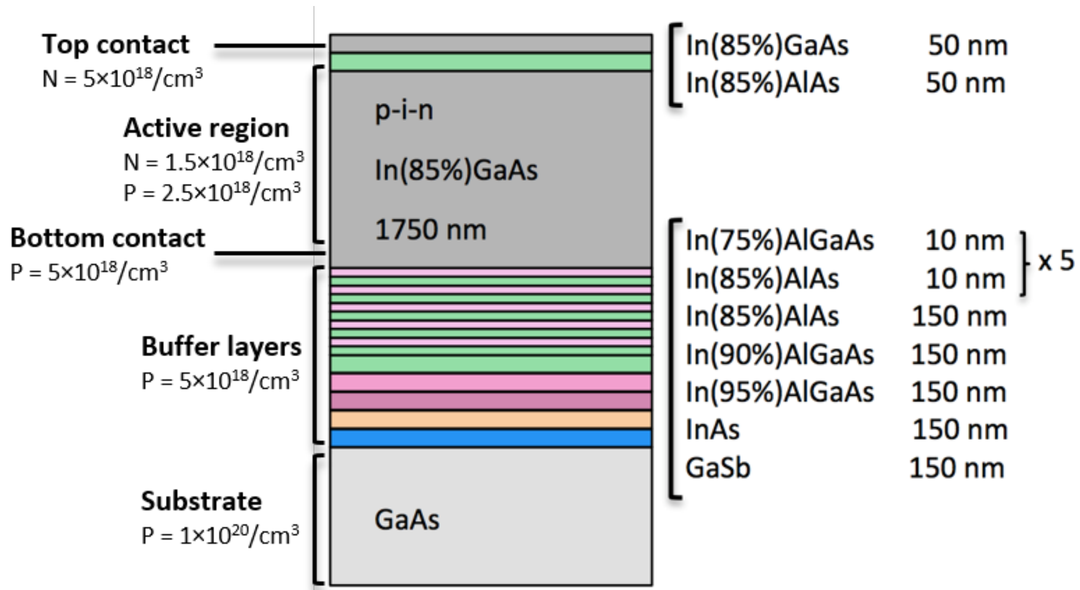

Figure 5.1. Structure of the GaInAs TPV cells grown by MBE detailing the layers and their compositions.

As can be seen from Figure 5.1, except for the 1750-nm-thick p-i-n InGaAs junction being the active area of the device, there are many more layers within the

cell. GaSb and InAs layers are the primary buffer layers designed to accommodate most of the stress accumulated during growth and to stop the threading dislocations from propagating into the active region. They are followed by three layers of graded buffer that is used to gradually change the lattice constant from that of the substrate to that of the p-i-n region. On top of these buffers there is a 10-layer InAlAs/InAlGaAs superlattice forming a so called dislocation filter layer. Its aim is to dissipate any remaining strain within the structure and effectively confine the threading dislocations that could be propagating from the lower layers. The final InAlAs layer is thicker and acts as a contacting layer. The p-i-n junction is placed on top of it. The last two layers are an InAlAs window and an InGaAs top contacting layer. The growth conditions of all of the layers are described in the next section.

5.1.2 MBE Growth

The sample described in the above section has been grown on a highly-p-doped, epi-ready (001) GaAs substrate in order to facilitate contacting through the bottom of the sample. The substrate has been heated up to 590°C to grow GaAs and then cooled to 510°C for GaSb buffer layer growth. The temperature has been reduced further to 480°C when the graded InAlGaAs buffer was being grown and then to 415°C for the superlattice growth. Beryllium doping has been applied to all of the aforementioned layers, resulting in doping levels of $N_a=5\times10^{18}cm^{-3}$, in order to ensure good carriers flow throughout the wafers all the way to the bottom of the substrate to allow use of a back-side p-type contact. After all the buffer layers have been grown,

the temperature was raised again to 480°C, optimal for GaInAs growth. A 1000-nm-thick, $2.5\times10^{18}cm^{-3}$ doped p-type $Ga_{0.15}In_{0.85}As$ layer has been grown first, followed by 500nm of intrinsic $Ga_{0.15}In_{0.85}As$ and then 250nm of n-type $1.5\times10^{18}cm^{-3}$ doped $Ga_{0.15}In_{0.85}As$, all together forming the p-i-n junction. N-type $In_{0.85}Al_{0.15}As$ window layer has been grown on top of it, also with $1.5\times10^{18}cm^{-3}$ doping level, and finally the contacting $Ga_{0.15}In_{0.85}As$ with higher, $5\times10^{18}cm^{-3}$ doping level. The n-type doping has been achieved using silicon as the donor dopant. After the contacting layer was complete, the sample has been cooled down to 100°C to finish off the growth.

5.2 Material Quality Analysis

5.2.1 Surface Morphology

In order to assess the quality of the grown materials several measurements can be made. For the sample presented in this chapter AFM, TEM, XRD and PL measurements have been performed. Detail on these techniques can be found in Chapter 3 of this thesis.

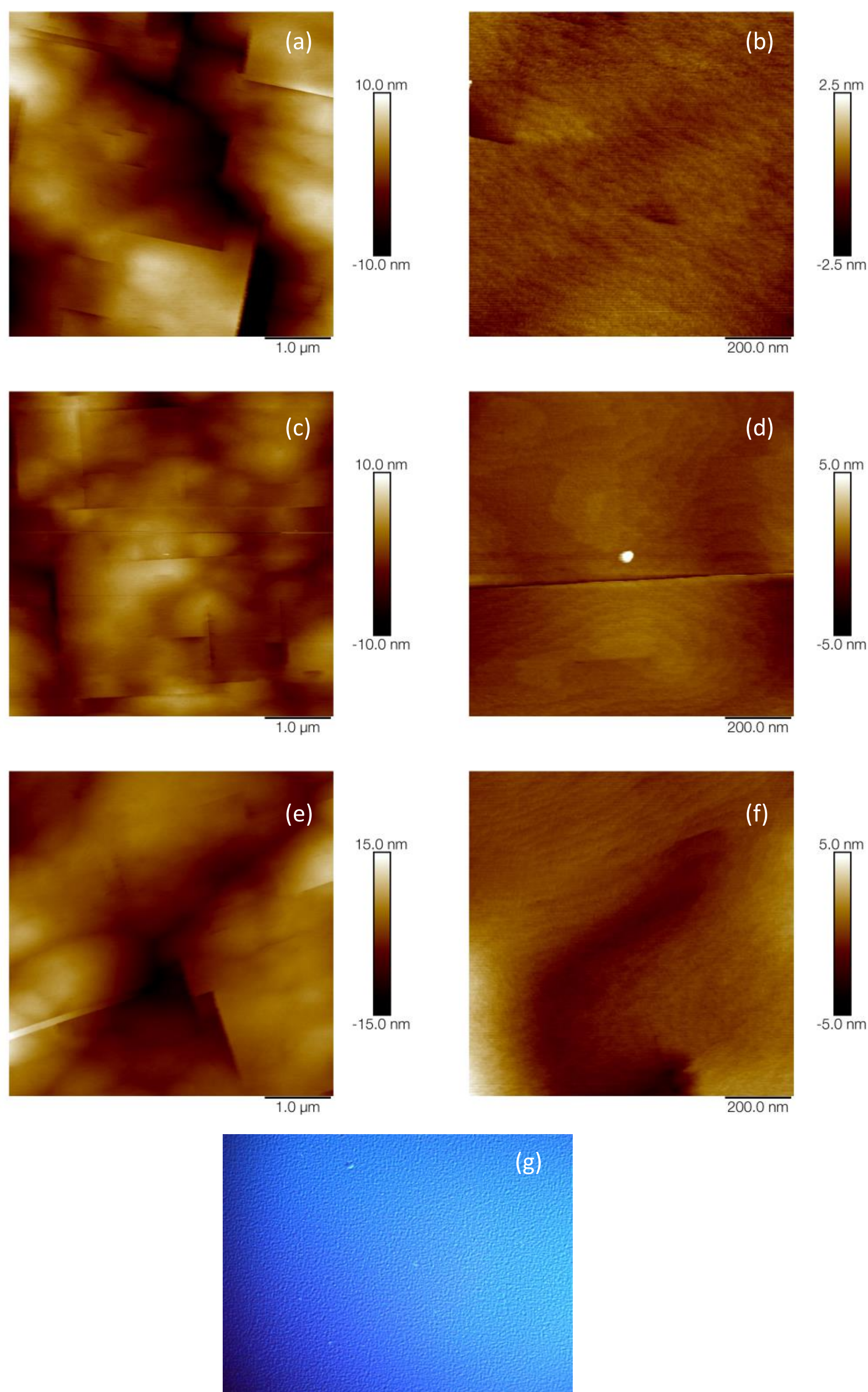

Figure 5.2. AFM images of the as-grown GaInAs TPV cells from the centre (a,b), middle (c,d) and the edge (e,f) of the wafer, (a,c,e) are 5µm × 5µm and (b,d,f) are 1µm × 1µm. The scale on the right indicates the roughness of the samples. Optical microscope image of the centre part of the sample (g).

Figure 5.2 (a)-(f) shows AFM images of different parts of the wafer. From the scale bars it can be observed that on micro-scale the roughness of the sample is very low, 5 nm in the centre to 10 nm on the edge for 1μm × 1μm measurements and 20 to 30 nm for 5μm × 5μm. The RMS roughness was calculated to be less than 1 nm for all 1 μm^2 images indicating a very good surface morphology of the analysed samples. However, an image taken by a camera on an optical microscope, Figure 5.2(g), shows an orange-skin-like roughness of the surface of the sample, which indicates than on macro-scale the morphology of the sample is not as good as suggested by the AFM. The origin of this effect is most probably the stress built-up within the sample.

5.2.2 Crystal Quality

One of the most effective methods of investigating the crystal quality of the materials is TEM. It can show a cross-section of the whole structure of the cell and hence is a useful tool to observe defects, strain, threading dislocations etc. TEM pictures taken for as-grown GaInAs cells described in the earlier sections of this chapter are shown in Figure 5.3.

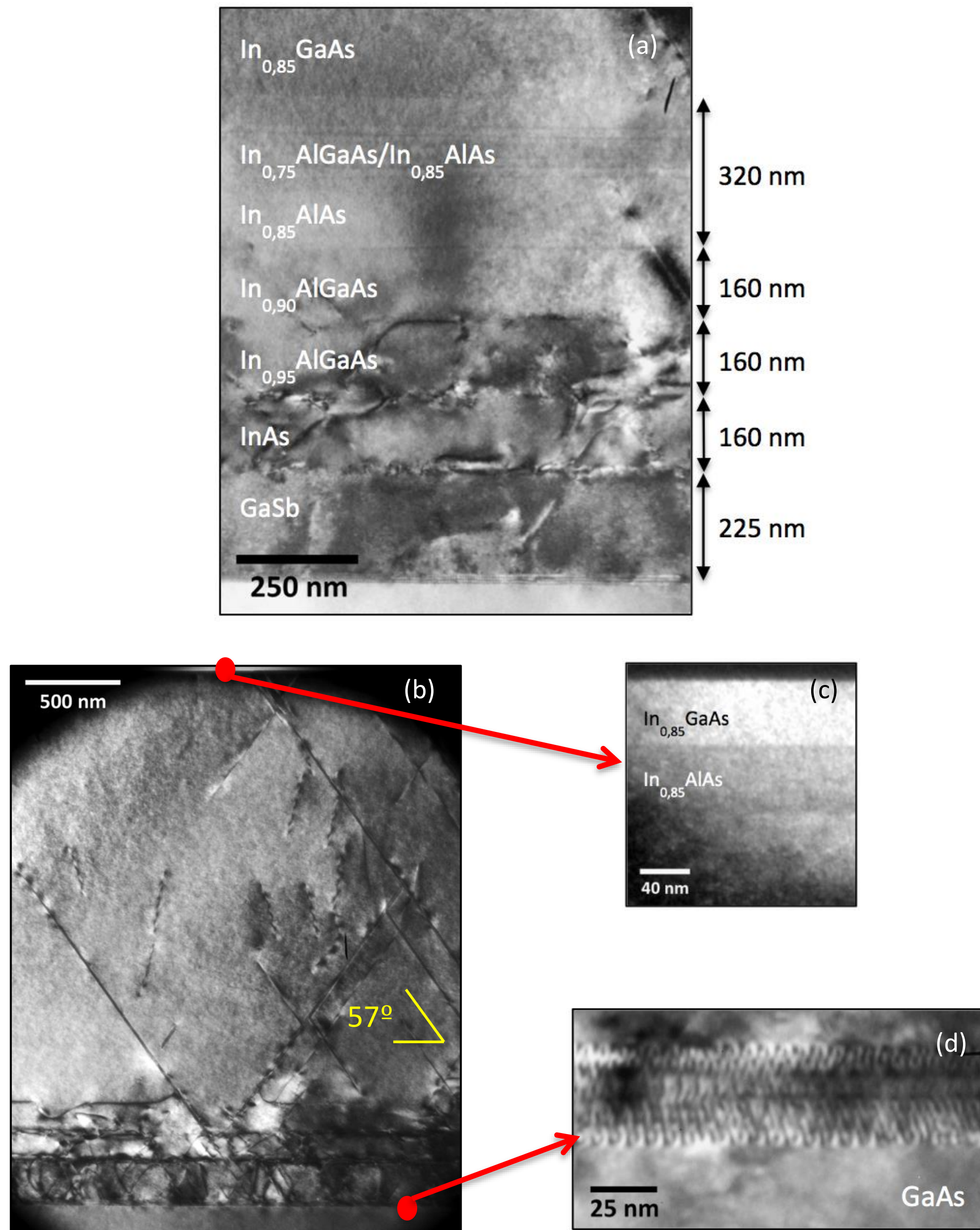

Figure 5.3. TEM images of the GaInAs cells showing the layers within the structure (a), a cross-section including the threading dislocations (b), micrograph of the top layers (c) and the network of misfit dislocations from which threading dislocations originate (d).

Figure 5.3 (a) shows a cross section across all the filtering layers and the lower part of the active layers. It can be seen that most of the threading dislocations (TDs) are confined to the three bottom layers, GaSb, InAs and $In_{0.95}AlGaAs$. Looking at the

picture of the whole structure from the substrate to the top contacting layer, Figure 5.3 (b), it can be observed that there are some threading dislocations propagating through the upper layers of the cell as well. However, the density of the threading dislocations in the active area of the cell is significantly lower than in the bottom filtering layers. It results in virtually perfect crystal quality in the uppermost layers of the cell, as shown in Figure 5.3 (c).

The threading dislocations (TDs) originate from misfit defects at the interface between the substrate and the GaSb filtering layer. The crosshatched pattern of these dislocations can be seen in the TEM micrograph in Figure 5.3 (d). They arise from lattice mismatch between the GaAs substrate and the subsequent layers grown on top of it [2]. Difference in lattice constants forces the grown material to try to fit into the crystal template of the substrate resulting in build-up of strain in the epitaxial layer. When the strain reaches a critical point, it is released by a formation of these misfit dislocations and the material relaxes. The more layers are grown, higher the stress on the bottom layers and hence more dislocations are formed at the interface with the substrate. Some of the stress will also be released by formation of threading dislocations originating at the substrate/cell interface. Introducing filtering layers helps to limit these dislocations to the bottom part of the cell and hence not affect the quality of the active layers. They act as a buffer between the substrate lattice constant and the cell material lattice constant, with the top layer of the buffer forming a virtual substrate for the active area growth. Since there is minimal mismatch between that virtual substrate and the p-i-n layers, there is no stress build-up between them and

hence only very few dislocations are formed. Use of effective filtering layers for the cells presented in this chapter ensures high quality of the produced devices.

During the calibration growths of the buffer layers for the samples presented in this chapter we have discovered that using low amounts of Be dopant during the growth helps to significantly reduce the number of threading dislocations [3]. The misfit dislocations (MDs) created at the interface between two materials with large lattice mismatch, in this case GaSb on GaAs, come in two variants, 60° MDs and 90° MDs. The first type generates threading dislocations whilst the second one can completely relax the system without formation of any TDs. Therefore it is crucial to first understand conditions under which the two types are formed and then apply this knowledge to grow defect-free materials. It is well known that formation of one or the other type of MDs depends on the temperature of growth, with 60° MDs being formed at higher temperatures (540°C and above) and 90° MDs at low temperatures (below 520°C). It has also been observed that formation of 90° MDs can be aided by use of low levels of dopants that influence the surface dynamics during the growth in a favourable way.

In order to assess the impact of use of Be doping on the crystal quality of grown GaSb two samples have been grown on GaAs(001) substrates: an undoped GaSb (sample A) and a Be-doped one with doping levels of $5\times10^{18}cm^{-3}$ (sample B). Figure 5.4 shows the schematics of GaSb growth and formation of the two different types of the MDs in both undoped and Be-doped GaSb samples. The whole process can be described in four steps.

Step 1: The initial growth of GASb on GaAs following the Volmer-Weber (island) growth mode. Islands are formed in order to release the strain arising from large lattice mismatch (7.8%). The islands are of uniform height, flat-topped and confined by <111> planes. The initial strain relief comes through formation of an interfacial misfit array consisting of pure 90° MDs along the <110> directions at the GaSb/GaAs interface (Fig. 5.4. (a)).

Step 2: More GASb is deposited and the islands reach a critical height where the strain is partially relieved by bending the atomic planes to the free surface under the leading edges. This results in formation of 60° MDs at the leading edges of each island (Fig. 5.4. (b)).

Step 3: After the deposition thickness exceeds 80 nm the islands start to coalesce causing an interaction between the 60° MDs at each leading edge and the previously formed 90° MDs leading to generation of TDs. As the upper parts of the islands start to coalesce new 60° MDs are formed at the coalescence areas. These new 60° MDs glide down to the GaSb/GaAs interface along the <111> planes, where they interact with the 90° MDs producing more threading dislocations (Fig. 5.4. (c) Step 3.1.). Formation of the new TDs can be prevented if Be doping is used. The presence of Be atoms causes lattice distortions which pin the 60° MDs formed at the coalescence areas limiting the dislocation mobility (Be hardening process) (Fig. 5.4. (c) Step 3.2.). This prevents the 60° MDs from gliding towards the 90° MDs and hence no new TDs are formed.

Step 4: Continued growth of the samples in layer-by-layer mode. Fig. 5.4. (d)

shows the final distribution of the dislocations within a sample with (Step 4.2) and without (Step 4.1) Be doping.

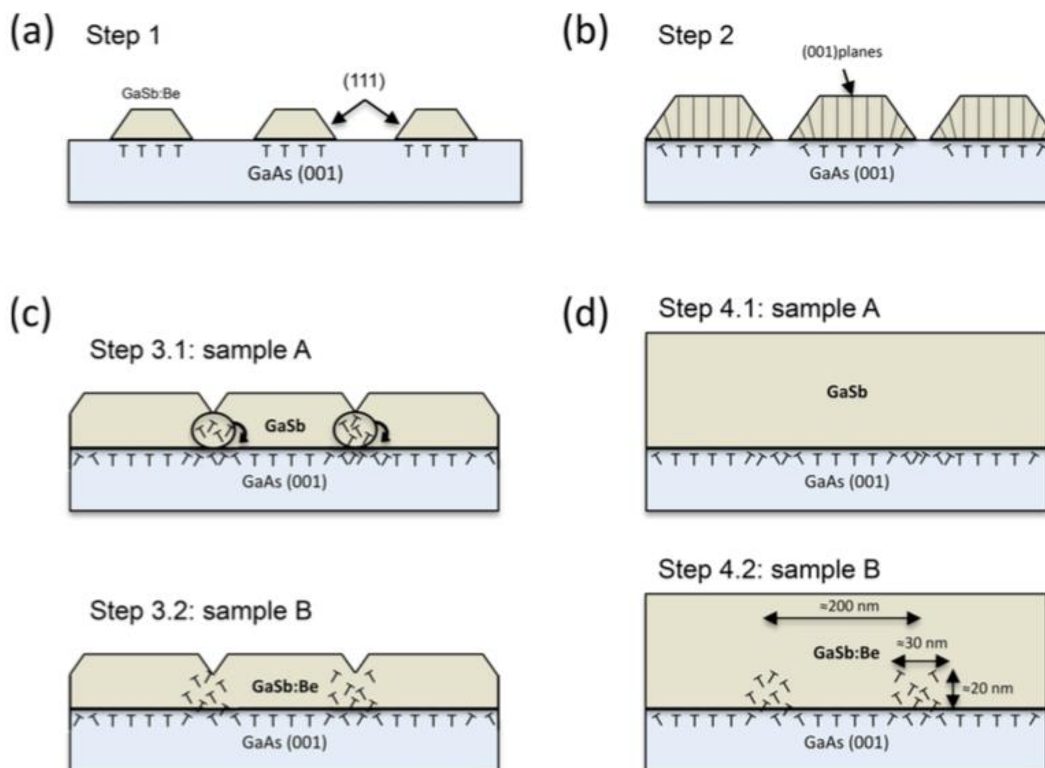

Figure 5.4. Schematic representation of MD formation and distribution on the GaSb:Be/GaAs heterostructure. (a) Step 1: initial islands following the Volmer-Weber growth model. (b) Step 2: Strain relaxation by IMF network (>) and 60° MDs at the leading edges (h). (c) Step 3: Distribution of the 60° MDs originated in the coalescence areas for both samples. (d) Step 4: Final distribution of 90° and 60° MDs in the GaSb(:Be)/GaAs system.

Figure 5.5 compares the resulting crystal quality of samples A and B. The TEM images of the two samples clearly show that number of threading dislocations is considerably reduces when Be is used as a dopant during the buffer growth. In same-sized sections of the two samples we can observe 12 TDs in the GaSb sample

(sample A) and only 3 in the GaSb:Be one (sample B). From the dimensions of the micrographs (TEM images) and the sample slice used in the measurements the TDs density can be calculated as 6.7×10^{-4}nm^{-2} and 2.3×10^{-4}nm^{-2} for samples A and B, respectively.

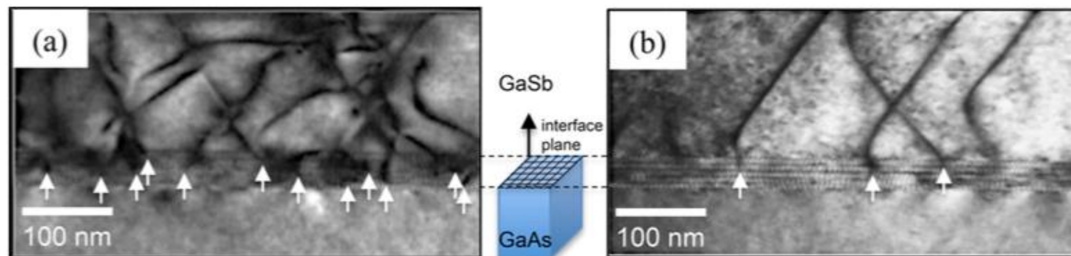

Figure 5.5. Cross-sectional TEM micrographs at the interface of (a) GaSb/GaAs (sample A) and (b) GaSb:Be/GaAs (sample B). Both micrographs have been taken with the same sample thickness, magnification and angle. The <001> plane at the GaSb/GaAs interface is schematically shown in between the two micrographs to help visualise the MD configuration. The white arrows indicate the origin points of the TDs.

5.2.3 Composition

Non-invasive methods are preferred when assessing the composition of the grown materials. Two of such methods that have been used for the cells grown for this project are XRD and PL. They provide information on how close to the original design the grown materials are. Figure 5.6 shows the results of XRD measurements of the sample presented in this chapter.

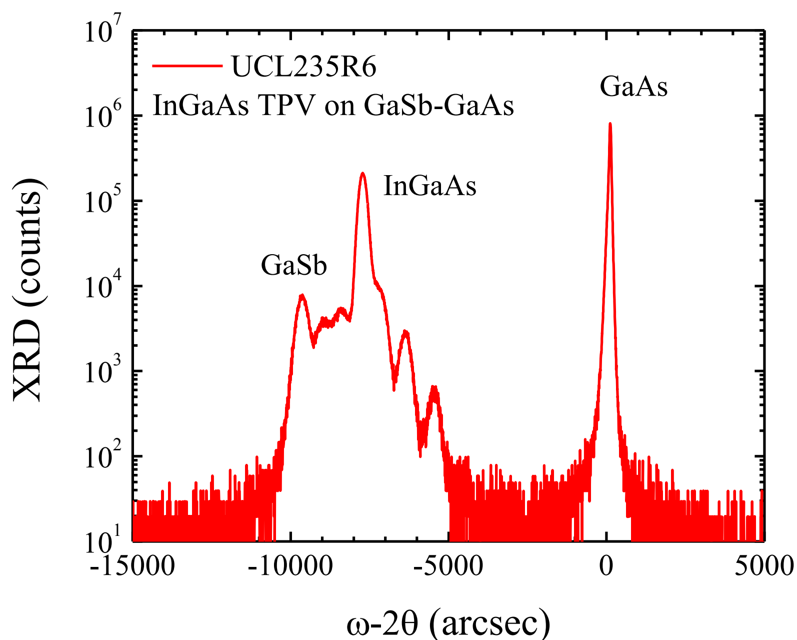

Figure 5.6. XRD composition measurement results for the GaInAs TPV cell grown on GaAs substrate with GaSb, InAs and metamorphic buffer layers.

Different peaks correspond to different materials and their different compositions, as indicated on the plot. The GaAs substrate, GaSb buffer and InGaAs cell peaks are clearly distinguishable, however there are several other peaks there as well. They most probably arise from the other filtering layers within the structure. The highest InGaAs peak corresponds to In/Ga ratio of 0.877/0.123 as opposed to the planned 0.85/0.15. However this is not a large deviation and it could be due to errors in calibration of the XRD system or small changes in the growth conditions in the MBE between the calibration and the sample growths.

Another method of estimating the composition of the grown materials is via PL measurements from which the bandgap can be inferred. The sample has been cooled

down to 4 K for the measurements in order to eliminate interference from thermal effects as explained in section 3.3.1 of this thesis.

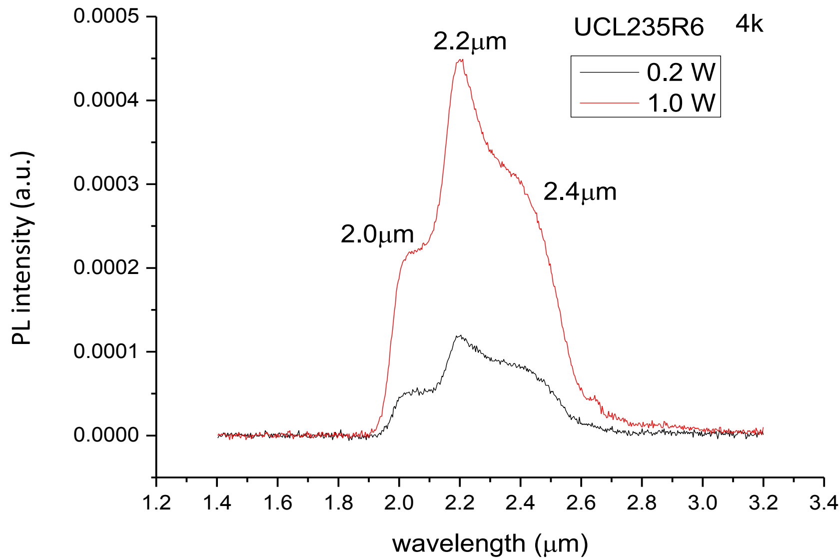

Figure 5.7. The results of the low-temperature photoluminescence measurements of the GaInAs TPV cell.

The low-temperature PL results, Figure 5.7, show three peaks of different intensities at 2.0, 2.2 and 2.4 μm suggesting three different In/Ga compositions within the sample. GaInAs with 85% indium should emit around 2.36 μm at 4 K, while the 2.2 μm peak corresponds to $In_{0.8}Ga_{0.2}As$ and 2.0μm peak to $In_{0.735}Ga_{0.265}As$. The discrepancies between the XRD and PL measurements imply that the material composition of the grown cells is not uniform.

5.3 Fabrication Process

After the material quality measurements it was decided that the grown structure should be fabricated into TPV devices. A sample has been cleaved from the centre of as-grown wafer to ensure best material uniformity. Both top-top and top-bottom approaches were used for contacts fabrication in order to investigate any possible differences in performances of the cells due to different contacting methods. After the sample has been cleaned and deoxidised (details in section 3.2), it has loaded to a bell jar evaporator for back contact deposition. 5 nm of Au has been evaporated, followed by 10 nm of Zn and 150 nm of Au, and then annealed at 340°C for 7 seconds to improve adhesion. Then the sample was cleaved into two parts, one of them to be used for top-top and the other one for top-bottom contacts. Fabrication of top-contacted devices requires several steps. First, the mesa pattern has to be defined with photolithography and then etched in order to separate the devices and to reach the lower contacting layer. Hydrogen peroxide 35%: phosphoric acid 85%: H2O 1:1:10 solution has been used to etch about 1.4-μm-deep mesas. Afterwards the sample was soaked in an acetone bath to remove the photoresist. Optical microscope has been used to evaluate the features and Dektak measurements were performed to check the etch depth is correct. Afterwards photolithography was used to create a mask for contacts deposition and the sample without mesa etch was taped onto a shadow mask. Both samples have then been loaded into the e-beam evaporator and 20 nm/200 nm Ti/Au contacts were deposited. The samples with photoresist mask have then been soaked overnight to achieve lift-off. All the details

of the processing steps mentioned in this section can be found in section 3.2 of this thesis. Figure 5.8 below shows the devices with contacts fabricated via photolithography (a) and shadow mask (b).

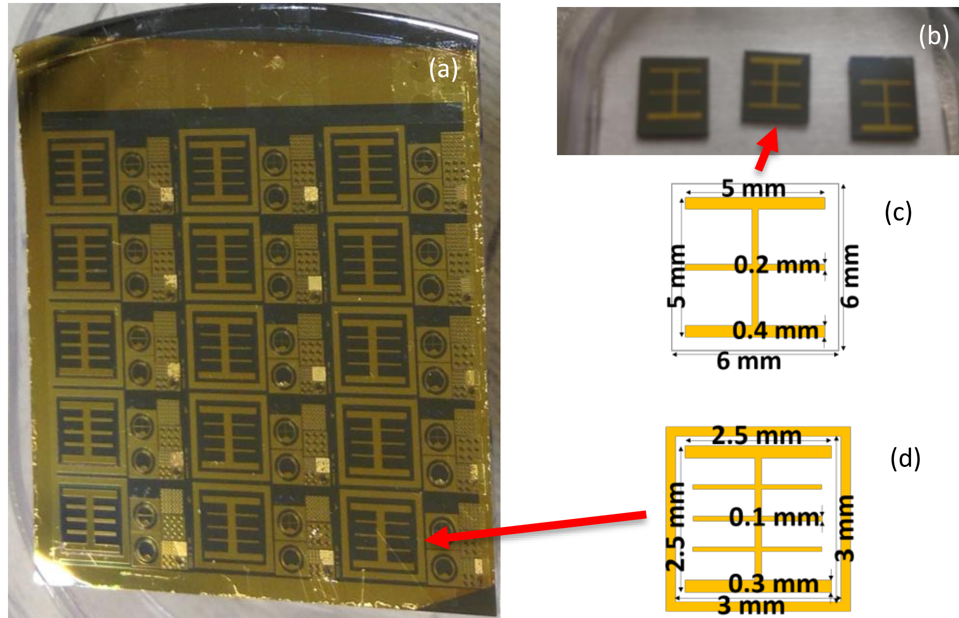

Figure 5.8. The fabricated devices after contacts deposition using (a) top-top approach with photolithography masking and (b) top-bottom approach with a shadow mask for top contacts. Schematics of the metal contacts and their dimensions for (c) the shadow mask and (d) the photolithography mask.

5.4 Electrical and Optical Characterisation

5.4.1 Dark JV Measurements

The first set of measurements performed for the fabricated samples were dark JV measurements, i.e. current and voltage measurements under no illumination. The solar simulator station has been used for this purpose. Figure 5.9 shows the resulting JV curves of all 15 devices presented in Figure 5.8 (a) in the previous section.

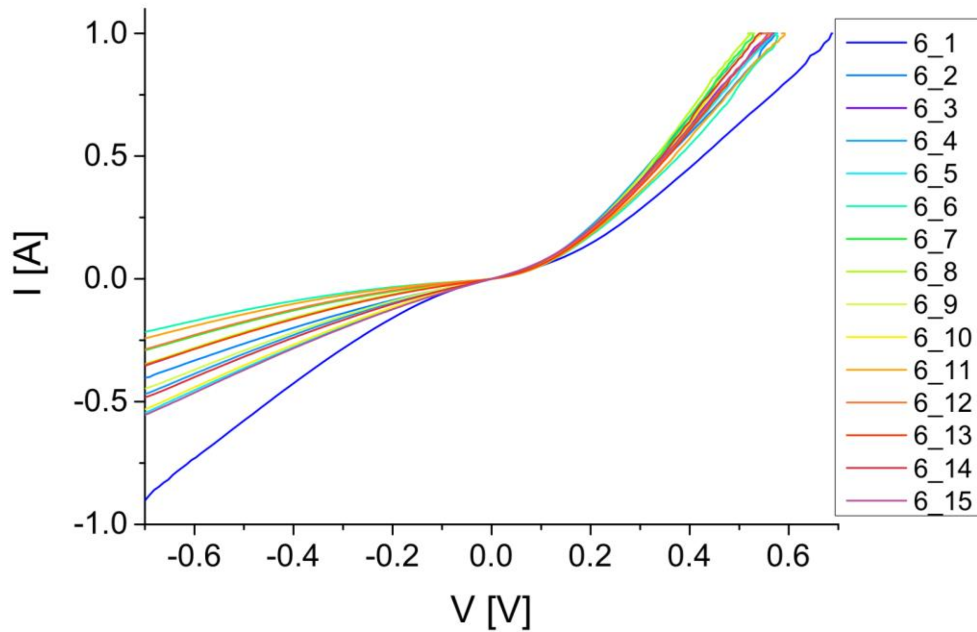

Figure 5.9. The pre-annealing dark JV measurements results of fifteen $In_{0.85}Ga_{0.15}As$ TPV cells.

The general trend of the curves is similar, diode behaviour has been observed for all the devices with forward currents being comparable but with larger differences in the reverse current. However, despite the curves having a general diode shape they are far off from the ideal diode curve, most likely due to high contacts resistance and material defect. Measurements of contacts resistance indicated that it is indeed higher than desired, about 60-70Ω, and they showed Shottky behaviour instead of ohmic. This had a negative effect on the performance of the cells hence not very good dark JV measurements results. In order to minimise the impact of the contacts resistance, the devices have been thermally annealed [4,5]. A range of temperatures and times, detailed in Figure 5.10, has been used. Best outcome has been achieved for devices annealed at 400 and 420°C for 30 seconds, resulting in significant

improvements in their dark JVs.

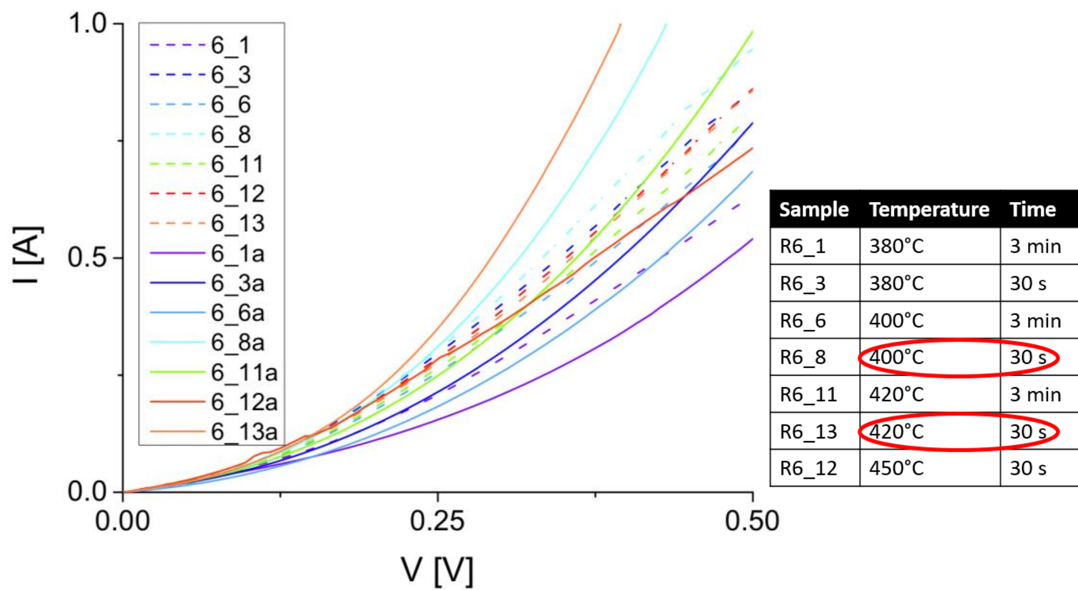

Sample	Temperature	Time
R6_1	380°C	3 min
R6_3	380°C	30 s
R6_6	400°C	3 min
R6_8	400°C	30 s
R6_11	420°C	3 min
R6_13	420°C	30 s
R6_12	450°C	30 s

Figure 5.10. The pre- (dashed lines) and post-annealing (continuous lines) dark JV measurements of some of the top-top contacted $In_{0.85}Ga_{0.15}As$ TPV cells. The table details the times and temperatures of the annealing process as well as which devices have been subjected to it.

In order to obtain more devices with improved performance, another batch of TPV cells has been fabricated from the $In_{0.85}Ga_{0.15}As$ sample. Same as in the former batch Ti(20nm)/Au(200nm) have been used for both the n and p type contacts. Dark JV measurements have been performed showing diode behaviour of all the devices. Consequently, all the contacts have been annealed at 420°C for 30 seconds in order to improve their quality.

Figure 5.11 shows the final dark JV results for the best top-top (blue lines) and best top-bottom (green lines) contacted devices compared to references with not

annealed contacts. It can be observed that while the reverse currents trends are comparable and only vary in values, the forward current trends differ. The top-top contacts devices have a later onset of diode behaviour but the curve is steeper, indicating that for higher bias voltages performances of the top-top devices will surpass those of the top-bottom ones. Comparing curves in Figure 5.11 it can be noticed that this change in behaviour is more prominent after the contacts have been annealed, suggesting some impact of the RTA process on the devices, but it can also be observed for the not annealed references (grey and black curves in Figure 5.11).

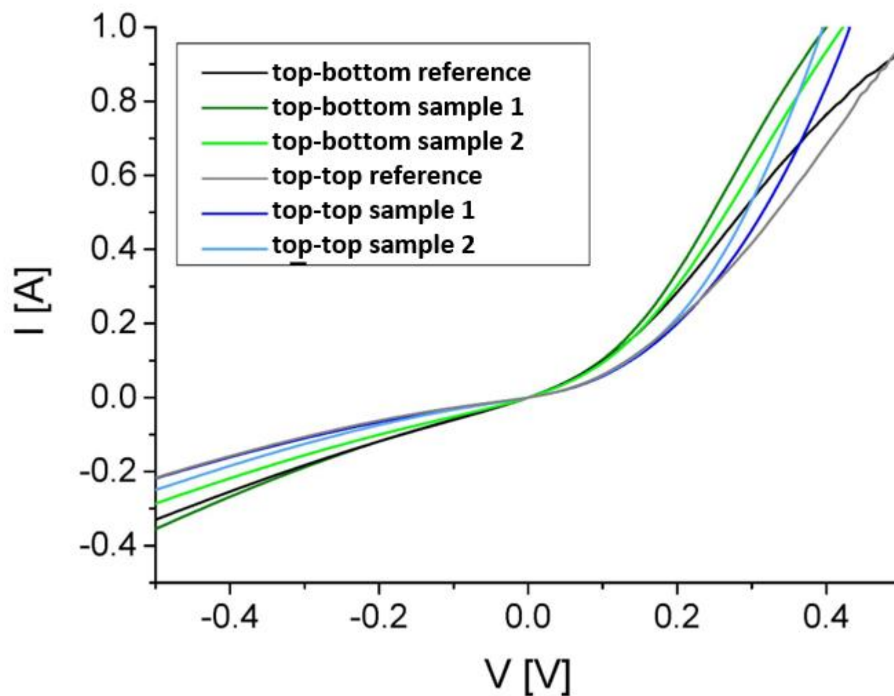

Figure 5.11. The dark IV measurements of the $In_{0.85}Ga_{0.15}As$ TPV cells processed using top-top contacts (blue lines) and using top-bottom contacts (green lines) compared to their respective references with not annealed contacts (grey and black lines).

The difference in behaviour between devices with different types of contacts is most likely due to the fact that in the top-top devices the carriers do not need to pass through the defective buffer layers. The difference between the annealed and not annealed samples is in majority caused by the reduction of contacts resistance of the RTA treated samples.

5.4.2 Illuminated JV and QE

After confirming that the fabricated devices exhibit diode behaviour, the samples have been sent to the ARL to measure the JV characteristics under blackbody illumination [6]. One of the smallest devices has been used for these measurements, the size of the mesa is 53 μm in diameter. Figure 5.12 shows results of dark JV measurements at room temperature and at 78 K. The open circuit voltage has been estimated to be only -0.0036 V and the short circuit current is 0.346 A/cm2. The measured dark currents were high which is an indicator of low shunt resistance in forward bias. As can be observed from the curves for reverse bias, the breakdown voltage is low at room temperature but it increases when the temperature of the device is lowered. Reason for high series resistance most probably comes from the fabrication processes, especially metallisation. As mentioned previously, the contacts did not show a good ohmic behaviour, even after thermal annealing.

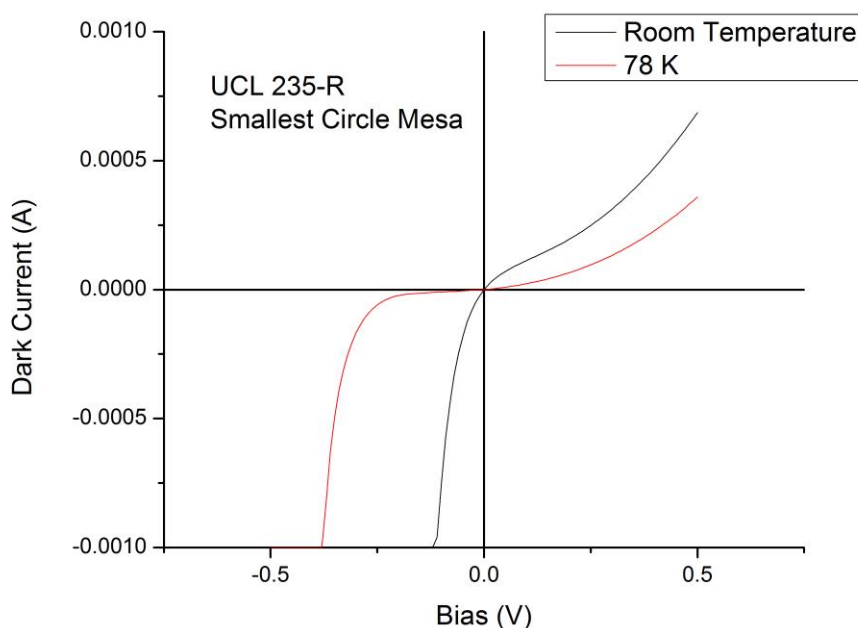

Figure 5.12. The dark current measurements for a range of bias voltages for the $In_{0.85}Ga_{0.15}As$ cells at room temperature (black line) and at 78 K (red line).

In order to assess the performance of the $In_{0.85}Ga_{0.15}As$ TPV cells under normal operating conditions, JV measurements have been performed under a wide-open aperture of a 1000°C blackbody source. Results of these measurements compared to room temperature dark JV are shown in Figure 5.13.

Looking at the values on the current axis, it can be observed that the difference in measured current with and without the blackbody illumination is very small. The dark current at room temperature is much higher than the photocurrent so the two can hardly be resolved. In order to have a better indication of photocurrent it would be useful to perform the measurements at low temperature since the dark current is then much lower, as shown in Figure 5.12. The setup used for these measurements does not have such capabilities therefore the total current at low temperature under

blackbody source has been inferred by adding the room temperature photocurrent to low temperature dark current. The resulting current values should be close to the true ones since there is no reason for the photocurrent at low temperature to differ from the room temperature measurement. Figure 5.14 shows the low and room temperature I-V curves in the dark and under a 1000°C blackbody source.

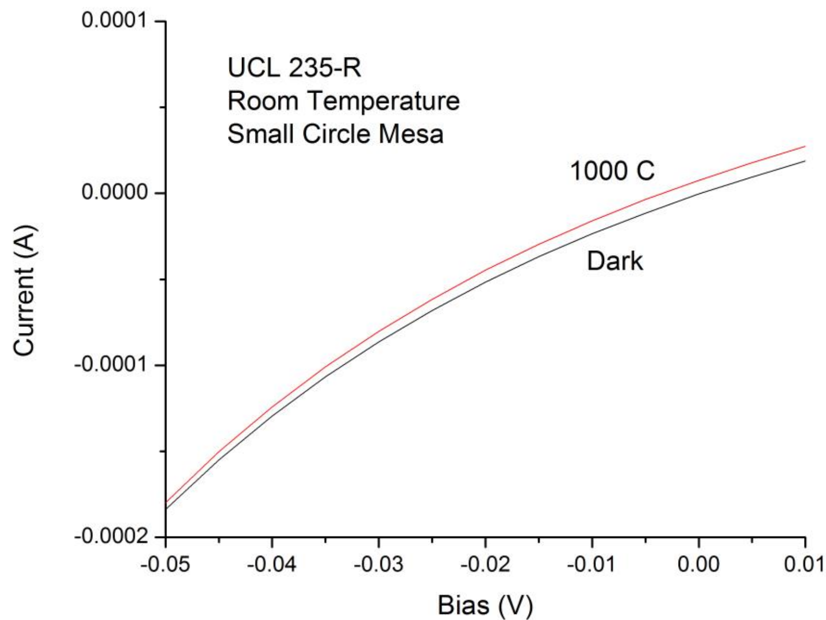

Figure 5.13. The current measurements for a range of bias voltages for the $In_{0.85}Ga_{0.15}As$ cells at room temperature under a 1000°C blackbody source (red line) and in the dark (black line).

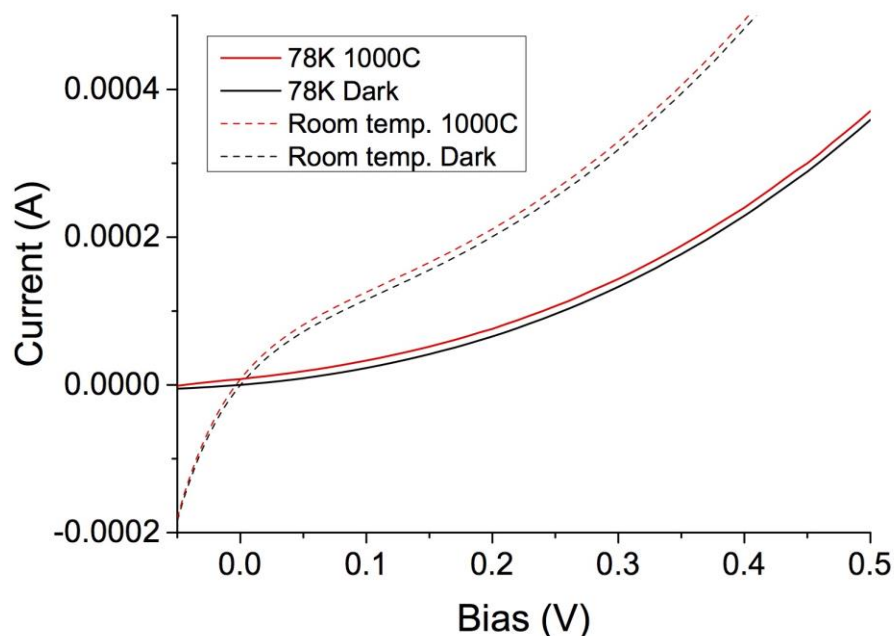

Figure 5.14. The current measurements for a range of bias voltages for the $In_{0.85}Ga_{0.15}As$ cells at room temperature under a 1000°C blackbody source (red dashed line) and in the dark (black dashed line), low temperature dark current measurement (solid black line) and calculated values for low temperature current under 1000°C blackbody source (red solid line).

It can be observed that for lower bias voltages the difference between illuminated and dark currents is greater for low temperature measurements. This is to be expected since the dark current is lower and it rises significantly slower than at room temperature while photocurrent generation remains the same. For voltages above 0.1 V the difference becomes comparable for the 78 K and RT measurements.

Figure 5.15 shows the results of quantum efficiency (electrons/photon) and responsivity (A/W) fof the $In_{0.85}Ga_{0.15}As$ TPV cells investigated. The relative spectral response in the Fourier Transform Infrared Spectroscopy (FTIR) and the photocurrent

in a narrow spectral band around 2 μm have been measured using a calibrated blackbody source at 1000°C with three different aperture sizes. The slope of the current versus photon flux for the different apertures gives the average quantum efficiency at 2 μm. This was used to scale the relative spectral data to obtain the efficiency in electrons per photon and responsivity in amps per watt. From the quantum efficiency measurements, the responsivity of the device can be calculated using the following equation[7]:

$$R(\lambda) = \eta(\lambda)\frac{q}{hf} = \eta(\lambda)\frac{\lambda}{1.23985}\ [\frac{A}{W}] \tag{5-1}$$

where η is the quantum efficiency at a given wavelength, q is electron charge, h is Planck's constant, f is the frequency of the optical signal and λ is the wavelength of the signal.

As can be seen from the plots in Figure 5.15, quantum efficiencies up to 50% were obtain which is a good result. These measurements show that the devices can be successfully operated as photodetectors despite high series resistances observed from the I-V measurements. All the quantum efficiency related measurements have been carried at low temperatures (78 K).

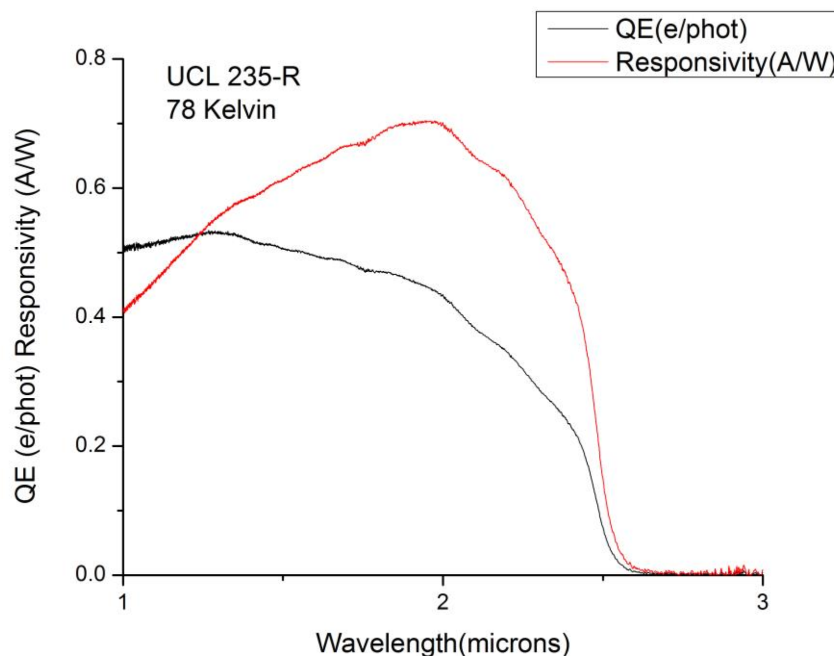

Figure 5.15. The quantum efficiency (electrons/photon, black line) and responsivity (A/W, red line) measurements for a range of wavelengths for the $In_{0.85}Ga_{0.15}As$ cells at 78 K under a 1000°C blackbody source.

5.4.3 PL of Annealed Samples

High-temperature annealing study has been performed on the grown structures and its effects investigated using PL measurements. More details on how annealing works and how it affects the samples can be found in section 3.2.5. A range of temperatures from 700 to 800°C have been used and durations of 150 and 300 seconds. The results of the PL measurements compared to an unannealed reference sample are shown in Figure 5.16. The table next to the plot details what annealing conditions have been used for which sample. All the measurements have been performed at 20 K with the laser power set to 1W (effective power delivered to the

sample was approximately 100mW).

A clear improvement can be observed for all the annealed samples compared to the as-grown reference. The best results have been measured for a sample annealed at 725°C for 300 s for which the peak PL intensity has increased about six times. Generally higher improvement in photoluminescence has been measured for longer duration of the thermal processing compared to the shorter ones at the same temperature. Raising the annealing temperature above 725°C does not further improve the results. Behavior of the sample annealed at 800°C for 300 seconds does not fit to the patterns observed for all the other samples. While the peak at 3.5 μm is a second order peak and can be ignored, the origins of short wavelength peak as well as increase in PL intensity compared to the sample annealed at 750°C for the same duration remain unknown.

More details about the impact of different annealing times and temperatures can be obtained from the plots (b) and (c) in Figure 5.16. For annealing duration of 150 seconds increase in temperature results in further increase in the PL intensity of the measured samples. However, when the samples are annealed for 300 seconds 725°C gives optimum result and 300s at 750°C is already too much. Too high temperature and too long annealing time can lead to intermixing of atoms and migration of dopants leading to blurred interfaces and changes in layers compositions and doping profiles. These in turn result in worse performance of the sample.

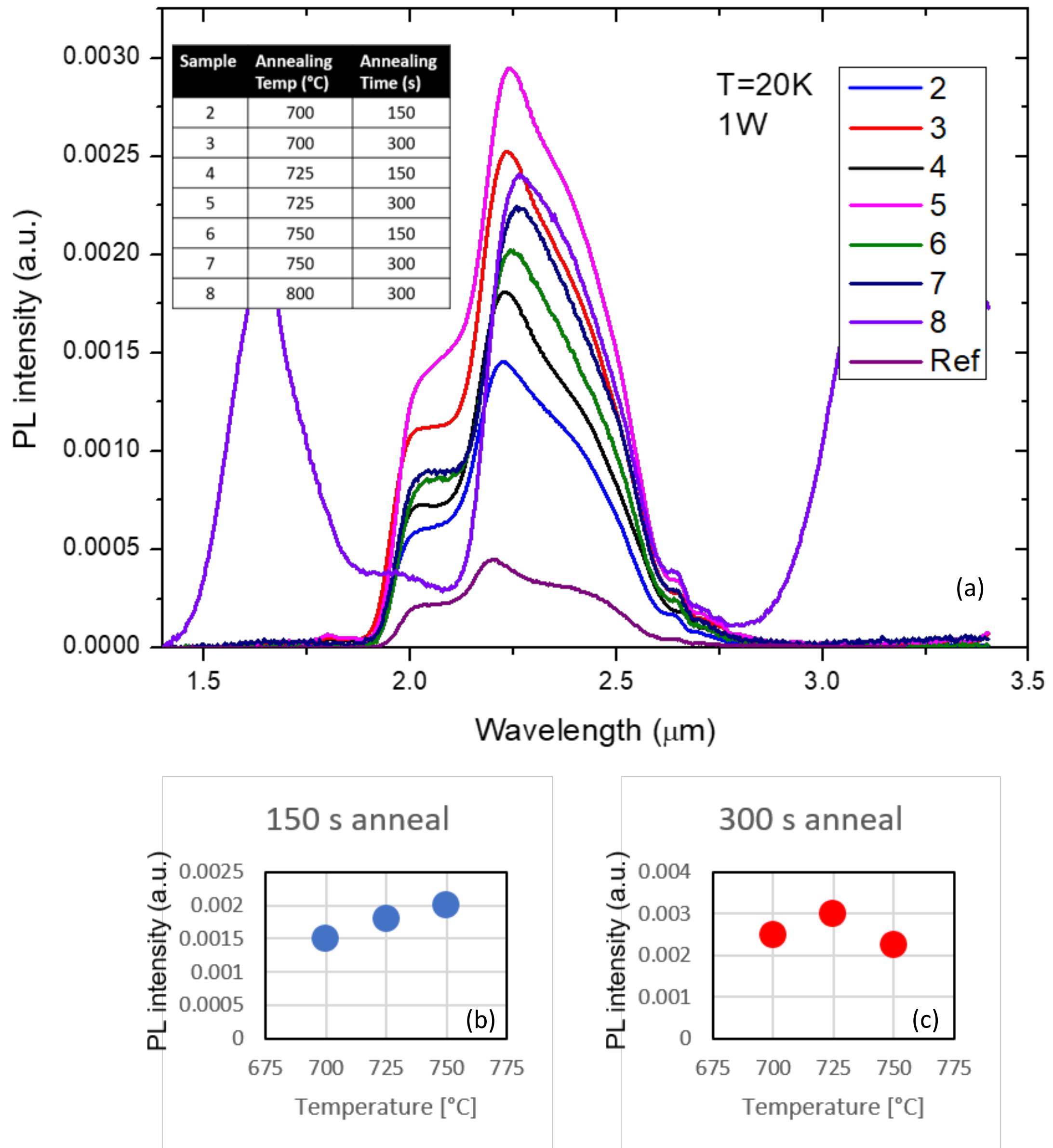

Sample	Annealing Temp (°C)	Annealing Time (s)
2	700	150
3	700	300
4	725	150
5	725	300
6	750	150
7	750	300
8	800	300

Figure 5.16. (a) The photoluminescence measurements for the $In_{0.85}Ga_{0.15}As$ samples annealed at different conditions (detailed in the table) compared to the unannealed reference sample. The two small plots show trends for the two different annealing durations: (b) 150s (samples 2,4,6) and (c) 300s (samples 3,5,7).

5.5 Conclusions

In conclusion, we have successfully grown InGaAs TPV cells by MBE on GaAs substrate, evaluated the material quality, fabricated InGaAs TPV cells and measured their performances. Good material quality was confirmed by low threading dislocation density and smooth surface morphology observed with AFM. The composition measurements have implied that the samples are not uniform, with gallium content ranging from 12.3 to 26.5%.

The MBE grown samples have then been fabricated into TPV devices using LCN (London Centre for Nanotechnology) facilities. Two contacting methods have been used, a top-top one utilising photolithography processes and a simple top-bottom one using a shadow mask for the top contact. Differences between the performances of the devices fabricated using these two approaches have been observed however the origin of those have not yet been investigated. The performances of the TPVs have been improved by thermal annealing of the metal contacts at 420°C for 30 seconds.

The diode behaviour of the devices has been confirmed with dark JV measurements at 78 K as well as room temperature. Generation of photocurrent has also been observed from JV measurements under a 1000°C blackbody source, however the total current measured consists mostly of the dark current. These results show that the fabricated devices would not work well as TPVs due to high levels of dark current and only low-temperature operation. Most likely reasons behind the poor TPV performance are high levels of Auger recombination, intrinsic to low bandgap materials, as well as low material quality and possibly fabrication errors.

High-temperature rapid thermal annealing (RTA) study showed that the photoluminescence of the devices and hence possibly their performances can be significantly increased using this method. However, improving the crystal quality via RTA is not sufficient to turn these devices into high-quality TPVs.

After establishing that the fabricated devices are not suitable for TPV operation, further characterization was performed in order to determine if they could be used for other mid-IR applications. The QE and responsivity measurements showed that the performance of the devices is good, yielding about 50% efficiency in converting photons into electrons. Because of good quantum efficiency results the fabricated devices can be used as mid-IR photodetectors. Their performance in such capacity has been evaluated at the ARL with temperature-dependent dark current as well as voltage-dependent and temperature-dependent photoresponse/QE measurements. A paper detailing these findings has been published [8].

5.6 References

1. P. Jurczak, A. Onno. K. Sablon, and H. Liu, Efficiency of GaInAs thermophotovoltaic cells: the effects of incident radiation, light trapping and recombinations, *Optics Express 23(19)*, 2015.
2. R.F.C. Farrow, Molecular Beam Epitaxy – Applications to Key Materials, *William Andrew Publishing/Noyes*, 1995.
3. M. Gutiérrez, D. Araujo, P. Jurczak, J. Wu and H. Liu, Solid solution strengthening in GaSb/GaAs: A mode to reduce the TD density through Be-doping, *Applied Physics Letters 110*, 092103, 2017.
4. H. Kim, S. Han, T. Seong, and W. Choi, Electrical and Structural Properties of Ti/Au Ohmic contacts to n ZnO, *Journal of the Electrochemical Society 148(3)*, 2001.
5. A. Redondo-Cubero, M.D. Ynsa, M.F. Romero, L.C. Alves, and E. Munoz, Effect of rapid thermal annealing on the composition of Au/Ti/Al/Ti contacts for GaN-based microdevices, *Nuclear Instr. and Methods in Physics Research Sec. B 306*, 2013.
6. M. Tan *et al.*, Investigation of InGaAs thermophotovoltaic cells under blackbody radiation, *Appl. Phys. Ex. 7(9),* 2014.
7. K.W. Busch and M.A. Busch, Multielement Detection Systems for Spectrochemical Analysis, *John Willey and Sons*, 1990.
8. P. Jurczak, K. Sablon, M. Gutiérrez, H. Liu and J. Wu, 2.5-μm InGaAs photodiodes grown on GaAs substrates by interfacial misfit array technique,

Infrared Physics & Technology, Volume 81, Pages 320-324, 2017.

9. G. Binnig, C.F. Quate, and Ch. Gerber, Atomic Force Microscopy, *Physical Review Letters 56*, 1986.
10. G. Binnig, and H. Rohrer, Scanning tunneling microscopy, *IBM Journal of Research and Development* 30(4), 1986.
11. B.D. Cullity, Elements of X-ray diffraction, *2nd ed. Addison-Wesley, Reading, Mass.,* 1978.
12. H. Haug, and S.W. Koch, Quantum Theory of the Optical and Electronic Properties of Semiconductors (5th ed.), *World Scientific*, 2009.

Chapter 6:

InAs Nanowires for Thermophotovoltaic Applications

This chapter contains details on growth and optical analysis of InAs nanowires as a low-bandgap material suitable for thermophotovoltaic applications. Description of calibration growths for high-quality InAs nanowires is followed by identification of main challenges for using InAs nanowires for high-performance optoelectronic and photonic devices. A solution to these key problems is presented further in the chapter and its suitability verified by detailed analysis of the photoluminescence spectra.

6.1. Motivation and Initial Growths

The motivation behind choosing InAs nanowires (NWs) as the next TPV-suitable material was discovery of crippling limitations of InGaAs bulk described in the previous chapter. Despite the possibility of significant improvements in crystal quality through annealing, defects due to lattice mismatch between the active material and the substrate are virtually impossible to avoid. Hence, growth of low defect density InGaAs cannot be facilitated on low cost substrates such as silicon. Moreover, the high levels of Auger recombination in low bandgap materials cannot be suppressed leading to high levels of dark current in the fabricated devices. These observations lead us to conclude that InGaAs bulk is not a suitable choice for high-performance and low-cost TPV devices. Therefore, a new low-bandgap material free of the aforementioned limitations needs to be developed. Since large lattice constant mismatch with silicon as well as high levels of Auger recombination rates are intrinsic to all low-bandgap III-V bulk semiconductors, another geometry should be considered. Nanowires were chosen for this project since they can be grown on virtually any substrate due to the small contact area between the NWs and the substrate limiting the defects to the interface between the two materials. Moreover, the small dimensions of the nanowires lead to 2D carrier confinement which can effectively reduce the Auger recombination rates. The large surface area and arrayed geometry can significantly improve the absorption as well as cooling efficiency. Due to these advantages InAs nanowires were chosen as the next material to be researched for TPV applications in this thesis and the details of its development are presented in this

chapter.

The first step to high-performance InAs nanowires (NWs) based optoelectronic and photonic devices is reproducible growth of high-quality, high density and high uniformity InAs NWs on a cheap, industry-relevant platform such as i.e. silicon wafers. High-quality InAs NWs have been demonstrated using gold catalyst particles[1-10], but these are not compatible with complimentary metal-oxide-semiconductor (CMOS) industrial standards. Self-catalysed growth methods are therefore more suitable and have been successfully used before[5,11-13], however they require fine levels of deposition control to obtain high quality material. Such high levels of precision can be achieved using a molecular beam epitaxy (MBE) system like the one described in section 3.1.1 of this thesis.

Nanowires are very sensitive to growth conditions such as substrate temperature, ratio of the V/III fluxes, substrate preparation. Even very minute changes like a few degrees too low or too high substrate temperature can severely hinder or even completely prevent nanowire formation[14-15]. Therefore many calibration growths are required where the growth conditions are successively adjusted in order to obtain the best quality of the final material. SEM images of some early InAs NWs samples are presented in Figure 6.1 showing the progression in enhancing the quality and uniformity of the nanowires.

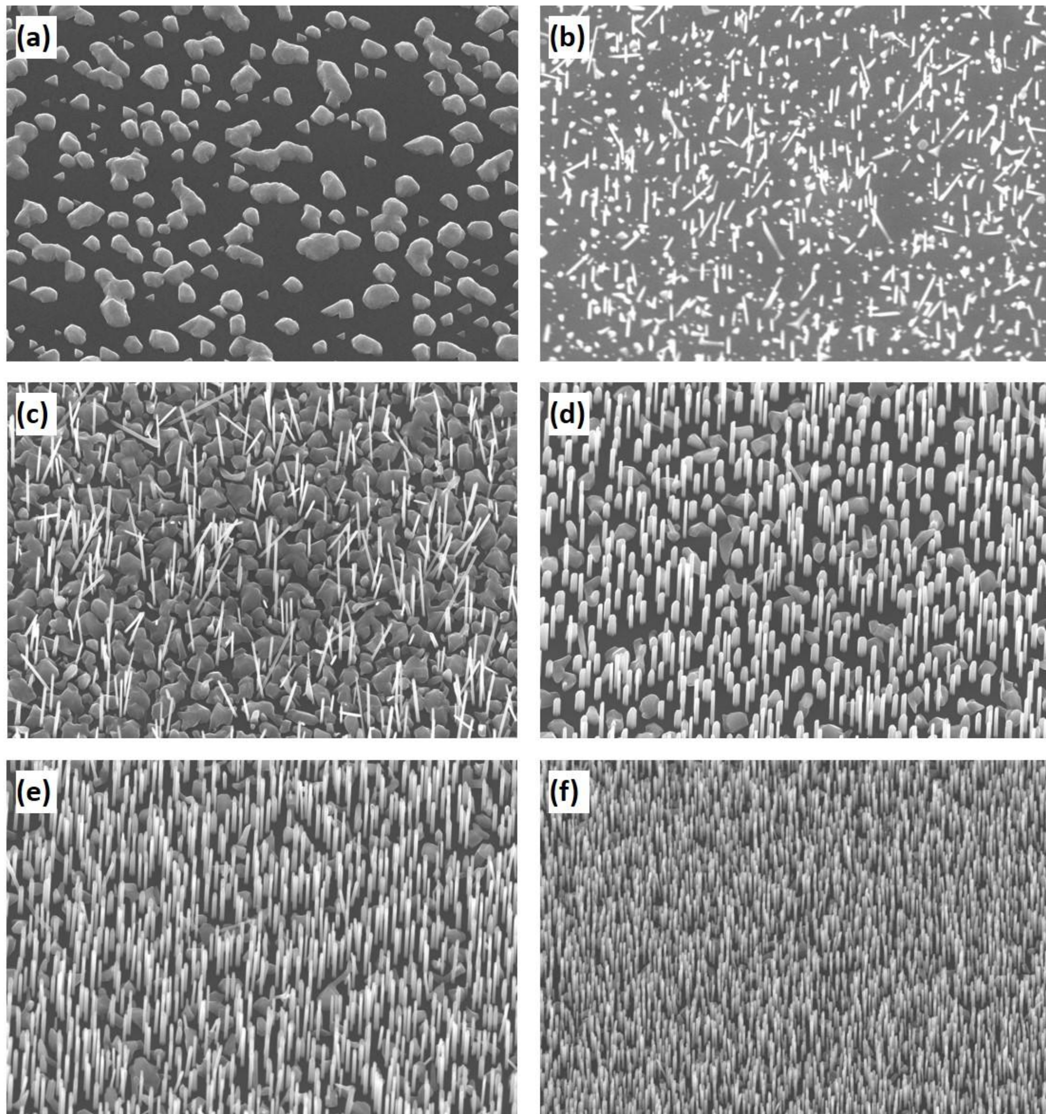

Figure 6.1. The SEM images of several InAs NWs samples.

The initial growths results depicted in Figure 6.1 (a) show that only clusters are present and no nanowires have been formed. This indicates that the temperature of growth was far from suitable. Figures 6.1 (b) and (c) show some progress on the growth. Some nanowires are present in between the cluster formations however their density is still low and they grew at various angles. From 6.1 (d) to (f) it can be observed that following further growth temperature adjustments the nanowires density is increased and their length more uniform. All the nanowires on the later

samples are grown in a vertical direction and clusters density is low.

SEM is a good starting point for the assessment of the quality of the grown nanowires. It provides vital information on their uniformity, length, diameter etc. depending on their position on the wafer. Observing these features allows for deducing the necessary growth conditions adjustments. The next step in assessing the quality of the grown material is photoluminescence (PL) measurement. If the sample is of poor quality, usually no signal can be detected. Improvements in quality can be observed as an increase in strength of the PL signal. Analysis of the wavelengths and relative positions of the peaks in the PL spectra can provide information on the bandgap and defects within the nanowires. Figure 6.2 shows PL spectra of several InAs NW samples clearly indicating the improvement in signal strength as the quality of the NWs is improved.

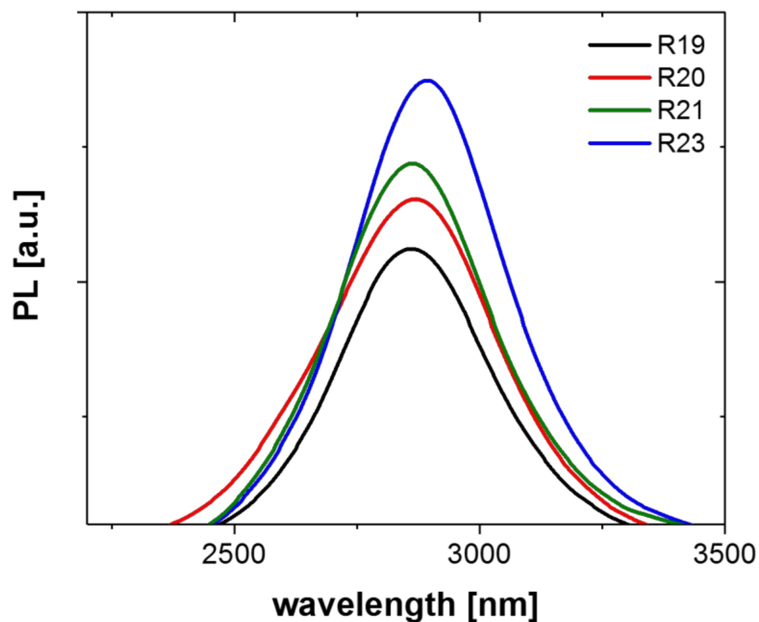

Figure 6.2. The PL spectra of several InAs NWs samples taken at 10K.

Since InAs has high number of surface states and the sample has not been passivated, the carrier recombination is dominated by surface states and the overall photoluminescence reduced. Surface states-dominated emission is a serious disadvantage for any photonic or optoelectronic devices as it severely limits the usability of the generated carriers as they have a high chance of recombining at the surface before they can be extracted. Therefore surface passivation leading to elimination of surface states can be identified as the key to obtaining InAs NWs of quality suitable for high-performance devices. The next section of this chapter proposes a passivation solution for the InAs nanowires and analyses how much impact it has on the performance of the NWs. InP has been chosen for the passivation as having a several times larger bandgap it would create a high barrier for the electrons accumulated near the InAs surface and hence prevent them from reaching the surface of the InAs/InP nanowires. Since the carriers are confined away from the surface, surface states recombination does not occur.

6.2. InAs Nanowires Capped with InP

6.2.1. Growth Conditions and Initial Quality Assessment

The nanowires have been grown by a solid source Veeco Gen 930 MBE system, the one described in section 3.1.1 of this thesis. For indium deposition a solid In source has been used and for arsenic and phosphorus As_4 and P_2 cracker cells, respectively. The InAs NWs have been grown by self-catalysed method directly on p-type Si(111) substrate. Indium flux of 4.78×10^{-8} Torr, V/III ratio of 288, substrate

temperature of 450°C have been used in a one-hour-long growth. Afterwards the InP shell was grown for 10 minutes at In flux of 4.78×10^{-8} Torr, V/III ratio of 60 and substrate temperature of 400°C. The results of growths with and without the InP shell are presented in Figure 6.3.

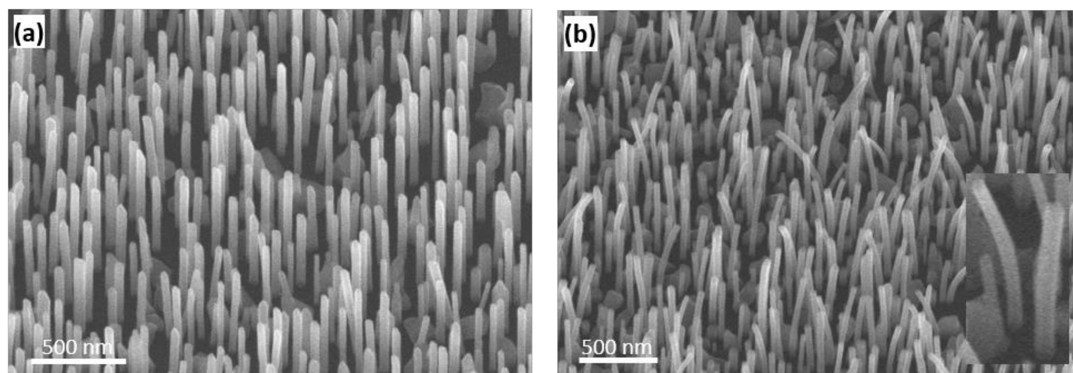

Figure 6.3. The SEM images (tilt angle 25º) of (a) InAs core-only NWs and (b) InAs/InP core/shell NWs grown on Si(111) substrates via a self-catalyzed MBE growth method. The inset in (b) shows a high magnification image of single InAs/InP nanowires.

From the SEM images in Figure 6.3 it can be seen that for both samples the nanowires have been grown vertically on the silicon substrate, however there is an obvious difference between the two samples in shape of the nanowires. While the InAs-only core NWs are perfectly straight, the core/shell InAs/InP ones are visibly bent. This is caused by the strain induced on the InAs core of the nanowire by the InP shell. All the observed nanowires are of good overall quality without any obvious defects. They are also uniform in diameter, density and length. The NWs are about 500 nm long in both samples and have diameters of 55-60 nm with 3-5 nm accounting for the shell in the InAs/InP NWs.

6.2.2. Crystal Quality, Structure and Composition

The best method to evaluate the quality of the grown crystal and its structure is tunnelling electron microscopy (TEM). Figure 6.4 (a) shows a TEM image of one of the InAs/InP nanowires. The diameter of the nanowire is readily confirmed as well as the presence of a thin shell of InP. The interface between the two materials can be easily distinguished as a sharp contrast in the colour of the two sections, confirming two different materials are present. The inset shows a close-up of that interface, from which it can be observed that the thickness of the shell at the measured section is about 3 nm.

High resolution TEM makes it possible to observe single atoms and how they are ordered in the lattice. Figure 6.4 (b) shows such a high-resolution TEM image of a middle section of the measured nanowire. It can be seen that there are two distinctly different ways in which the atoms are ordered in different sections of the image. These account for two different crystal phases, zinc-blende (ZB) and wurtzite (WZ), which are the two crystal phases observed in InAs crystals as well as i.e. other III-V semiconductors. Since both of the phases are present, the structure of the presented InAs nanowires can be described as polytypic. Examples of the two different crystal phases have been highlighted on the image with green (ZB) and blue (WZ). The inset shows a selective area electron diffraction pattern taken for the same nanowire, which again confirms the presence of both WZ and ZB phases. The composition switches between the two phases with fluctuations in substrate temperature and fluxes ratios during the growth. Further work on the growth conditions is required in order to fine

tune these parameters and obtain pure-phase InAs NWs.

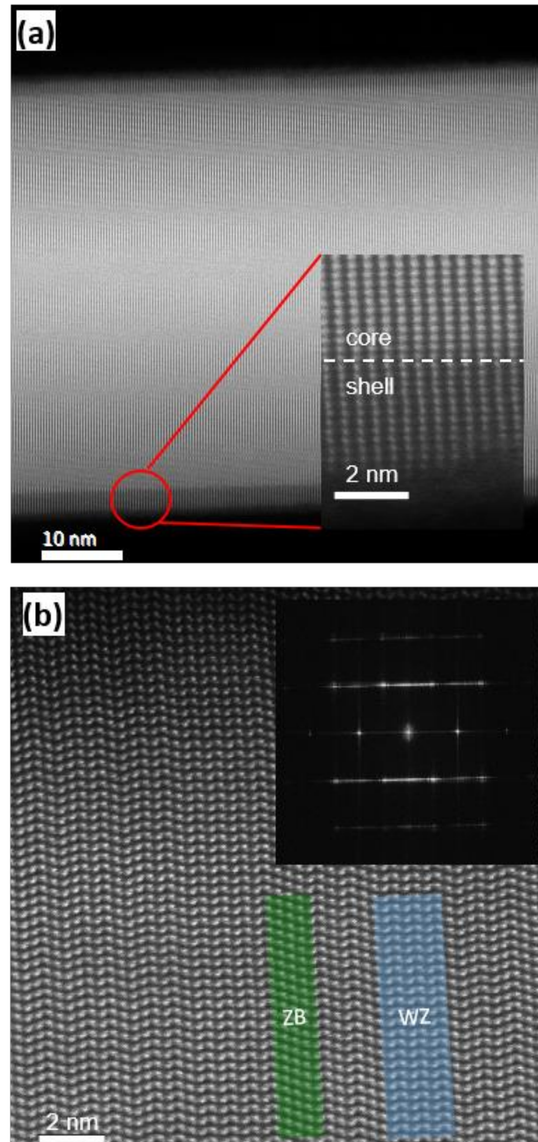

Figure 6.4. (a) <112> ADF-STEM image of a middle section of one of the InAs/InP NWs clearly showing the core and shell parts of the structure. (b) <110> ADF-STEM image of a middle section of one of the InAs/InP NWs showing polytypic structure of the nanowires with highlighted examples of wurtzite (blue) and zinc-blende (green) crystal phases. The inset shows the selective area electron diffraction pattern taken for one of the nanowires confirming that both wurtzite (WZ) and zinc-blende (ZB) phases are present.

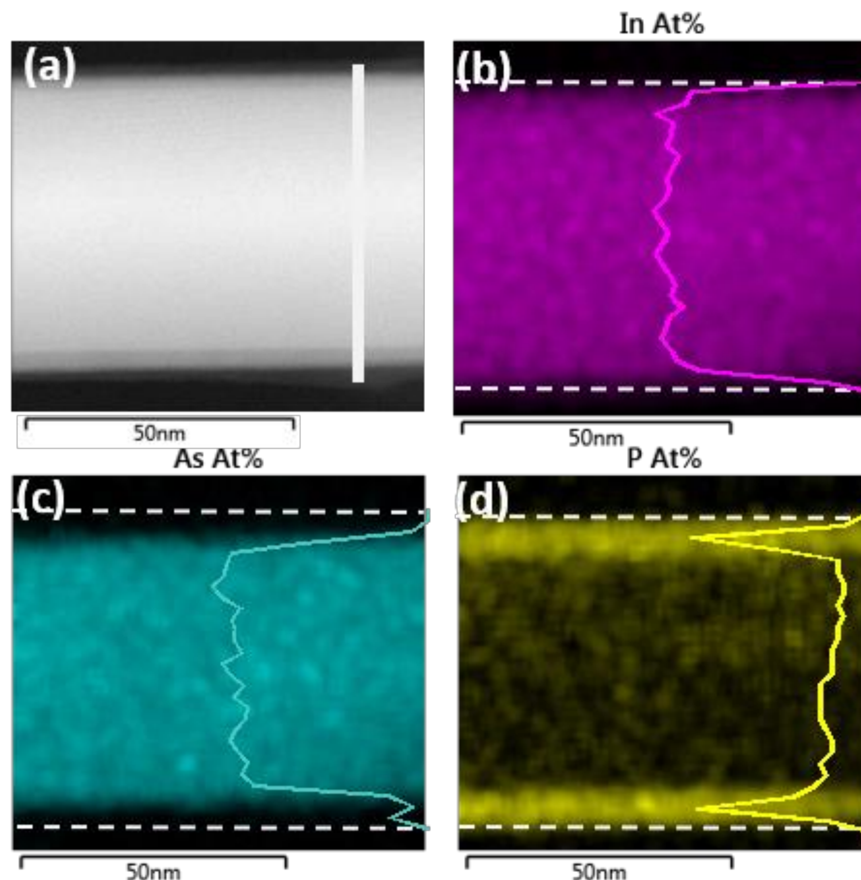

Figure 6.5. Composition analysis of the InAs/InP NWs with EDX. (a) Middle section of a NW with highlighted (b) In, (c) As and (d) P elemental distribution. EDX line profile taken along the white line indicated in (a) correcponding to the In, As and P have also been plotted in (b), (c) and (d), respectively.

In order to analyse the composition of the InAs/InP nanowires energy dispersive x-ray spectroscopy was performed. A fragment of the middle section of a nanowire shown in Figure 6.5 (a) has been measured as well as its cross-section as indicated with the line. The analysis shows uniform distribution of indium throughout the sample (Fig. 6.5(b)) and of arsenic in the core (Fig. 6.5(c)). Figure 6.5(d) shows high phosphorus content within the shell of the nanowire. This analysis confirms that the

core of the NW is composed of InAs and the shell of InP. The interface between the InAs and InP is not abrupt and some intermixing of P and As atoms can be observed in the core region close to the shell. The line plots in Figures 6.5 (b)-(d) indicate concentrations of In, As and P, respectively, along the cross-section indicated in Figure 6.5(a).

6.3. Photoluminescence Study of the InAs and InAs/InP Nanowires

A mid-IR photoluminescence (PL) measurement setup described in section 3.3.1 of this thesis has been used to analyse the photoluminescence of both InAs core-only and InAs/InP core/shell nanowires. When nanowires are grown via the self-catalysed growth on non-patterned substrates, some of the material is deposited on the residual oxide and amorphous clusters are formed. To ensure that the measured signal originated from the nanowires themselves and not those clusters, before the measurements the NWs have been mechanically removed from the sample via ultrasonication and deposited on a clean piece of silicon substrate. The measurements have been taken at a range of temperatures between 10 and 300 K. For power-dependent measurements laser powers between 50 and 600 mW have been used, where the power delivered to the sample is half of the laser output. For temperature-dependent measurements laser power of 600 mW (300 mW at the sample) has been used.

6.3.1. Peaks Analysis

First measurements have been taken at 10K. The red lines in Figure 6.6 (a) and (b) show the original measurements, it can be easily observed that there are multiple peaks present in the spectrum. Using peak fitting the spectrum from InAs NWs can be resolved into three peaks (Fig. 6.6(a)), A1 centred around 2607 nm (475.6 meV), A2 at 2835 nm (437.3 meV) and A3 at 2932 nm (422.9 meV), while the spectrum from InAs/InP NWs contains only two peaks, B1 at 2524 nm (491.2 meV) and B2 at 2833 nm (437.6 meV). All of the peaks observed in Figures 6.6. (a) and (b) are blue-shifted from the bulk InAs emission (around 3000 nm, 415 meV from literature[16]; 3026 nm, 409.7 meV from measurement of InAs wafer, reference peaks in Figure 6.6(a) and (b)). The most probable reasons for this shift are either size-induced quantisation effects or Burstein-Moss (band-filling) effect commonly observed for nanowires[17]. Both of these processes cause bandgap broadening hence the blue-shift. There is also a slight blue-shift of the InAs/InP spectrum peaks compared to the InAs core-only NWs induced by the strain of the InP cladding layer on the InAs core[18,19].

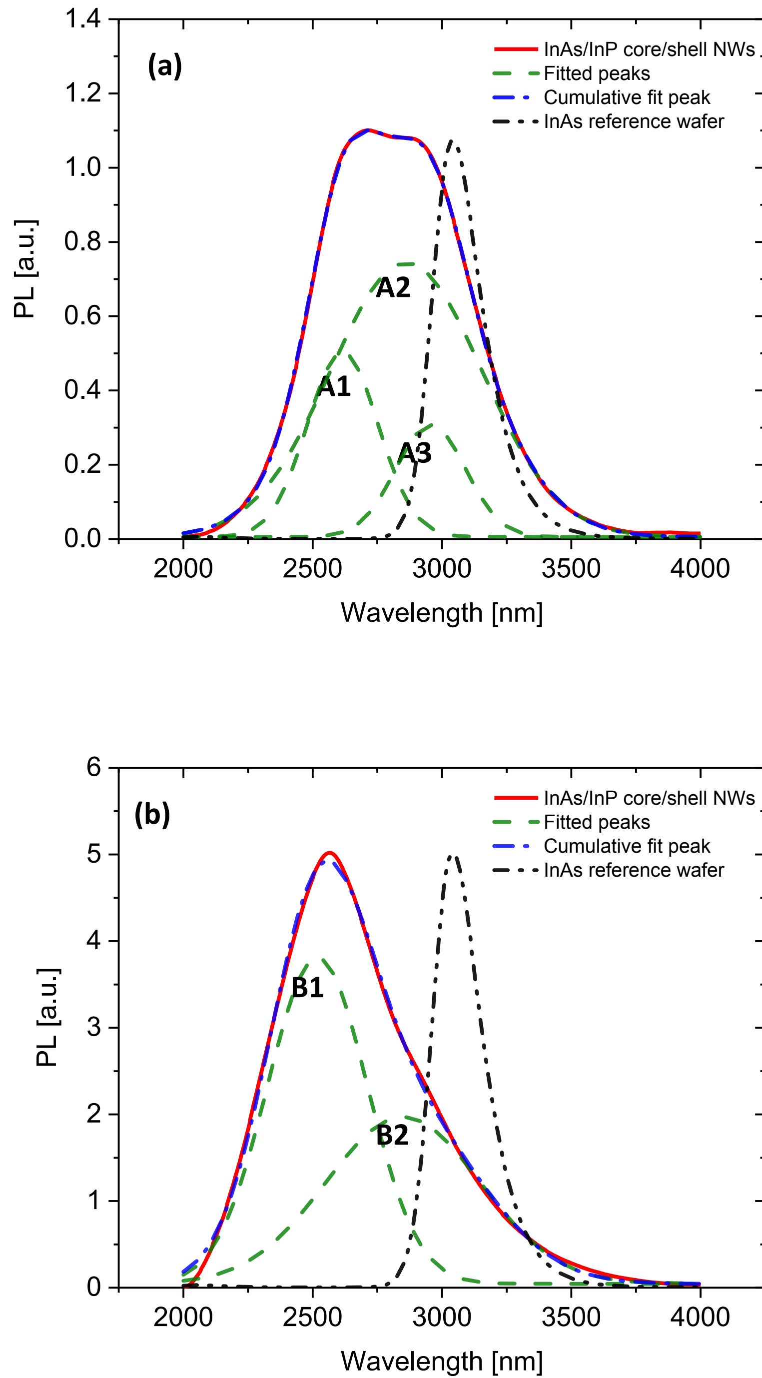

Figure 6.6. PL spectra taken at 10K for (a) the InAs core-only and (b) the InAs/InP core/shell nanowires with InAs wafer emission as reference. Measured signal (red), fitted Gaussian peaks (green), sum of the fitted peaks (blue) and normalized InAs wafer reference (black) have been plotted.

The differences in energies between the different peaks of the same sample help to determine their origin. Usually observed are ground state emission, first excited state emission (at high laser powers), emission from various defect states. Different wavelength peaks can also indicate different materials or their compositions within the measured sample. Zanolli et al. showed in their calculations that these is a difference between the bandgap energies of wurtzite and zinc-blende phases in InAs bulk of about 55 meV at 0 K[20]. The energy difference between peaks B1 and B2 is 53.6 meV and between A1 and A3 is 52.7 meV, both very close to the theoretical prediction. The minor deviations from the bulk value and between the two samples can be accounted for by the same effects as those causing the blue-shifts.

The observations of these energy differences between the peaks of both samples led to a conclusion that the shorter-wavelength peaks A1 and B1 arise from the wurtzite segments of the nanowires, while longer-wavelength peaks A3 and B2 arise from the zinc-blende segments. Surface effects dominate recombination processes in InAs NWs due to their small diameter and high surface electron density. The InP shell passivates the surface of the InAs nanowires suppressing the surface-related emission in favour of emission from the NW core. Therefore the A2 peak dominating the InAs core-only emission can be attributed to surface states related emission while an analogous peak is not present in the passivated InAs/InP sample.

6.3.2. Temperature Dependent Measurements

The temperature-dependent PL measurements have been taken at temperatures between 10 and 300 K at 50 K intervals. The results for the core-only and core/shell have been plotted in Figure 6.7 (a) and (b) respectively. The relative intensities of the peaks in the spectra for the core-only NWs change at sample temperatures of 200 K and above. This is caused by an increase in the surface states emission relative to the nanowires emission as the surface related processes are more significant at higher temperatures. The general shape of the spectra does not change with temperature for the InAs/InP sample and the intensity drops with increasing temperature as expected.

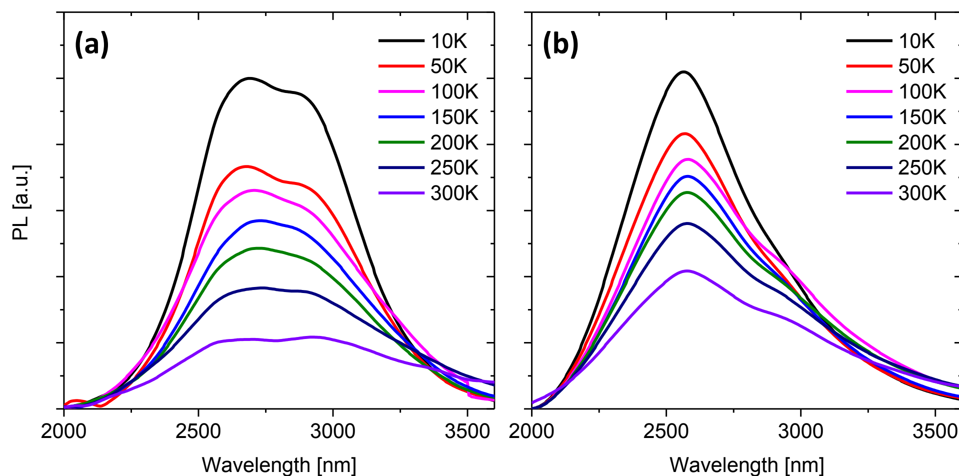

Figure 6.7. PL spectra taken at temperatures between 10 and 300 K for (a) the InAs core-only and (b) the InAs/InP core/shell nanowires.

Strong PL emission can be observed for both samples all the way up to room temperature (300 K). At 300 K, the intensities of InAs and InAs/InP samples were

about 20% and 40% of that at 10 K, respectively. Achieving such strong emission at room temperature confirms high quality of the material and its suitability for fabrication of devices capable of working at room conditions.

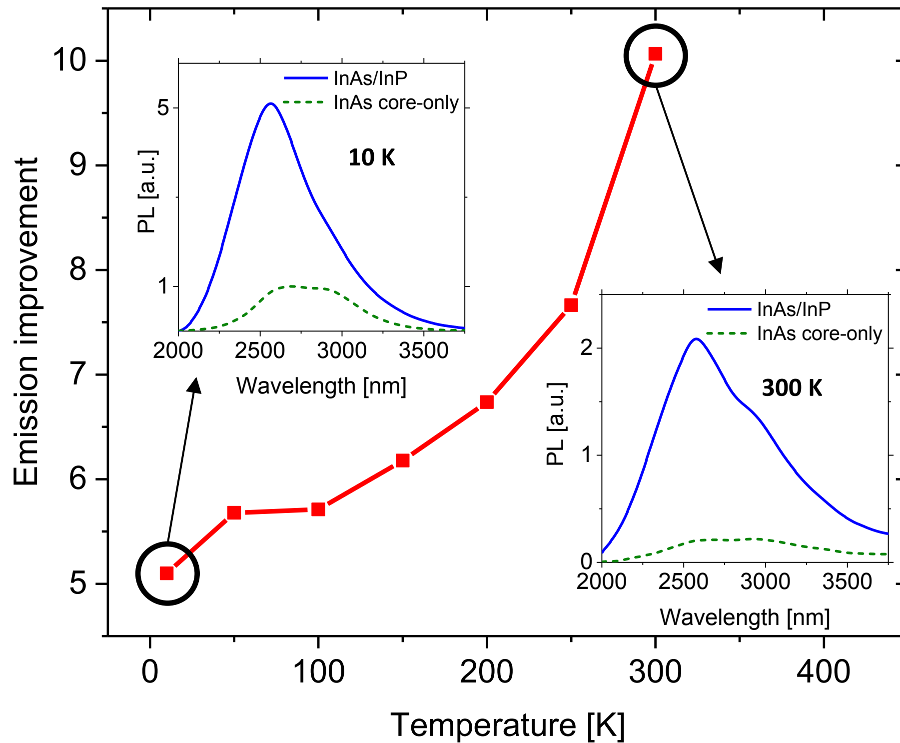

Figure 6.8. Emission improvement of the InAs/InP NWs over InAs NWs, the insets show PL emission for the two samples at 10 and 300 K.

Figure 6.8 shows the emission improvement of the InAs/InP core/shell nanowires compared with the emission of the InAs core-only sample. The improvement was calculated as the ratio of the maximum strengths of the signals from the two samples. The improvement at 10 K is about five-fold, as depicted with left-hand side inset, and increases with temperature to real about ten-fold difference at 300 K, as shown on

the right-hand side inset. The reason for increase in the ratio between the two samples arises from the fact that the core-only NWs emission being dominated by the surface states is highly sensitive to temperature. The unpassivated InAs NWs are more strongly affected by the thermal effects due to the exposed surface states.

The results of the temperature-dependent PL and analysis of the emission strength ratios show that passivation of the InAs NWs with an InP capping layer is highly effective at supressing the surface states related emission and hence considerably improving the optical performance of the material. The achieved ten-fold improvement at room temperature is a large step forward towards fabricating real-life, commercially-relevant InAs NWs based optoelectronic and photonic devices.

6.3.3. Integrated Photoluminescence Analysis

Integrating the PL signal for both samples taken at different excitation powers and temperatures allowed for further analysis of the optical properties of the InAs nanowires. In Figure 6.9 (a) the integrated PL signal has been plotted against the laser excitation power at temperatures of 10, 100, 200 and 300 K. A typical trend can be observed for the InAs/InP NWs sample where the integrated PL values rise quickly with increasing power (up to around 100 mW), and then starts to saturate at higher powers. The general shape of the plots is preserved at all the temperatures, only the intensity drops as expected when the temperature is increased. For the InAs core-only nanowires the trends are similar, however it takes longer to reach the saturation levels as the temperature is increased. This is caused by the surface states and

higher susceptibility of the non-passivated InAs core-only NWs to thermal effects. Once again a significant improvement on the optical properties of the NWs in terms of their PL output is observed for the InP-passivated sample.

Figure 6.9 (b) shows the integrated PL values for the two nanowires samples and a reference InAs wafer as a function of temperature of the sample. The plot for the InAs wafer follows the typical trend where the PL intensity drops rapidly as the temperature of the sample is increased from 10 to 300 K. However, both nanowires sample show a relatively steady trend across the whole temperature range. The integrated PL intensity for the InAs (InAs/InP) sample only drops by a factor of 3 (2) between 10 and 300 K. Such a remarkable thermal stability can be attributed to very high carrier confinement within the nanowires. In bulk materials, thermally excited carriers are free to move around and non-radiatively recombine. However, because of the small dimensions of the nanowires and a small contact area with the substrate the generated carriers cannot easily escape and then recombine. Since the trends for the both samples are very similar they indicate that the confinement effects are more pronounced that the difference caused by the surface states effects.

Comparing the trends for the InAs NWs and the InAs wafer it is interesting to notice that at temperatures above 200 K the integrated PL signal of the nanowire sample is stronger than that of the wafer. This could be explained by the geometry of the wafer (bulk material) and the fact that it has not been passivated.

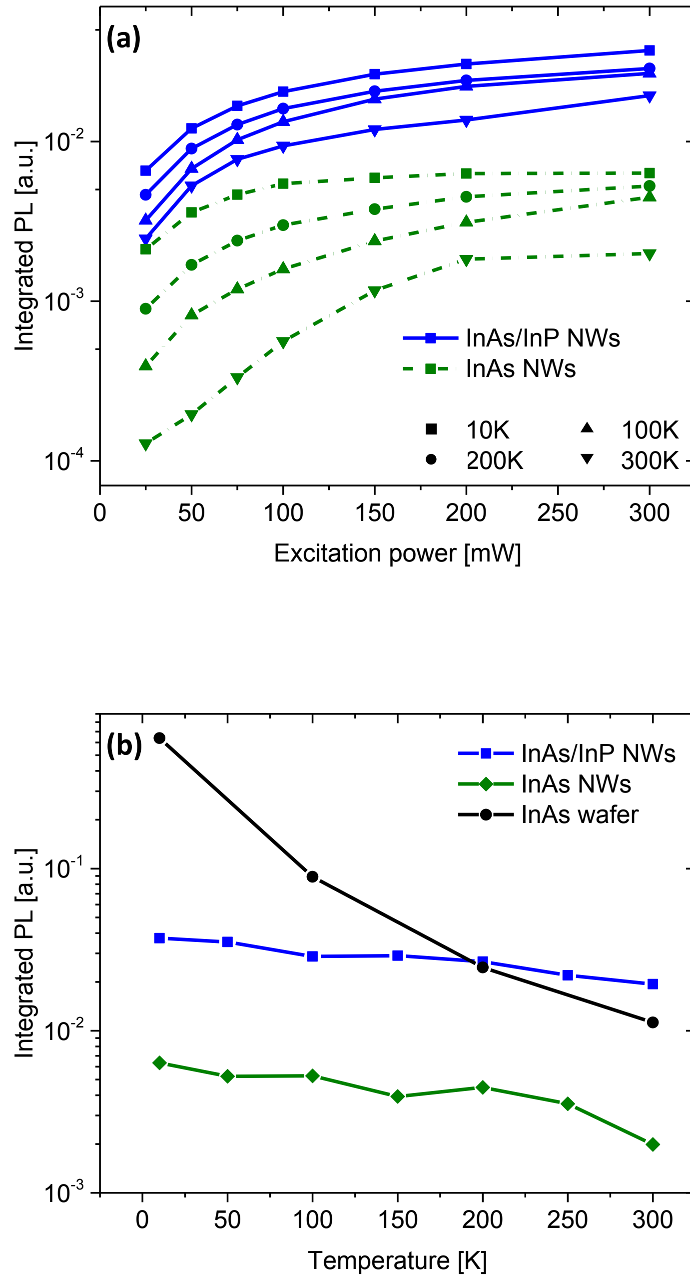

Figure 6.9. Integrated PL as a function of (a) excitation power for a range of temperatures between 10 and 300 K and (b) sample temperature for InAs/InP nanowires (blue), InAs core-only nanowires (green) and InAs wafer (black).

6.4. Conclusions

InAs nanowires have been successfully grown by a self-catalysed method via molecular beam epitaxy (MBE) and high quality of the produced material has been confirmed by SEM and TEM imaging. The optical properties of InAs nanowires have been analysed in detail by photoluminescence (PL) measurements at a range of laser excitation powers and sample temperatures.

The first conclusion of the work presented in this chapter of the thesis is that using a thin layer of InP cladding on top of the InAs core effectively passivates the surface states and minimises the impact of related recombination processes whilst promoting emission from the nanowire core itself. The passivation results in up to ten-fold improvement in strength of the photoluminescence emission from the InAs/InP nanowires compared to the InAs core-only NWs.

Temperature-dependent PL measurements showed that strong emission can be obtained for both the nanowire samples up to room temperature. This confirms good quality of the grown samples and indicates that the InAs NWs would be suitable for fabrication of high-performance optoelectronic and photonic devices working in room conditions.

High carrier confinement has been observed from the integrated PL measurements across a range of temperatures. Both samples showed a good temperature stability, distinctly different to the behaviour of bulk InAs. These features can be an important advantage in design of novel electronic and quantum devices or lead to new observations of nanoscale physical phenomena.

The results presented in this chapter could have a high impact on the further development of InAs NWs optoelectronic materials and devices. The good optical performance is promising for thermophotovoltaic applications, whilst the unique geometry could also be taken advantage of for cooling of the devices, which is essential for efficient thermophotovoltaic energy conversion. However, fabrication of TPV devices out of these nanowires would first require a lot of improvements in fabrication processes for nanowires in general. Therefore, even though from material point of view the InAs nanowires are a highly promising choice for TPVs, we are still far off from creating functional devices.

6.5. References

1. Fasth, C.; Fuhrer, A.; Samuelson, L.; Golovach, V.N.; Loss, D. *Phys. Rev. Lett.* 2007, 98, 266801.
2. Thelander, C.; Bjork, M.T.; Larsson, M.W.; Hansen, A.E.; Wallenberg, L.R.; Samuelson, L. *Solid State Comm.* 2004, 131, 573-579.
3. Sun, M.H.; Leong, E.S.P.; Chin, A.H.; Ning, C.Z.; Cirlin, G.E.; Samsonenko, Y.B.; Dubrovskii, V.G.; Chuang, L.; Chang-Hasnain, C. *Nanotechnology* 2010, 21, 33.
4. Rota, M.B.; Ameruddin, A.S.; Fonseka, H.A.; Gao, Q.; Mura, F.; Polimeni, A.; Miriametro, A.; Tan, H.H.; Jagadish, C.; Capizzi, M. *Nano Lett.* 2016, 16, 5197-5203.
5. Dubrovskii, V.G.; Sibirev, N.V.; Berdnikov, Y.; Gomes, U.P.; Ercolani, D.; Zannier, V.; Sorba, L. *Nanotechnology* 2016, 27, 375602.
6. Dick, K.A.; Thelander, C.; Samuelson, L.; Caroff, P. *Nano Lett.* 2010, 10, 3494-3499.
7. Caroff, P.; Dick, K.A.; Johansson, J.; Messing, M.E.; Deppert, K.; Samuelson, L. *Nature Nanotechnology* 2009, 4, 50-55.
8. Chuang, L.C.; Moewe, M.; Chase, C.; Kobayashi, N.P.; Chang-Hasnain, C.; Crankshaw, S. *Appl. Phys. Lett.* 2007, 90, 4.
9. Roest, A.L.; Verheijen, M.A.; Wunnicke, O.; Serafin, S.; Wondergem, H.; Bakkers, E.P.A.M. *Nanotechnology* 2006, 17, S271.
10. Tchernycheva, M.; Travers, L.; Patriarche, G.; Glas, F.; Harmand, J.C.; Cirlin, G.E.; Dubrovskii, V.G. *J. Appl. Phys.* 2007, 102, 9.

11. Koblmuller, G.; Vizbaras, K.; Hertenberger, S.; Bolte, S.; Rudolph, D.; Becker, J.; Doblinger, M.; Amann, M.C.; Finley, J.J.; Abstreiter, G. Appl. Phys. Lett. 2012, 101, 5

12. Soo, M.T.; Zheng, K; Gao, Q.; Tan, H.H.; Jagadish, C.; Zou, J. *Nano Lett.* 2016, 16(7), 4189-4193

13. Gomes, P.U.; Ercolani, D.; Zannier, V.; David, J.; Gemmi, M.; Beltram, F.; Sorba, L. *Nanotechnology* 2016, 27, 25

14. Zhang, Y.; Wu, J.; Aagesen, M.; Liu, H. *J. Phys. D Appl. Phys.* 2015, 48, 463001.

15. Zhang, Y.; Aagesen, M.; Holm, J.V.; Jorgensen, H.I.; Wu, J.; Liu, H. *Nano Lett.* 2013, 13, 3897-3902

16. InAs band structure and carrier concentration, IOFFE institute, accessed on 3rd February 2017, http://www.ioffe.ru/SVA/NSM/Semicond/InAs/bandstr.html

17. Yan, Y.; Liao, Z.M.; Bie, Y.Q.; Wu, H.C.; Zhou, Y.B. *Appl. Phys. Lett.* 2011, 99, 10

18. Shiri, D.; Kong, Y.; Buin, A.; Anantram, M.P. *Appl. Phys. Lett.* 2008, 93, 7

19. Wei, B.; Zheng, K.; Ji, Y.; Zhang, Y.; Zhang, Z.; Han, X. *Nano Lett.* 2012, 12, 4595-4599

20. Zanolli, Z.; Fuchs, F.; Furthmuller, J.; von Barth, U.; Bechstedt, F. *Phys. Rev. B*

Chapter 7:

Conclusions and Future Work

This chapter summarises the major contributions of this thesis towards development of highly efficient semiconductor thermophotovoltaic (TPV) cells. Several approaches have been studied in this thesis, however all of them require significantly more work before they become feasible solutions for practical applications of TPVs. Therefore this chapter also includes some suggestions on further possible improvements and ways to achieve them.

7.1 Conclusions

In this thesis several pathways towards development of commercially viable thermophotovoltaic cells have been explored. They include modelling of optimal TPV cells, growth and fabrication of the designed devices, optical studies of suitable nanostructures

and finally development of MBE growth methods of alternative TPV-compatible materials.

The study of literature on previous developments in thermophotovoltaic area highlighted two main problems on material level: the chosen semiconductors are not suitable due to indirect bandgaps (germanium, silicon) [1-3] or growth of the suitable low-bandgap materials is technologically challenging (In-rich InGaAs, InAsSb) [4-8]. Another problem is lack of consensus on what bandgaps and hence which materials are most suitable, as no detailed studies have been reported in this area. Therefore the first part of work for this thesis, described in detail in Chapter 4, focused on developing a comprehensive model of TPV cells. The material of choice for this study was InGaAs as its bandgap can be varied over a large range, from 0.36 eV (InAs) to 1.42 eV (GaAs). The developed model can also be easily adapted for other materials.

Using this model optimal bandgaps for different operating conditions (temperature of the source and incident power density) have been calculated. It was demonstrated that the optimal bandgap of a TPV cell is directly linked to the temperature of the source. As the temperature of the emitted increases, so does the optimal bandgap of a TPV cell. This is related to the energy of the peak intensity of the thermal radiation from the source. Hence for emitters at typical temperatures of 1000-1400 K InAs or even a lower bandgap material like InAsSb is most suitable. No correlation between the strength of radiation and the bandgap of the cell has been found. Various parameters of the structures (architecture, thickness, temperature, defects) have been taken into account. It was observed that maintaining low cell temperature during operation is crucial for high efficiency as every 50 degrees increase above 300 K cuts about 5% from the total

efficiency of the cells. Investigation of absorption properties of cell architectures with and without light trapping showed that minimal thicknesses of such cells are 3 μm and 0.5 μm, respectively. This shows that clever engineering of the cell structure can significantly reduce the amount of material needed and hence reduce the production cost. As quality of real life materials is not perfect, impact of defects have been included in the simulations demonstrating that threading dislocation density of 10^5 cm^{-2} should not be exceeded. The maximum theoretical efficiency of around 25% has been calculated for the InAs-based TPV cells.

The modelling study strongly suggested that use of low-bandgap In-rich InGaAs is a more suitable solution than the commonly used $In_{0.53}Ga_{0.47}As$. The next chapter of the thesis describes in detail the whole process of growth, fabrication and characterisation of $In_{0.85}Ga_{0.15}As$ TPV cells. The material quality of the cells was concluded to be good based on AFM and TEM studies. The composition has been estimated using PL and XRD measurements giving In content of 75-85%. After metallisation process the samples have been extensively characterised. Dark J-V study showed that the fabricated devices exhibit diode behaviour, both at room temperature and 78 K. Generation of photocurrent has been observed under a 1000°C blackbody source, however the total current measured consists mostly of the dark current. Hence improvements on the structure design and fabrication processes are needed to produce high performing devices. The quantum efficiency and responsivity measurements showed that the overall performance of the devices is good, yielding about 50% photon-to-electron conversion efficiency.

The initial results from the fabricated InGaAs devices showed high promise for future development of TPV cells based on this material, however significant improvements on every step of the design, growth and fabrication processes would be necessary to achieve viable devices. Therefore the next part of the project focused on a completely different structure design based on InAs nanowires. Due to their many advantages over bulk materials, nanowires are expected to deliver devices of significantly higher performances. They can also be grown on virtually any substrates, which has a potential of significantly reducing production costs and making the devices commercially viable.

The first step in producing nanowires-based devices is growth of good quality NW materials. The main obstacle in development of high-efficiency InAs photovoltaic devices like TPVs are poor optical properties of the InAs nanowires reported so far. Therefore the next chapter of this thesis focuses on growth of high-quality InAs NWs with significantly improved optical performance. We have identified the large number of surface states as the main reason behind the poor performances of the InAs NWs. The proposed solution of passivating the surfaces of the nanowires with a thin layer of InP has been tested. The differences in performance of passivated and unpassivated samples have been investigated in detail with an extensive PL study. The passivation resulted in up to ten-fold improvement of the photoluminescence (PL) emission. The crystal structures of the grown samples have been assessed in detail using TEM measurements confirming high quality of the material.

Overall, this thesis reports improvements in development of new generation of

high performance thermophotovoltaic devices. The comprehensive modeling study of InGaAs TPV cells provides information needed to understand how to effectively optimize the devices. Finally, novel solutions have been demonstrated for obtaining higher quality materials such as Be-mediated buffer growth for InGaAs or passivation of InAs nanowires with InP.

7.2 Future Plans

Despite promising results for InAs nanowires presented in this thesis, their development into functional devices requires significant developments in nanowire devices fabrication in general. Since large area, nanowire array-based devices are currently not possible to fabricate, development of InAs NWs TPVs needs to be postponed until more advanced techniques are available. Therefore future work should focus on exploring other material systems suitable for TPVs.

Based on the results achieved in this thesis and literature studies of mid-infrared suitable materials, the future plans on the development of thermophotovoltaic cells start with establishing successful growth routines for GeSn compounds with different compositions of Sn. Achieving good quality, direct bandgap GeSn material on Si substrates will enable fabrication of high-quailty, low-cost group-IV TPV cells.

A whole range of possibilities comes from nanostructures formed of the aforementioned group IV materials. Multiple quantum well (MQWs), nanowires and quantum dots (QDs) offer certain advantages over bulk materials as due to their nanoscale dimensions they are capable of reducing the degrees of freedom of carriers

giving rise to quantum effects. As the growth studies of these structures are limited or altogether non-existent, especially for Ge and GeSn, the first step would be to develop growth routines for each of these nanostructures.

Finally, another possible path is integration of group-IV and III-V materials in the same structure in order to take advantages of their specific properties. Since Ge and GaAs are lattice matched, they are especially suitable for this purpose, as their growth would not introduce a significant number of defects. Since the UCL MBE group operates a connected system of group-IV and III-V MBE chambers equipped with a large number of sources (Ge, Si, Sn, Ga, As, In, Sb, P), the scope of possible combinations is wide. Taking advantage of the unique opportunities provided by this setup could be the key to obtaining high-performance, commercially viable TPV devices.

7.3 References

1. T.J. Coutts, A review of progress in thermophotovoltaic generation of electricity, *Renewable and Sustainable Energy Reviews* 3, 1999.
2. R.W. Beck and E.N. Sayers, Study of germanium devices for use in a thermophotovoltaic converter, *Progress Report No 2 (final report)*, DA28-043-AMC-02543(E), General Motors Corporation, 1967.
3. R.J. Schwartz, The theoretical and experimental investigation of planar pin thermophotovoltaic cells, *Contract No.* DAAB07-70-C-0129, Purdue University, 1971.
4. S. Murray, F. Newman, C. Murray, D. Wilt, M. Wanlass, P. Ahrenkiel, R. Messham, and R. Siergiej, "MOCVD growth of lattice-matched and mismatched InGaAs materials for thermophotovoltaic energy conversion," *Semiconductor Science and Technology 18*, 2003.
5. M.K. Hudait, Y. Lin, M.N. Palmisiano, and S.A. Ringel, "0.6-eV bandgap In/sub 0.69/Ga/sub 0.31/As thermophotovoltaic devices grown on InAs/sub y/P/sub 1-y/ step-graded buffers by molecular beam epitaxy," *IEEE Electron. Device Lett. 24*, 2003.
6. B. Wernsman, T. Bird, M. Sheldon, S. Link, and R. Wehrer, "Molecular beam epitaxy grown 0.6 eV n/p/n InPAs/InGaAs/InAlAs double heterostructure thermophotovoltaic devices using carbon as the p-type dopant," *Journal of Vacuum Science & Technology B: Microelectronics and Nanometer Structures 24*, 2006.

7. J. Cederberg, J. Blaich, G. Girard, S. Lee, D. Nelson, and C. Murray, "The development of (InGa)As thermophotovoltaic cells on InP using strain-relaxed In(PAs) buffers," *Journal of Crystal Growth 310*, 2008.
8. M.K. Hudait, M. Brenner, and S.A. Ringel, "Metamorphic In 0.7 Al 0.3 As/In 0.69 Ga 0.31 As thermophotovoltaic devices grown on graded InAsyP 1− y buffers by molecular beam epitaxy," *Solid State Electron. 53(1)*, 2009.
9. P. Jurczak, A. Onno. K. Sablon, and H. Liu, Efficiency of GaInAs thermophotovoltaic cells: the effects of incident radiation, light trapping and recombinations, *Optics Express 23(19)*, 2015.
10. M. Gutiérrez, D. Araujo, P. Jurczak, J. Wu and H. Liu, Solid solution strengthening in GaSb/GaAs: A mode to reduce the TD density through Be-doping, *Applied Physics Letters 110*, 092103, 2017.
11. P. Jurczak, K. Sablon, M. Gutiérrez, H. Liu and J. Wu, 2.5-μm InGaAs photodiodes grown on GaAs substrates by interfacial misfit array technique, *Infrared Physics & Technology*, Volume 81, Pages 320-324, 2017.